RCA REVIEW

a technical journal

RADIO AND ELECTRONICS
RESEARCH • ENGINEERING

Published quarterly by

RCA LABORATORIES

in cooperation with all subsidiaries and divisions of

RADIO CORPORATION OF AMERICA

VOLUME XXI | MARCH 1960 | NUMBER 1

CONTENTS

RCA REVIEW is regularly abstracted and indexed by *Industrial Arts Index Science Abstracts* (I.E.E.-Brit.), *Electronic Engineering Master Index, Chemical Abstracts, Proc. I.R.E.,* and *Electronic & Radio Engineer.*

RCA REVIEW

BOARD OF EDITORS

SIMULTANEOUS SIGNAL SEPARATION IN THE TRICOLOR VIDICON*

By

HAROLD BORKAN

RCA Laboratories,
Princeton, N.J.

Summary—The operation of the tricolor Vidicon, a single camera tube for color television, presents a novel circuit problem. The target structure contains considerable capacitance which couples the three output electrodes. Extraction of separate color signals in the presence of this cross-coupling impedance must be performed while maintaining a satisfactory signal-to-noise ratio. This paper presents a general analysis of the problem and suggests several practical solutions. The system described involves low input impedance, feedback preamplifiers, and mixed-highs circuitry.

INTRODUCTION

A NOVEL circuit problem is encountered in the design of camera equipment associated with the tricolor Vidicon,[1] a developmental camera tube for color television. The tricolor tube has three output electrodes for delivering three electrical signals corresponding to the red, green and blue information contained in the scene. However, the three output signals are coupled together by the large inherent capacitance of the target structure. The problem is to extract separate color signals in the presence of the cross-coupling impedance while maintaining a satisfactory signal-to-noise ratio.

The target of the tricolor Vidicon, shown in Figure 1, contains color filters in a repetitive sequence of red, green and blue strips. Superposed in registry with each filter is a narrower transparent conducting signal strip. All signal strips behind filters of the same primary color are connected to a common output terminal. Experimental tricolor Vidicons have been made with tube diameters of two inches and one inch. In the two-inch size, the capacitance between one set of signal strips and the other two (the inter-set capacitance) is of the order of 1200 micromicrofarads; in the one-inch size, it is of the order of 600 micromicrofarads. A single electron beam scanning the photoconductor on the target induces video signal currents in each set of strips in proportion to the primary color component.

* Manuscript received December 20, 1959.

[1] P. K. Weimer, S. Gray, C. W. Beadle, H. Borkan, S. A. Ochs, and H. C. Thompson, "A Developmental Tricolor Vidicon Having a Multiple-Electrode Target," to be published in *Trans. I.R.E.*, July, 1960.

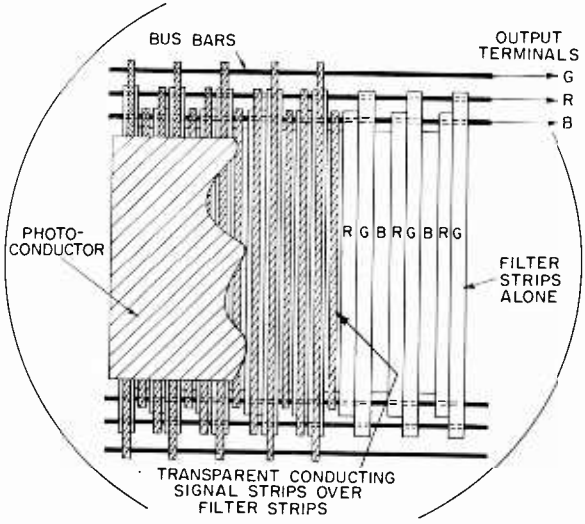

Fig. 1—Cut-away diagram of the tricolor Vidicon target as viewed from the electron gun.

Introductory Calculations

A separate preamplifier is connected to each of the three output leads of the target. The video signal current produces voltage fluctuations in the input load resistor of each preamplifier. Ideally, each separate color signal should be amplified only by its corresponding preamplifier. Actually, because of the inter-set capacitance, it is possible for the signals of higher frequency to cross-couple. An equivalent circuit of the target is shown in Figure 2 as a delta whose sides

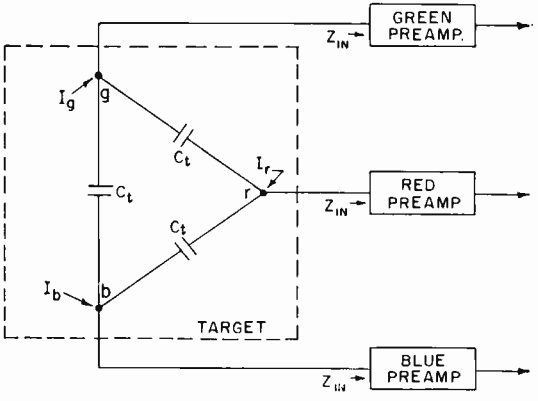

Fig. 2—Equivalent circuit of the tricolor Vidicon target.

are the cross-coupling capacitances, C_t, and whose vertices are the signal strips connected to three preamplifiers with input impedances represented by Z_{in}. Complete symmetry is assumed throughout. Since the beam acts as a high-impedance source, a primary color signal is represented as a single current source driving the corresponding set of strips. In general, the signals from the three sets of signal strips are present concurrently.

Some simple calculations will serve to indicate the signal-separation problem. In Figure 2, C_t, which is one leg of the delta, has a capacitance of 600 micromicrofarads in the larger targets, and a reactance of 204 ohms at 1.3 megacycles, the upper limit of desired signal separation defined by the color-television system. Suppose conventional black-and-white preamplifiers with Z_{in} consisting of a resistor of 50,000 ohms, shunted by 30 micromicrofarads, are used. Also, imagine a scene of a green picket fence on a dark background with optical image size such that the pickets correspond to one-megacycle information. For this case, there is but one signal current, I_g, which divides and flows through the three preamplifiers according to the impedances presented: 34.4 per cent into the green and 32.8 per cent into each of the red and blue. The green picket fence would appear white on a color monitor because it would be made up of almost equal parts of green, red, and blue video signals.

The three alternative paths for I_g have impedances Z_{in} through the green preamplifier, $Z_{in} - jX_c$ through the red, and $Z_{in} - jX_c$ through the blue. If Z_{in} were much smaller than X_c, there would be one low-impedance path through the green preamplifier and two relatively high-impedance paths through the other two preamplifiers; most of the signal current would flow through the desired channel. Suppose preamplifiers of low input impedance are provided by placing a 75-ohm resistor to ground at the head of each preamplifier. The signal separation would be excellent at the lower frequencies, but would deteriorate at the higher frequencies. This method of reducing preamplifier input impedance reduces cross-talk, but, as shown below, the signal-to-noise ratio is quite poor.

The equivalent r-m-s noise current, in amperes, flowing into a camera preamplifier due to the input circuit and first amplifier stage may be expressed as[2]

$$I_n = \sqrt{4kTf_0}\sqrt{\frac{1}{R} + \frac{R_{eq}}{R^2} + \frac{R_{eq}}{3X_c^2}} \qquad (1)$$

[2] H. B. DeVore and H. Iams, "Some Factors Affecting the Choice of Lenses for Television Cameras," *Proc. I.R.E.*, Vol. 28, p. 369, August, 1940.

where k = Boltzmann's constant (1.38×10^{-23} Joules/° K),

T = absolute temperature, taken as 300° K,

f_0 = upper limit of frequency band,

X_c = capacitive reactance to ground at f_0,

R = resistance to ground,

R_{eq} = equivalent noise resistance of the preamplifier input tube.

For a 1.3-megacycle chroma bandwidth, $X_c = 1/(4\pi f_0 C_t) = 102$ ohms (assuming Z_{in} small compared to the target reactance, and direct capacitance to ground small compared with $2C_t$ which is 1200 micromicrofarads in the larger targets). The resistance to ground, R, is 75 ohms and R_{eq} is 45 ohms (for two type 417-A triodes in parallel). Since the target presents a very large capacitance, a reduction in noise is obtained through the paralleling of input tubes.

Substituting in the above expression,

$$I_n = 1.47 \times 10^{-7} \sqrt{0.0133 + 0.0080 + 0.0014},$$

or $$I_n = 0.0221 \text{ microampere.}$$

Since a typical total signal is 0.6 microampere peak-to-peak, or 0.2 microampere in each channel, the signal-to-noise ratio for each color is approximately 9. This poor performance is due largely to the first two terms under the radical which reflect the small value of R. Noise of any one amplifier has been assumed not to cross-talk to the other two amplifiers.

Mathematical Analysis

The problem of signal separation may be analyzed from the equivalent circuit shown in Figure 3. The analysis is simplified by making the assumption of complete symmetry. The cross-coupling capacitances, C_t, between the sets of signal strips are equal and have impedances Z_t. Likewise, the impedances, Z, at the input of the three identical preamplifiers are equal, each comprising a resistor R and capacitance C in parallel. The fictitious noise-voltage generators, e_{ng}, e_{nr} and e_{nb}, represent the noise developed in each head amplifier stage, but exclude the thermal agitation noise due to R. Certainly for best design, R should be chosen very large so that its noise will be dominated by amplifier

noise. The unity-gain preamplifiers have voltage outputs, V, which include signals plus noise.

Each amplifier noise source is effectively in series with the input control grid. The Superposition Theorem is employed to sum up the effects of the three current generators in the form of voltages at r, g, and b, the vertices of the delta. For example, the total input voltage to the green preamplifier is the sum of the separate voltages produced

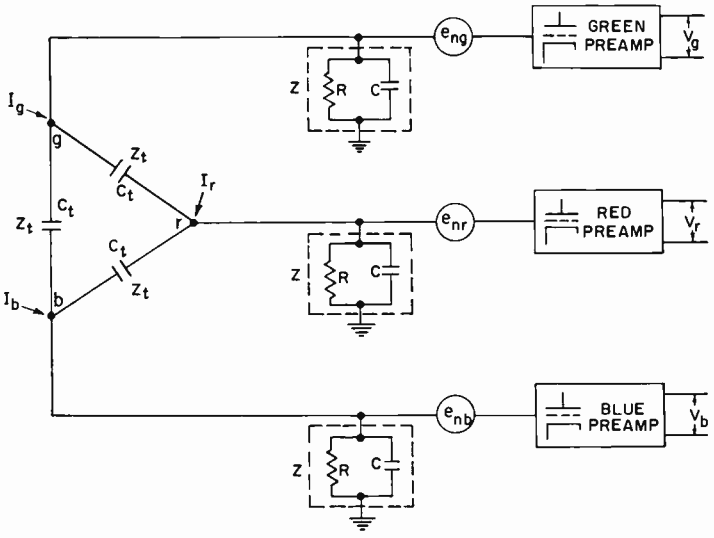

Fig. 3—Equivalent circuit for analysis.

by I_g, I_r, and I_b at g, plus the noise voltage e_{ng}. Therefore, an expression for V_g in terms of the I's and e_{ng} is

$$V_g = I_g \frac{Z(Z+Z_t)}{3Z+Z_t} + I_r \frac{Z^2}{3Z+Z_t} + I_b \frac{Z^2}{3Z+Z_t} + e_{ng}. \tag{2a}$$

The other two expressions are derived in similar fashion;

$$V_r = I_g \frac{Z^2}{3Z+Z_t} + I_r \frac{Z(Z+Z_t)}{3Z+Z_t} + I_b \frac{Z^2}{3Z+Z_t} + e_{nr}, \tag{2b}$$

and

$$V_b = I_g \frac{Z^2}{3Z+Z_t} + I_r \frac{Z^2}{3Z+Z_t} + I_b \frac{Z(Z+Z_t)}{3Z+Z_t} + e_{nb}. \tag{2c}$$

The solutions for the three unknown signals, I_g, I_r, and I_b, plus noise, in terms of the V's are given below:

$$I_g + \left(\frac{2}{Z_t} + \frac{1}{Z}\right)e_{ng} - \frac{1}{Z_t}e_{nr} - \frac{1}{Z_t}e_{nb} = \left(\frac{2}{Z_t} + \frac{1}{Z}\right)V_g - \frac{1}{Z_t}V_r - \frac{1}{Z_t}V_b, \quad (3a)$$

$$I_r - \frac{1}{Z_t}e_{ng} + \left(\frac{2}{Z_t} + \frac{1}{Z}\right)e_{nr} - \frac{1}{Z_t}e_{nb} = -\frac{1}{Z_t}V_g + \left(\frac{2}{Z_t} + \frac{1}{Z}\right)V_r - \frac{1}{Z_t}V_b. \quad (3b)$$

$$I_b - \frac{1}{Z_t}e_{ng} - \frac{1}{Z_t}e_{nr} + \left(\frac{2}{Z_t} + \frac{1}{Z}\right)e_{nb} = -\frac{1}{Z_t}V_g - \frac{1}{Z_t}V_r + \left(\frac{2}{Z_t} + \frac{1}{Z}\right)V_b. \quad (3c)$$

Since all noise sources other than the first-stage shot noise have been excluded in this analysis, the above solutions are optimum. In addition, they are perfectly general, for once pure signals have been secured, regardless of the method chosen for separating signals, the indicated noise will also be present.

Possible Electronic Solutions

The mathematical solutions to the simultaneous equations indicate a direct method for solving the signal-separation problem. With the noise terms omitted, Equations (3) may be expressed as follows:

$$Z_t I_g = \left(2 + \frac{C}{C_t}\right)V_g - V_r - V_b, \quad (4a)$$

$$Z_t I_r = -V_g + \left(2 + \frac{C}{C_t}\right)V_r - V_b, \quad (4b)$$

$$Z_t I_b = -V_g - V_r + \left(2 + \frac{C}{C_t}\right)V_b. \quad (4c)$$

It has been assumed that $R \gg 1/\omega C$ and, therefore, $1/Z \quad j\omega C$.

Figure 4 is a block diagram showing how the above operations may be performed electronically. One channel is represented and only a green signal has been derived. Since the input impedance is capacitive, the subsequent stages of amplification contain correcting networks to insure that the signal is amplified uniformly irrespective of frequency.

An "electronic matrix" could be built to operate on the three observables, the V's, and yield the three desirables, the I's. Some disadvantages of the electronic matrix are: (1) it is critical in adjustment, since each pure color signal is obtained from the difference of two nearly identical signals; (2) the system is somewhat complex; (3) the compensation for the capacitive input impedance over the required number of frequency decades is rather awkward.

A simpler method for the solution of the signal-separation problem involves low-input-impedance preamplifiers. The previous analysis is applicable if R, the actual impedance to ground at the amplifier input,

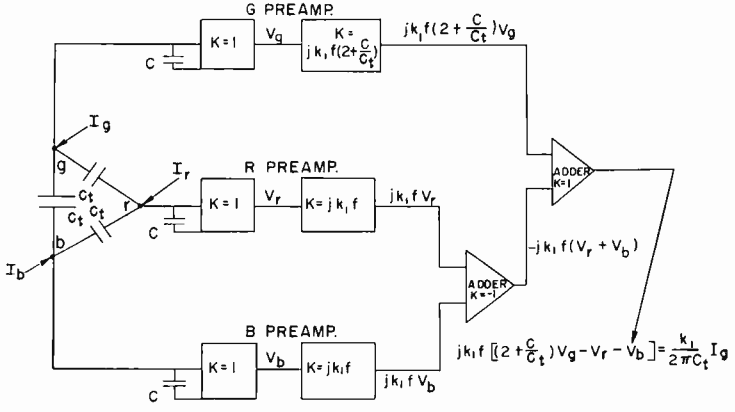

Fig. 4—One channel of the "electronic matrix."

is maintained large. If the low impedance is obtained dynamically, signal separation may be achieved while the optimum signal-to-noise ratios are approached. A dynamic impedance does not exhibit thermal-agitation noise as does a physical resistance. Two methods of dynamically obtaining a low input impedance are: (1) use of negative feedback from the output of each amplifier to its own input, and (2) use of grounded-grid amplifiers. These low-input-impedance preamplifiers do accomplish signal separation within the target. The cross-feeding of signals is accomplished by the delta of Z_t's itself. This method, though not identical with the mathematical solutions given previously, approaches these solutions as the input impedance is made to approach zero.

Expressions for the input impedance, Z_{in}, and the output voltage, V_{out}, of a single-stage feedback amplifier shown in Figure 5, are readily derived:

$$Z_{\text{in}} = \left(\frac{Z_f}{Z_{bp}} + 1 \right) \frac{1}{g_m}, \tag{5a}$$

and

$$V_{\text{out}} = -I_{\text{in}} Z_f, \tag{5b}$$

where $Z_{bp} = \dfrac{r_p Z_b}{r_p + Z_b}$,

Z_b is the plate load impedance,

r_p and g_m are the plate resistance and transconductance of the amplifier tube, respectively,

Z_f is the impedance in the feedback path, and

I_{in} is the signal current.

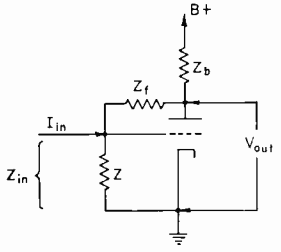

Fig. 5—Schematic diagram of the feedback preamplifier stage.

The above expressions are valid if $g_m \gg \dfrac{1}{Z_{bp}} + \dfrac{1}{Z}\left(\dfrac{Z_f}{Z_{bp}} + 1 \right)$,

where Z is the physical impedance to ground at the preamplifier input.

If two parallel-connected type 417-A triodes are used, g_m is 0.060 mho and r_p is 750 ohms. A practical value for the plate-load resistor is 3000 ohms. If it is desired to have $Z_{\text{in}} = 75$ ohms, then Z_f must be 2200 ohms. For a signal current of 0.2 microampere peak-to-peak in each color channel, V_{out} is 440 microvolts. Assuming a large R (say 200,000 ohms) and all the above values, the imposed conditions are sufficiently satisfied.

Expressions for the input impedance and output voltage for a grounded-grid amplifier may be found in the literature and are given

below:

$$Z_{in} = \frac{Z_b + r_p}{\mu + 1}, \quad \text{and} \quad V_{out} = I_{in} Z_b, \tag{6}$$

where the amplification factor, $\mu = g_m r_p$, and all other terms are the same as previously defined. The above expressions are valid if the resistor in the cathode circuit is much greater than Z_{in}. Assuming the same plate-load resistor, the input impedance for the grounded-grid arrangement is about 81 ohms.

Neither the feedback nor the grounded-grid method requires unusual circuits subsequent to the preamplifiers and neither should be critical in operation. The feedback amplifier is more flexible because a wide range of input impedances may be obtained by inserting the proper feedback impedance. In the cathode-driven arrangement, the input characteristic is primarily determined by the input tube, which has been selected for noise considerations. It appears that a practical method of achieving signal separation is to use special low-input-impedance preamplifiers of the feedback variety.

Feedback Preamplifier Design

The first stage in each of the feedback preamplifiers was chosen on the basis of signal-separation and noise considerations to consist of two parallel-connected type 417-A triodes with a feedback path of 2200 ohms between the plates and grids. A cascode-connected 417-A is used as the second stage because of signal-to-noise considerations. With this arrangement, the second-stage noise has not been made negligible, but has been reduced to a reasonable value. The considerable gain obtainable from the cascode amplifier insures that the signal level at the input to the third stage will be high enough that further degradation is insignificant. The subsequent stages in the preamplifier are conventional.

The Mixed-Highs System

The present standards for color television require only 1.3 megacycles of chroma information. Since all signals, separated as well as cross coupled, pass through the preamplifiers, a total signal above this frequency may be obtained by adding the three preamplifier outputs through a high-pass filter. It is apparent that a signal obtained by summing Equations 3a, 3b, and 3c results in a cancellation of the larger noise terms, since noise originating in one channel appears reversed in phase in the other channels. This feature may be referred to as "correlated noise."

A method of utilizing the correlated noise to improve the signal-to-noise ratio of the tricolor Vidicon is shown in block diagram form in Figure 6. The signals are fed directly into three feedback preamplifiers, each presenting a low input impedance, where they are amplified to about 0.5 volt peak-to-peak. The signals then pass into a level setter which establishes a reference voltage related to black-level during horizontal retrace time. The signals then split up into two paths. One path is through the mixed-highs adder which combines the three signals and passes them through a high-pass filter. This is the mixed-highs channel which carries information made up of equal parts of the original red, green, and blue signals above 1.3 megacycles. The other path for each signal is through a low-pass 1.3-megacycle filter.

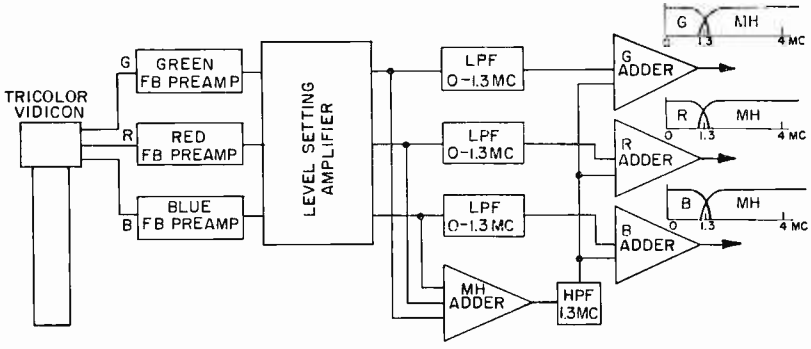

Fig. 6—Mixed-highs system for providing noise reduction in tricolor Vidicon signals.

Since the preamplifiers have separated the color information out to beyond this frequency, each of these three signals contain information of essentially one primary color. The mixed highs are added to each of the color signals in the final adders. The resultant signals may be fed to a simultaneous monitor or used to produce the standard color signal.

Evaluation of the Feedback Method

The feedback preamplifier method of signal separation is evaluated by an analysis of two factors—signal separation ability and signal-to-noise ratio. Figure 7 is a phasor diagram illustrating the magnitude and phase of the three output signals produced by a pure primary color as a function of signal frequency. All sources of cross-talk other than capacitive coupling through the target have been neglected. The diagram is applicable to both two-inch and one-inch targets having the

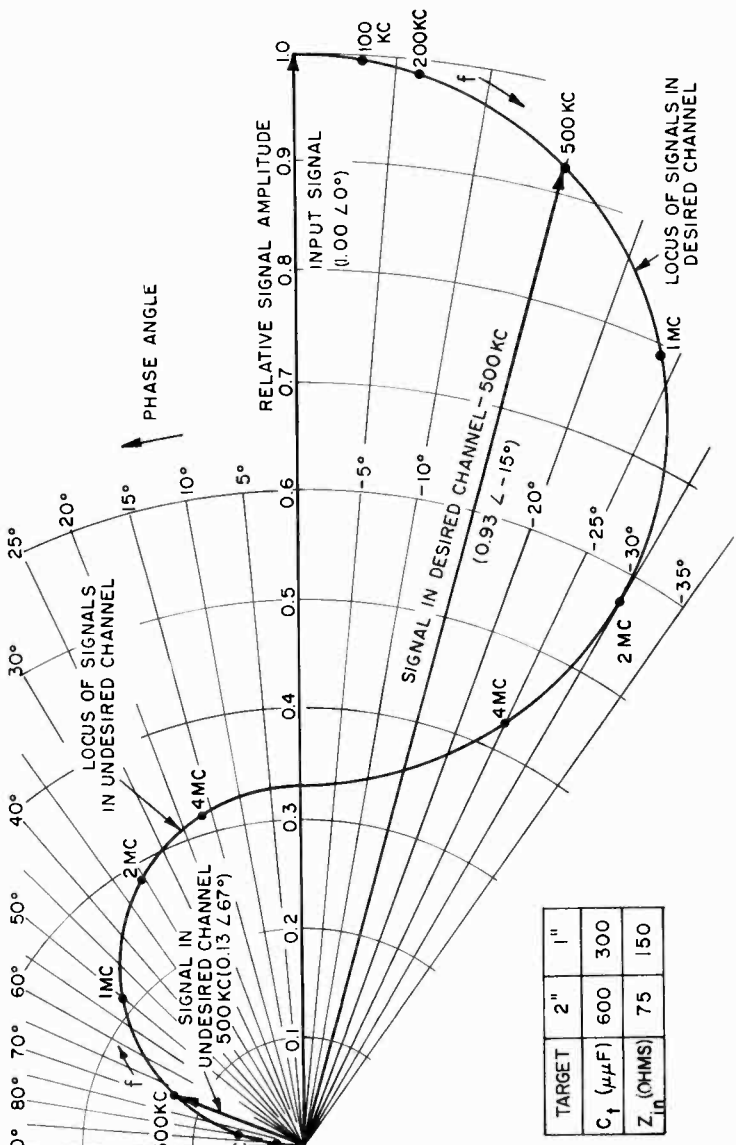

Fig. 7—Phasor diagram showing signals in desired and undesired channels for primary color signals of various frequencies (500-kilocycle signal illustrated).

values of C_t and Z_{in} indicated. While the graph shows color mixing at the higher frequencies, subjectively it has been found that the residual color cross talk is acceptable, since the eye is not sensitive to chromatic differences in small areas. However, should a lower value of input impedance be desirable, it is attainable with slight additional noise degradation in the mixed highs due to the second amplifier stage.

In the appendix, optimum values for signal-to-noise ratios have been calculated to be 29 for each color channel and 330 for the mixed highs. These values are for a 0.6-microampere peak-to-peak white signal. The calculated value for each color channel is determined only by first-stage amplifier noise.

Since thermal agitation noise, beam noise, and second-stage noise are found to be negligible when compared with first-stage amplifier noise, the feedback preamplifier signal-to-noise ratio for color information is reasonably close to the optimum value. In practice the system appears better than the calculated value, because of noise cancellation at the picture tube. To a limited extent, noise addition is performed by the observer viewing the picture tube, and some noise cancellation is effected. Thermal agitation and beam noise may also be neglected for the mixed-highs channel, but second-stage noise is appreciable. Its effect is to further reduce the attainable signal-to-noise ratio from the optimum value.

The optimum signal-to-noise ratios assume realistic amplifying tubes and load resistors. If lower-noise amplifier tubes become available, performance will naturally improve. However, one can parallel more tubes at the input and improve the signal-to-noise ratio in color while not appreciably damaging the signal-to-noise ratio in the mixed highs. The prime obstacle to both perfect signal separation and high signal-to-noise is the inherent inter-set capacitance. The color channel signal-to-noise ratio varies inversely as this capacitance and the chromatic cross-talk varies approximately as the capacitance.

The Tricolor Vidicon in the Color Television System

The simultaneous signals from the tricolor Vidicon processed by the mixed-highs circuits may be used to form the standard signal in the usual manner. The standard signal could likewise be produced without the mixed-highs circuits but would benefit less from the correlated nature of the noise. While the specific signal-to-noise ratios have been computed for the output signals of the system shown in Figure 6, the same technique may be used in calculating signal-to-noise ratios for the E_Y, E_I, and E_Q signals.

The analysis has shown that minimum noise occurs when the

simultaneous signals are combined equally. A tricolor Vidicon made with relative sensitivities in each color channel corresponding to the luminance coefficients, would offer reduced noise compared with a tube made with equal sensitivities. The additional noise arising from the inter-set capacitance could then be confined to the chrominance channels and excluded from the luminance. This feature would contribute to reduced noise visibility on both color and black-and-white receivers.

ACKNOWLEDGMENT

The author is indebted to P. K. Weimer under whose direction this work was performed. The contribution to the analysis of the noise problem by D. O. North is greatly appreciated. In addition, thanks are due to H. L. Oehme for constructing the equipment.

APPENDIX

The optimum values for signal-to-noise ratios in each color channel and in mixed highs may be calculated from Equations (3). While the assumed noise sources in the expressions are voltage generators, in combination with the modifying impedance terms they represent noise currents.

The equivalent noise current in each color channel, calculated from Equation (1) with R assumed large, is represented as

$$\sqrt{4kTf_0}\sqrt{\frac{R_{eq}\omega_0^2C_0^2}{3}}, \tag{7}$$

where $f_0 = \omega_0/2\pi$ is the upper frequency limit of desired color information (taken as 1.3 megacycles); k, T, and R_{eq} are the same quantities previously defined; and C_0 is the total effective input capacitance. C_0 is determined by the coefficients of the noise terms in Equation (3a). Thus

$$C_0 = \sqrt{(2C_t + C)^2 + (C_t)^2 + (C_t)^2}, \tag{8}$$

or $C_0 \approx \sqrt{6}\ C_t$ for C much smaller than C_t. With $R_{eq} = 45$ ohms and $C_t = 600$ micromicrofarads, the equivalent noise current for each color channel is 0.00682 microampere. The signal-to-noise ratio is then 29 for a signal current of 0.2 microampere peak-to-peak in that channel. It has been assumed that beam noise from the camera tube is negligible.

The optimum signal-to-noise ratio for the high frequencies is evaluated by the sum of Equations (3).

$$I_g + I_r + I_b + \frac{1}{Z}(e_{ng} + e_{nr} + e_{nb}) = \frac{1}{Z}(V_g + V_r + V_b). \qquad (9)$$

Equation (1) is for a pass-band 0 to f_0. The corresponding expression for a pass-band f_1 to f_2 is easily derived and may be expressed:

$$I_n = \sqrt{4kT(f_2 - f_1)} \sqrt{\frac{1}{R} + \frac{R_{eq}}{R^2} + \frac{R_{eq}}{3X_{\bar{c}}^{-2}}} \qquad (10)$$

where $X_{\bar{c}} = \dfrac{1}{2\pi \bar{f} C}$ with $\bar{f} = \sqrt{f_1^2 + f_1 f_2 + f_2^2}$. From Equations (9) and (10), with R assumed large, the equivalent noise current in the mixed-highs channel is given by

$$2\pi \bar{f} C \sqrt{4kT(f_2 - f_1) R_{eq}}, \qquad (11)$$

where $f_2 = 4.2$ megacycles,

$f_1 = 1.3$ megacycles,

and $\bar{f} = 4.9$ megacycles.

Since C may be assumed to be 40 micromicrofarads, the equivalent noise current is 0.00182 microampere. The corresponding signal-to-noise ratio is then about 330 for a total signal of 0.6 microampere peak-to-peak.

RINGING IN HORIZONTAL-DEFLECTION AND HIGH-VOLTAGE TELEVISION CIRCUITS*

By

T. Murakami

RCA Victor Home Instruments
Camden, N. J.

Summary—An analytical study of the horizontal-deflection system for television shows that the transient ringing during the trace period of the deflection cycle can be eliminated by proper choice of circuit constants. Details of the solution are given so that the method of analysis and solution can be applied to other deflection systems. Experimental results that are given and the application of the theory to the design of horizontal-deflection systems verify the analysis presented. Information for the design of a specific deflection system with minimum ringing is presented in simplified form.

Introduction

THIS paper presents a theoretical analysis of the horizontal-deflection system of a television receiver. The purpose of the study is to determine the optimum circuit constants for a given horizontal-deflection system which would result in minimum ringing during scan with maximum high voltage during retrace. Previous authors[1] have shown that there is an optimum ratio between the resonant frequency of the scanning circuit and the resonant frequency of the high-voltage circuit. A more stringent design criterion for optimum performance is developed here.

The purpose of the horizontal-deflection system is to move the electron beam linearly across the face of the kinescope during the trace or scan period. During the retrace period the beam is returned to its initial position. United States television standards prescribe a total period of 63.5 microseconds between horizontal-synchronizing pulses. The normal station blanking and the variation of phase of the synchronizing signal in the receiver permit a maximum retrace time of approximately 9 microseconds in a receiver without retrace blanking. This permits a minimum trace time of approximately 54.5 microseconds. When retrace blanking is used, as in a color-television receiver, the maximum retrace time is approximately 13 microseconds.

* Manuscript received June 22, 1959.

[1] K. E. Martin and I. A. Whyte, "Line Timebase Circuits for 90° Scanning," *Mullard Technical Communications*, No. 14, p. 90, August 1955.

The driving current through the horizontal-yoke coils varies linearly with time during trace and is approximately sinusoidal during retrace when the circuit is reduced to its simplest form. When there is appreciable transient ringing in the high-voltage portion of the deflection system during the trace period, the ringing is reflected in the yoke circuit which in turn causes a light-intensity modulation on the kinescope raster. There are other important reasons why transient ringing during the trace period should be kept to a minimum; these are discussed later.

Qualitative Analysis of Basic Circuit

The basic horizontal-deflection circuit can be represented as shown in Figure 1. In this circuit, L_y and R_y represent the yoke inductance and resistance, C the distributed capacitance and externally added capacitance, and the switch S corresponds to the horizontal-output and damper tubes.

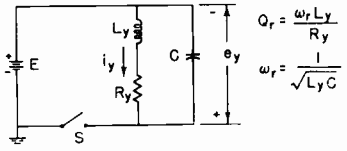

Fig. 1—Basic horizontal-deflection circuit.

The operation of the circuit can be explained qualitatively as follows. When the switch S is closed, the voltage E is impressed across the circuit, and the current i_y increases approximately linearly with time as shown in Figure 2(a). At a time t_1, corresponding to the end of the horizontal scan, the switch S is opened, and the retrace period is initiated. The voltage $-E$ on the capacitor first drops to zero in the time interval Δt as shown in Figure 2(b). During this interval, the current reaches its maximum value and all the energy in the circuit is in the form of magnetic energy.

Since the current through the inductance is finite at time t_1, there is a transient oscillation of the current in the parallel-tuned circuit. This transient occurs at a frequency very nearly equal to the resonant frequency ω_r of L_y and C. The rate at which the current changes in the inductance determines the voltage produced in the circuit. It is evident that the voltage across the capacitor during retrace can be much greater than the impressed voltage E, as shown in Figure 2(b). At time t_2 during the transient, the current i_y has decreased to zero

and the energy in the magnetic field has been transferred to the capacitor as potential energy. The current i_y then reverses and discharges the capacitor, returning the energy to the magnetic field in the reverse direction until the capacitor is completely discharged at $t_3 - \Delta t$. The magnetic field then begins to collapse, and at time t_3 the voltage on the capacitor is again charged to $-E$, the switch is reclosed, and another trace period begins.

Since the current during the time interval from t_3 to t_4 shown in Figure 2(a) is negative, the battery is being charged during this

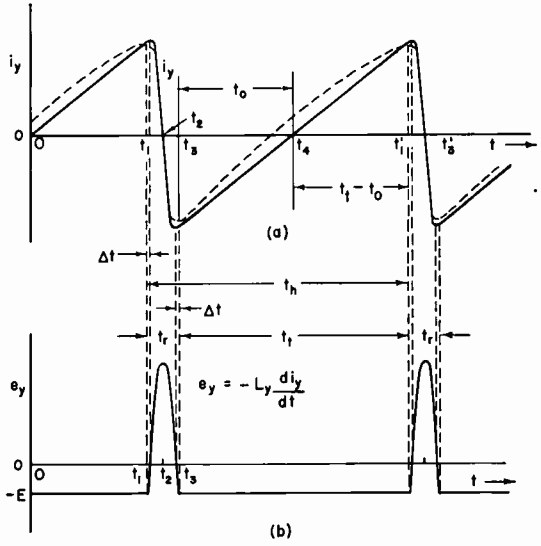

Fig. 2—Current and voltage waveforms in horizontal-deflection yoke.

interval. It is evident that if there are no losses in the circuit, the current waveshape will have odd symmetry about the time t_4. If there are losses in the circuit, more energy must be supplied during the interval $t_t - t_0$ when the battery is connected to the circuit. This corresponds to shifting the current curve as shown by the dashed line in Figure 2(a).

Practical Deflection Circuit

The basic circuit of Figure 1 is not suited to the power supply and tubes available for television receivers; therefore, a circuit such as that shown in Figure 3 is normally used. This circuit makes use of an autotransformer to couple the horizontal output tube, V_1, to the

yoke, L_y. The high voltage for the kinescope is obtained by means of a tertiary winding on the transformer which autotransforms the yoke pulse to a high value. A diode, V_2, rectifies this pulse for the high-voltage supply. The energy stored in the magnetic field of the yoke is returned to the capacitor C_B by current flowing from the yoke through the damper diode V_3 during the first part of the trace period. If C_B is large enough to prevent an appreciable change in the voltage E across it during the cycle, the capacitor can be considered as similar to a battery with no direct current flowing through it. In this case, C_B corresponds to the battery E of Figure 1 and is added in series with the power supply B to provide "B boost."

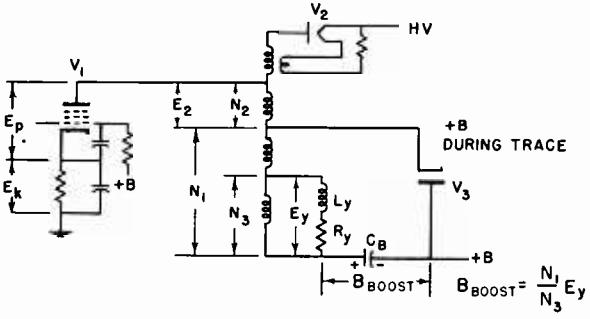

Fig. 3—Simplified horizontal-deflection circuit.

B boost is generally more than twice the power-supply voltage, and a few milliamperes can be drained from it to supply other circuits in the receiver that require very high power-supply voltages. Since this power is generated by means of a high-power pentode and diode, it is not economical for use in circuits that can operate from a normal power supply.

The control grid of the output tube is driven by a sawtooth waveform such as that shown in Figure 4. Since the tube is grid-leak biased, the tips of the driving sawtooth just reach grid current. The conduction time of the output tube is determined by the amplitude of the driving waveform. As shown in Figure 4, the amplitude of the drive is adjusted to permit the conduction time to just equal $t_f - t_0$. During the time interval t_0, the grid is sufficiently negative so that the output tube is cut off.

A typical operating loadline of a horizontal-output tube is shown in Figure 5. At the beginning of the trace period, the current and voltage are at point (a) of Figure 5. When the output tube begins

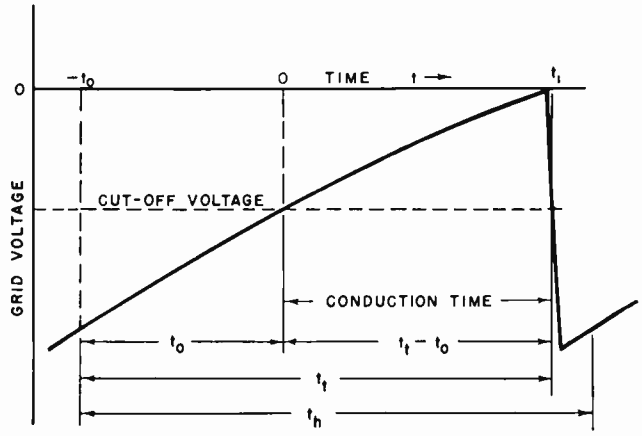

Fig. 4—Grid-voltage waveform.

to conduct, the current increases from (a) until it reaches a maximum at point (b) at the end of the trace period. At this point the output tube is cut off and the retrace pulse develops along the path (bcd). The path (bc) is not concisely defined here since it is dependent on the cutoff characteristic of the tube, but the time for the current to reach zero is in the order of 1 microsecond. The pulse then returns from (d) to (a) and the deflection cycle is completed.

The region to the left of the knee of the plate-current curve of Figure 5 is a region of instability. At high values of plate current in tetrodes or beam power tubes, as in the uppermost curve of Figure 5, a decrease in the plate voltage may cause the plate current to decrease

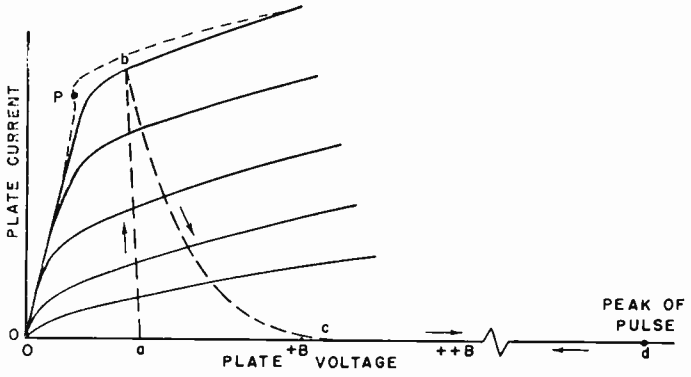

Fig. 5—Operating loadline of output tube.

along a curve indicated by the dashed line. It can be seen that at point P, there is an abrupt change in the plate current; at this point, the tube goes into a Barkhausen type of radio-frequency oscillation producing the so-called snivet.[2] The snivet is noted when the r-f oscillation is picked up by the receiver tuner or i-f circuits causing picture disturbance. When ringing of sufficient magnitude from the high-voltage circuit is reflected into the deflection circuit during the latter part of the trace period, the operating point may be shifted to the left of the knee and thereby produce snivets.

If transient ringing is present during the latter portion of the trace period, the plate voltage should be made sufficiently large so that the operating load line does not have an excursion to the left of the knee. Thus, minimum ringing during the trace portion of the deflection cycle is desired, since an improvement in the efficiency of the system can be obtained if the plate-supply voltage can be lowered.

Equivalent Circuit for Practical Deflection System

The practical deflection circuit shown in Figure 3 may be approximated by the equivalent circuit shown in Figure 6. The switch S is

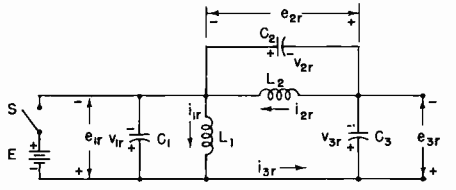

Fig. 6—Equivalent deflection circuit during retrace.

open during the retrace period and closed during the trace period. All circuit elements are referred to the high-voltage side of the autotransformer. The inductance L_1 is the equivalent inductance of the transformer windings and deflection yoke referred to the high-voltage side of the transformer. C_1 is the equivalent capacitance of the transformer windings, yoke winding, and output tube. Since the tertiary winding which supplies the high voltage is necessarily narrow in width to minimize the distributed capacitance, a relatively high leakage inductance L_2 appears between the yoke winding and the high-voltage winding. C_2 is the equivalent stray capacitance across L_2, and C_3 is the capacitance which appears across the high-voltage terminal.

[2] M. B. Knight, "Meet the Snivet," *Radio and Television News*, Vol. 50, No. 5, p. 104, November 1953.

For clarity, the instantaneous voltage across the equivalent yoke inductance L_1 during retrace is denoted by e_{1r}. Similarly, the instantaneous voltages across the leakage inductance L_2 and high voltage capacitance C_3 during the retrace interval are respectively e_{2r} and e_{3r}. The corresponding instantaneous currents are denoted by i_{1r}, i_{2r}, and i_{3r}.

With the switch S open, the circuit equations for Figure 6 may be written in differential form during retrace as

$$L_1 \frac{di_{1r}}{dt} - \frac{1}{C_1} \int_0^t (i_{3r} - i_{1r})\, dt + v_{1r} = 0 \tag{1}$$

$$L_2 \frac{di_{2r}}{dt} + \frac{1}{C_1} \int_0^t (i_{3r} - i_{1r})\, dt - v_{1r} + \frac{1}{C_3} \int_0^t i_{3r}\, dt + v_{3r} = 0 \tag{2}$$

$$L_2 \frac{di_{2r}}{dt} - \frac{1}{C_2} \int_0^t (i_{3r} - i_{2r})\, dt + v_{2r} = 0 \tag{3}$$

$$e_{3r} - \frac{1}{C_3} \int_0^t i_{3r}\, dt - v_{3r} = 0 \tag{4}$$

where the instantaneous currents and initial voltages v_{1r}, v_{2r}, and v_{3r} at $t = 0$ are as indicated in Figure 6. Using the Laplace transform method as shown in Appendix I, Equations (1) to (4) can be solved to obtain the equations for the transformed voltages E_{1r}, E_{2r}, and E_{3r} as functions of the complex variable p. Similarly, the transformed equations for the yoke and leakage currents I_{1r} and I_{2r} can also be found for the retrace period. All of the equations during the retrace period can be written in the form

$$F(p) = K \frac{p^3 + a_2 p^2 + a_1 p + a_0}{(p^2 + \beta^2)(p^2 + \lambda^2)} \tag{5}$$

where K, β, λ, and the a's are determined by the circuit constants and initial voltages and currents. The time function corresponding to Equation (5) is of the form

$$f(t) = \frac{K}{\beta^2 - \lambda^2} \left[\frac{a_2\beta^2 - a_0}{\beta} \sin \beta t + (\beta^2 - a_1) \cos \beta t + \frac{a_0 - a_2\lambda^2}{\lambda} \sin \lambda t + (a_1 - \lambda^2) \cos \lambda t \right]. \tag{6}$$

It is seen from Equation (6) that during the retrace interval there are two frequencies of oscillation in the current and voltage waveforms. The lower of the two frequencies is determined by L_1 resonating in parallel with C_1 and the capacitive path of $L_2C_2C_3$. The other resonant frequency is due to L_2 in parallel resonance with C_2 and the capacitive path $C_3L_1C_1$. The exact equations for the frequencies are given in Appendix I. In the practical case, the ratio of the two frequencies lies between 2.7 and 3.0.

The trace period is initiated when the switch S is closed, as shown in Figure 7. The currents and voltages during the trace period are identified by the subscript t. Since a constant voltage is applied to

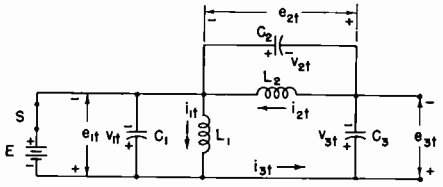

Fig. 7—Equivalent deflection circuit during trace.

the equivalent yoke inductance L_1, the equation for this circuit is

$$e_{1t} = -E = v_{1t} = -L_1 \frac{di_{1t}}{dt}. \tag{7}$$

Integrating Equation (7) gives the instantaneous yoke current during trace as

$$i_{1t} = -\frac{v_{1t}}{L_1} t + i_{1r}(t_r) \tag{8}$$

where the initial current for the trace period is the yoke current at the end of the retrace time t_r.

The differential equations for the leakage and high-voltage circuit with the switch S closed are

$$e_{3t} = \frac{1}{C_3} \int_0^t i_3 \, dt + v_{3t} \tag{9}$$

$$e_{3t} = -L_2 \frac{di_{2t}}{dt} + v_{1t} \tag{10}$$

$$L_2 \frac{di_{2t}}{dt} - \frac{1}{C_2} \int_0^t (i_{3t} - i_{2t})\, dt + v_{2t} = 0. \tag{11}$$

When Equations (9), (10), and (11) are solved simultaneously as shown in Appendix I, the instantaneous leakage current and voltage can be written in the form

$$f(t) = k_1 \left(\frac{h_0}{\delta} \sin \delta t + \cos \delta t \right) \tag{12}$$

where k_1, h_0, and δ are determined by the circuit constants and the voltages and currents at the beginning of the trace period. The frequency δ is determined by resonance of L_2 with C_2 and C_3 in parallel. The equation for the high voltage during the trace interval is

$$e_{3t} = v_{3t} \left[\frac{u_0}{\delta^2} - \frac{u_0 - \delta^2}{\delta^2} \cos \delta t + \frac{u_1}{\delta} \sin \delta t \right] \tag{13}$$

u_0 and u_1 being determined by the initial conditions and the circuit constants.

Steady-State Solution for Repeating Transient

The horizontal-deflection problem analyzed above involves the steady-state solution of a repeating transient. To briefly review the problem, let us consider the sequence of events. A set of initial voltages and currents are assumed at the beginning of the retrace period. As shown in Figure 2, the voltage across the yoke inductance starts at a voltage $-E$ when the switch S is opened. The circuit oscillates for approximately one half cycle during the retrace period, t_r. At the end of the retrace period, the yoke voltage is again at $-E$, the switch is closed, and another trace period, t_t, is initiated. The final conditions for the retrace period are the initial conditions for the trace period. Thus for the yoke current, $i_{1r}(t_r)$ is equal to $i_{1t}(0)$.

The current in the yoke during the trace period increases linearly in accordance with Equation (8). At the end of trace, the current $i_{1t}(t_t)$ is equal to the initial yoke current $i_{1r}(0)$ for the retrace cycle if all of the initial conditions have been properly chosen. This implies that the system has reached the steady-state condition. Similarly, the current i_2 and the voltage e_2 associated with the leakage inductance L_2 must be followed through the retrace cycle. In this way the current $i_{2r}(t_r)$ and the voltage $e_{2r}(t_r)$ which are the initial conditions $i_{2t}(0)$

and $e_{2t}(0)$ for the trace period are obtained. Using these initial conditions for the trace period in equations of the form given by Equation (12), the current $i_{2t}(t_t)$ and voltage $e_{2t}(t_t)$ are found. The current $i_{2t}(t_t)$ equals $i_{2r}(0)$, and the voltage $e_{2t}(t_t)$ equals v_{2r} when the steady-state condition is reached.

Since the circuit constants which result in minimum ringing during the trace period are desired, values of circuit constants from a practical design can be used as a starting point. In the method of solution used, appropriate values of the initial voltages and currents at the beginning of the retrace cycle were assumed. With a given set of horizontal-deflection requirements, the transformed supply voltage E and the desired trace and retrace times can be assumed to be known. For a given yoke inductance L_1, the maximum yoke current $i_{1t}(t_t)$ can be calculated by use of Equation (8). As the system has been assumed to be lossless, the current and voltage waveforms during retrace will be symmetrical in the steady-state condition. Thus

$$i_{1t}(t_t) = -i_{1r}(t_r) = -i_{1t}(0). \tag{14}$$

From Equations (8) and (14),

$$\begin{aligned} i_{1t}(t_t) &= \frac{E}{L_1} t_t + i_{1r}(t_r) \\ &= \frac{Et_t}{2L_1}. \end{aligned} \tag{15}$$

Any convenient value can be assumed for the current $i_{2r}(0)$ and the voltage v_{2r} to start the solution.

To facilitate computation of the steady-state condition for the repeating transient, a digital computer was used to find the various currents and voltages during the deflection cycle. For the given set of circuit constants, the exact value for the retrace time must be determined by solving Equation (6) for t_r with $f(t)$ equal to $-E$ and the appropriate constants for the yoke voltage $e_{1r}(t)$. The details of the solution are shown in Appendix II. Equation (6) must be solved for t_r for every complete horizontal-deflection cycle, since the retrace period will change from cycle to cycle as the initial conditions change with each cycle. Since the retrace time t_r changes, the trace time will also change in accord with (as applied to a color deflection system $t_h = 63.6 \times 10^{-6}$)

$$t_t = 63.6 \times 10^{-6} - t_r. \tag{16}$$

The new value of t_t corresponding to t_r must be used during the trace period.

Since no damping was introduced into the equivalent circuits shown in Figures 6 and 7, the solution as outlined above will not lead to a satisfactory steady-state solution. If the initial conditions for the second cycle are obtained by averaging the final conditions for the first cycle with the corresponding initial conditions, a satisfactorily converging solution is obtained.

Circuit Constants for Minimum Ringing During Trace

After the steady-state solution for a given set of constants has been found, the problem becomes one of determining the particular

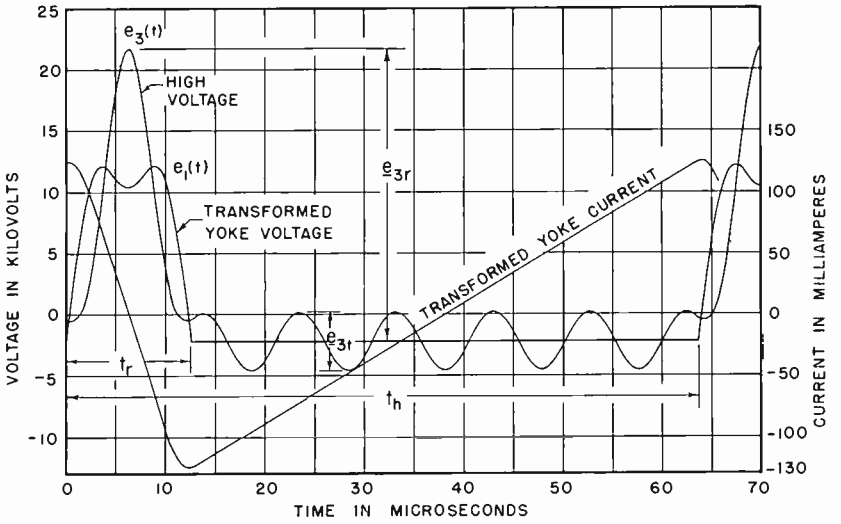

Fig. 8—Horizontal-deflection voltage and current waveforms with ringing during trace. Circuit constants (transformed to high-voltage side of transformer): $L_1 = .450$ h, $L_2 = .200$ h, $C_1 = 20$ $\mu\mu$f, $C_2 = 2$ $\mu\mu$f, $C_3 = 10$ $\mu\mu$f, $t_r = 12.652$ μsec, $(B/\lambda) = 2.945$, and $R = (e_{3r}/e_{3t}) = 5.01$.

set of constants that will result in minimum ringing of the high voltage during trace period. With the set of circuit constants originally chosen, a set of voltage and current waveforms such as that shown in Figure 8 was obtained. It was decided to keep E, L_1, C_2, C_3, and t_r constant in order to reduce the number of variable quantities to a minimum. The minimum ringing condition was then found by systematically varying L_2 and compensating for the change in retrace time by adjusting C_1 to the proper value. To determine the exact

circuit behavior, it was necessary to find the steady-state condition for the repeating transient for each value of L_2. Since maximum high voltage during retrace is desired in addition to minimum ringing, the ratio, R, of the peak of the high voltage to the amplitude of the ringing was determined for each value of L_2. Changes in L_2 were continued until a maximum value was obtained for the ratio R. Figure 9 shows the steady-state waveforms for minimum ringing during trace and maximum high voltage during retrace for a retrace time of 12.65

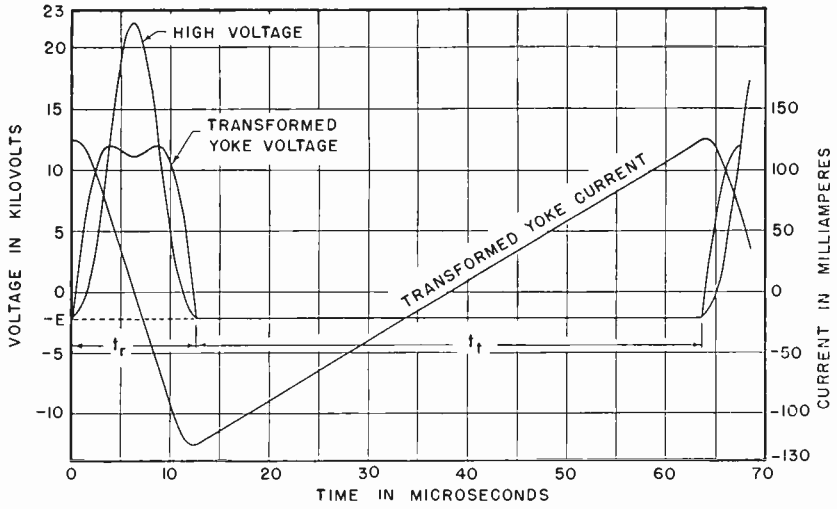

Fig. 9—Horizontal-deflection voltage and current waveforms with minimum ringing during trace. Circuit constants (transformed to high-voltage side of transformer): $L_1 = .450$ h, $L_2 = .240$ h, $C_1 = 18.92$ $\mu\mu$f, $C_2 = 1.565$ $\mu\mu$f, $C_3 = 9.38$ $\mu\mu$f, $t_r = 12.646$ μsec, $(B/\lambda) = 2.78$, and $R = 3725$.

microseconds. In Figure 10 the waveforms are shown for a set of circuit constants when the retrace time was made 10 microseconds.

It is noted that as the retrace time is decreased, the amplitude of the high voltage is increased if the applied battery voltage E is kept constant. This is due to the fact that the average d-c voltage in the system is zero, i.e., the area below the zero-voltage axis is equal to the area above the axis. By similar reasoning, it can be shown that the area above the dashed line in Figure 9 is the same for e_1 and e_3. As the retrace time is decreased, this area remains a constant for a given battery voltage E. Thus the area above the dashed line in Figure 10 is equal to the corresponding area shown in Figure 9. As a result of the area relationships, if the waveshapes of the voltage e_3 in Figures

9 and 10 are the same, the peak voltages above $-E$ are inversely proportional to the retrace times.

There is no unique solution for the minimum-ringing condition for a given retrace time and a given value of equivalent yoke inductance. There are many optimum circuit-value combinations of leakage inductance L_2, the capacitance C_1, and the high-voltage capacitance C_3 for a given retrace time and yoke inductance. Each of these circuit-value combinations gives a different retrace waveform. Figure 11

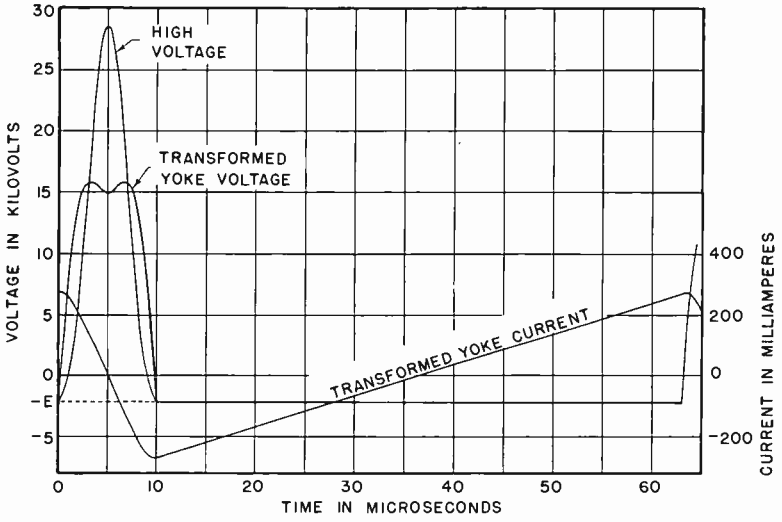

Fig. 10—Horizontal-deflection voltage and current waveforms with minimum ringing during trace. Transformed circuit constants: $L_1 = .220$ h, $L_2 = .115$ h, $C_1 = 26$ $\mu\mu$f, $C_2 = 2$ $\mu\mu$f, $C_3 = 12$ $\mu\mu$f, $t_r = 10$ μsec, $(B/\lambda) = 2.83$, and $R = 2990$.

shows the current and voltage waveforms for a retrace time of 9 microseconds in which the yoke voltage shows a pronounced valley. A family of curves of the yoke voltage as a function of the high-voltage capacitance C_3 is shown in Figure 12. In this case, the retrace time was held at 12.65 microseconds, the yoke inductance at 450 millihenries, and the equivalent capacitance C_2 of the leakage inductance at 2 micromicrofarads. The parameters L_2 and C_1 were varied to maintain the retrace time and keep the ringing to a minimum. For these examples, the solution was not carried out to the optimum condition of zero ringing during the trace period. The curves show that as the high-voltage capacitance C_3 is increased, the yoke voltage e_1 develops a deeper valley while the high voltage e_3 remains essentially the same.

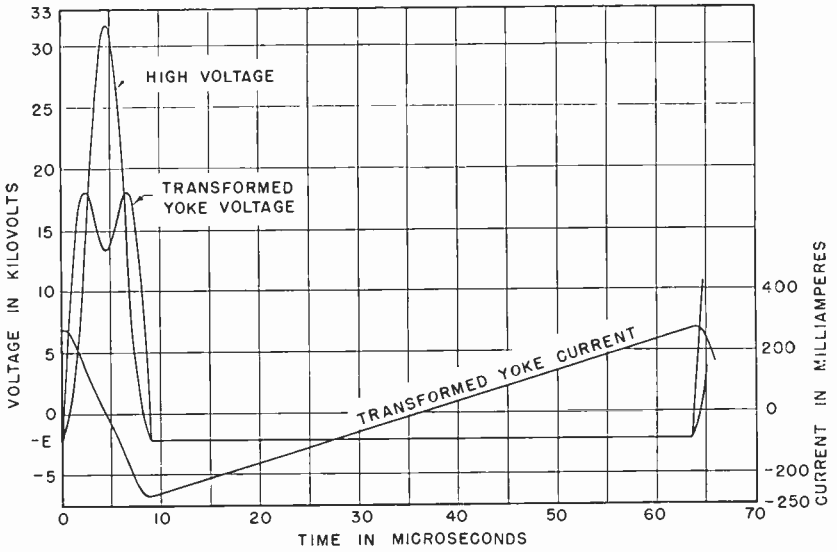

Fig. 11—Horizontal-deflection voltage and current waveforms with minimum ringing during trace. Transformed circuit constants: $L_1 = .220$ h, $L_2 = .106$ h, $C_1 = 17.4$ $\mu\mu$f, $C_2 = 2$ $\mu\mu$f, $C_3 = 12.6$ $\mu\mu$f, $t_r = 9$ μsec, $(B/\lambda) = 2.84$, and $R = 820$.

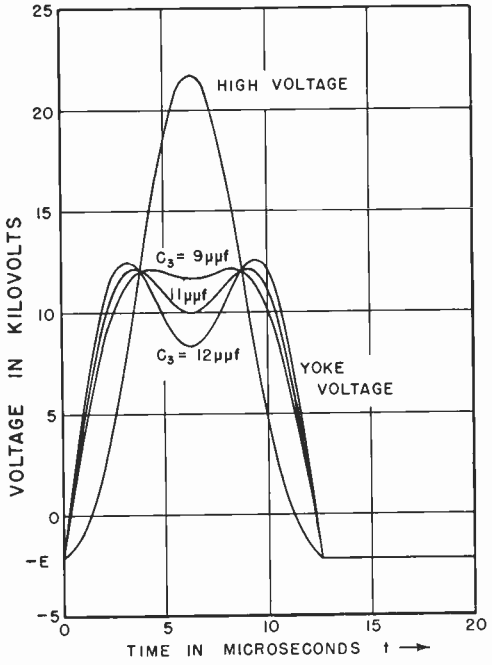

Fig. 12—Variation of yoke voltage with high-voltage capacitance.

Equations for Minimum Ringing Circuit Constants

A study of the circuit equations as given in Appendix III shows that the circuit constants resulting in minimum ringing may be scaled for any impedance level and any retrace time. The circuit constants derived in this manner, however, are only valid for the horizontal deflection period of 63.6 microseconds. For any other deflection period the problem must be re-solved in the manner illustrated in the previous sections.

To change the impedance $\sqrt{L_1/C_1}$ by a factor k, each inductance must be multiplied by k and each capacitance must be divided by k:

Thus
$$L' = kL, \tag{17}$$

and
$$C' = \frac{C}{k}, \tag{18}$$

where L and C are the original values and L' and C' are the new values. If the retrace time is to be changed by a factor η, the inductance and capacitance must each be multiplied by η. The new values are then

$$L' = \eta L, \tag{19}$$

and
$$C' = \eta C. \tag{20}$$

When both the impedance and retrace time are changed simultaneously,

$$L' = k\eta L, \tag{21}$$

and
$$C' = \frac{\eta C}{k}. \tag{22}$$

Example Using Scale-Change Equations

Starting with the circuit constants as given in Figure 10, the circuit constants for another impedance level and retrace time can be found by use of Equations (21) and (22). Let the new equivalent yoke inductance be 450 millihenries and the new retrace time be 12.65 microseconds. Since the retrace time given is 10 microseconds, the factor η is 12.65/10 or 1.265. Equation (21) yields a value of k

$$k = \frac{L'}{\eta L} = \frac{.450}{1.265 \times .220} = 1.617. \tag{23}$$

With $k = 1.617$ and $\eta = 1.265$,

$$L_2' = k\eta L_2 = 0.235 \text{ henry} \qquad C_1' = \frac{\eta C_1}{k} = 20.3\ \mu\mu\text{f}$$

$$C_2' = \frac{\eta C_2}{k} = 1.565\ \mu\mu\text{f} \qquad C_3' = \frac{\eta C_3}{k} = 9.39\ \mu\mu\text{f}. \tag{24}$$

These circuit element values are very close to the final values shown in Figure 9 which were obtained by optimizing the values shown above for the minimum ringing condition. In a practical design, the circuit element values given by Equations (24) would be sufficiently accurate for an initial design. The value of the capacitance C_2 is not very critical since its impedance is relatively high compared with that for the inductance L_2 at the lower resonant frequency. At the higher resonant frequency, the capacitance C_2 is added in shunt with a much higher value of capacitance so that its effect is minimized.

The peak of the high voltage $\hat{e}_3$ associated with Figure 9 may be approximated from that shown in Figure 10 by the relation

$$\hat{e}_3' + E = \frac{1}{\eta}\,(\hat{e}_3 + E), \tag{25}$$

which states that the voltage above $-E$ is inversely proportional to the retrace time. Equation (25) gives

$$\hat{e}_3' = \frac{1}{1.265}\,(28{,}500 + 2{,}200) - 2{,}200 = 22{,}050$$

which agrees with the value for the peak of the high voltage shown in Figure 9.

Experimental Results

The theoretical analysis was substantiated experimentally by use of the test circuit shown in Figure 13. In this circuit, a periodic pulse input to the first stage is converted to the waveform shown at the grid of the driver tube. The 6CL6 tube is normally cut off by sufficient cathode bias. When a positive pulse is applied to the grid of this tube, the capacitor C is discharged through the low-impedance path presented by the 6CL6. Because the pulse input to the 6CL6 tube is variable in width and repetition rate, the optimum conditions can be found for a given deflection system. Figures 14 to 16 show the voltage waveforms for a deflection system for several different conditions. In each of the figures, the yoke voltage, a voltage proportional to that across the leakage inductance ($e_3 - e_1$), and a voltage proportional to the high voltage are shown. Figure 14 shows the condition where the retrace period is slightly smaller than the optimum value. In this

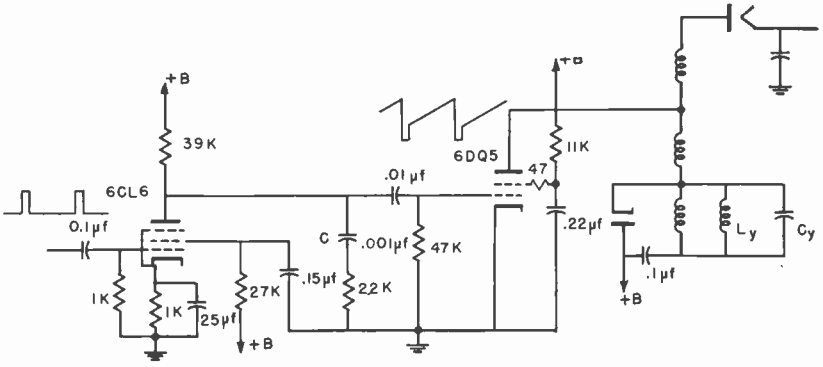

Fig. 13—Circuit for testing zero ringing condition.

case, ringing of the high voltage during the trace period is quite evident. There is a similar ringing of the voltage across the leakage inductance during trace as shown in Figure 14(b). In Figure 15 the conditions are optimum so that there is zero ringing during the trace period. When the retrace period is made slightly greater than that used for Figure 15 and all other quantities remain constant, the curves shown in Figure 16 result. The results shown here and the application of the theory to the design of horizontal-deflection systems verify the analysis presented.

YOKE VOLTAGE = e_1
(a)

$e_3 - e_1$
(b)

HIGH VOLTAGE = e_3
(c)

FIG. 14 VOLTAGE WAVEFORMS OF DEFLECTION SYSTEM WITH RETRACE PERIOD TOO SMALL

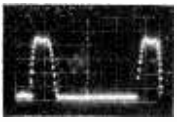

YOKE VOLTAGE = e_1
(a)

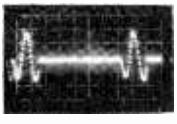

$e_3 - e_1$
(b)

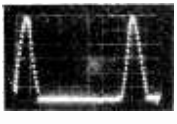

HIGH VOLTAGE = e_3
(c)

FIG. 15 VOLTAGE WAVEFORMS OF DEFLECTION SYSTEM WITH OPTIMUM RETRACE PERIOD.

YOKE VOLTAGE = e_1
(a)

$e_3 - e_1$
(b)

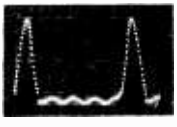

HIGH VOLTAGE = e_3
(c)

FIG. 16 VOLTAGE WAVEFORMS OF DEFLECTION SYSTEM WITH RETRACE PERIOD TOO LARGE.

Conclusions

In the past, the transient ringing during the trace period was not eliminated at the source but was minimized by addition of components. It has been shown here that the ringing can be eliminated by proper choice of the essential circuit elements. Information to be used in the design of a deflection system without ringing during trace has been presented in a simplified form. The circuit constants can be scaled so that the solution applies for different retrace times and impedance levels. The results are applicable to systems using a horizontal scan period of 63.6 microseconds, but the same method of solution can be applied for other periods. This method involves the steady-state solution of a repeating transient in a lossless system.

With the elimination of the transient ringing during the trace period, the problem of "snivets" is solved. The efficiency of the horizontal deflection system is also improved because a lower supply voltage is required when there is no ringing reflected to the plate circuit of the driver tube.

Acknowledgments

The author wishes to acknowledge the contributions to this study made by R. F. Kolar, L. E. Annus, B. V. Vonderschmitt, and C. C. Iden of RCA Victor Home Instruments. R. F. Kolar carried out the computer programming and solution of the problem. L. E. Annus performed the experimental work, and B. V. Vonderschmitt originally proposed the problem. Some sections of this paper are based on lecture notes on the horizontal-deflection system prepared by C. C. Iden.

Appendix I

Solution of Circuit Equations During Retrace

The circuit equations for Figure 6 with the switch S open can be written in differential form as

$$e_{3r} - \frac{1}{C_3}\int_0^t i_{3r}\,dt - v_{3r} = 0, \tag{26}$$

$$L_1\frac{di_{1r}}{dt} - \frac{1}{C_1}\int_0^t (i_{3r} - i_{1r})\,dt + v_{1r} = 0, \tag{27}$$

$$L_2\frac{di_{2r}}{dt} + \frac{1}{C_1}\int_0^t (i_{3r} - i_{1r})\,dt - v_{1r} + \frac{1}{C_3}\int_0^t i_{3r}\,dt + v_{3r} = 0, \tag{28}$$

$$L_2 \frac{di_{2r}}{dt} - \frac{1}{C_2} \int_0^t (i_{3r} - i_{2r})\, dt + v_{2r} = 0, \tag{29}$$

where v_{1r}, v_{2r}, and v_{3r} are the initial voltages during retrace on the capacitors C_1, C_2, and C_3, respectively.

Taking the Laplace transforms[3] of Equations (26), (27), (28), and (29),

$$E_{3r}(s) - \frac{1}{C_3 s} I_{3r}(s) - \frac{v_{3r}}{s} = 0, \tag{30}$$

$$L_1 s I_{1r}(s) - L_1 i_{1r}(0) - \frac{1}{C_1 s} \left[I_{3r}(s) - I_{1r}(s) \right] + \frac{v_{1r}}{s} = 0, \tag{31}$$

$$L_2 s I_{2r}(s) - L_2 i_{2r}(0) + \frac{1}{C_1 s} \left[I_{3r}(s) - I_{1r}(s) \right] - \frac{v_{1r}}{s} + \frac{1}{C_3 s} I_{3r}(s) + \frac{v_{3r}}{s} = 0, \tag{32}$$

$$L_2 s I_{2r}(s) - L_2 i_{2r}(0) - \frac{1}{C_2 s} \left[I_{3r}(s) - I_{2r}(s) \right] + \frac{v_{2r}}{s} = 0, \tag{33}$$

where $i_{1r}(0)$ and $i_{2r}(0)$ are the currents in the inductances L_1 and L_2 at time equal to zero. By solving Equations (30) to (33) simultaneously, the equations for the various voltages and currents are obtained. For purposes of convenience, we let $A = C_1C_2 + C_1C_3 + C_2C_3$. The transform of the yoke voltage during retrace is then

$$E_{1r}(s) = \frac{\begin{array}{c} L_1\{L_2 A v_{1r} s^3 + L_2[i_{1r}(0)(C_2+C_3)] - i_{2r}(0) C_3 s^2 \\ + (C_1 v_{1r} + C_3 v_{1r} + C_3 v_{2r}) s + i_{1r}(0)\} \end{array}}{\{L_1 L_2 A s^4 + (L_1C_1 + L_2C_2 + L_1C_3 + L_2C_3) s^2 + 1\}}. \tag{34}$$

The corresponding transformed yoke current is expressed as

$$I_{1r}(s) = \frac{\begin{array}{c} \{L_1 L_2 A i_{1r}(0) s^3 - L_2 A v_{1r} s^2 \\ + [L_1C_1 i_{1r}(0) + L_1C_3 i_{1r}(0) + L_2C_3 i_{2r}(0)] s \\ - (C_1 v_{1r} + C_3 v_{1r} + C_3 v_{2r})\} \end{array}}{\{L_1 L_2 A s + (L_1C_1 + L_2C_2 + L_1C_3 + L_2C_3) s^2 + 1\}}. \tag{35}$$

[3] M. F. Gardner and J. L. Barnes, *Transients in Linear Systems*, Vol. 1, p. 126, John Wiley and Sons Inc., New York, N. Y., 1942.

A voltage with a transform $E_{2r}(s)$ exists across the leakage inductance L_2 during retrace. This transformed voltage

$$E_{2r}(s) = \frac{\begin{array}{c} -L_2\{L_1v_{2r}As^3 - L_1[C_3i_{1r}(0) - C_1i_{2r}(0) - C_3i_{2r}(0)]s^2 \\ + (C_2v_{2r}+C_3v_{1r}+C_3v_{2r})s + i_{2r}(0)\} \end{array}}{\{L_1L_2As^4 + (L_1C_1+L_2C_2+L_1C_3+L_2C_3)s^2 + 1\}} \tag{36}$$

has an associated leakage current, the transform of which is

$$I_{2r}(s) = \frac{\begin{array}{c} \{L_1L_2Ai_{2r}(0)s^3 - L_1Av_{2r}s^2 \\ + [L_1C_3i_{1r}(0) + L_2C_2i_{2r}(0) + L_2C_3i_{2r}(0)]s \\ - (C_2v_{2r}+C_3v_{1r}+C_3v_{2r})\} \end{array}}{\{L_1L_2As^4 + (L_1C_1+L_2C_2+L_1C_3+L_2C_3)s^2 + 1\}}. \tag{37}$$

The transform of the high voltage $E_{3r}(s)$ during the retrace period is the difference between $E_{1r}(s)$ and $E_{2r}(s)$ or

$$E_{3r}(s) = \frac{\begin{array}{c} \{L_1L_2A(v_{1r}+v_{2r})s^3 + L_1L_2[C_2i_{1r}(0) + C_1i_{2r}(0)]s^2 \\ + [L_1C_1v_{1r}+L_2C_2v_{2r}+C_3(L_1+L_2)(v_{1r}+v_{2r})]s \\ + L_1i_{1r}(0) + L_2i_{2r}(0)\} \end{array}}{\{L_1L_2As^4 + (L_1C_1+L_2C_2+L_1C_3+L_2C_3)s^2 + 1\}}. \tag{38}$$

It is noted that all the transformed voltages and currents during the retrace period can be expressed in the form

$$F(s) = K\frac{s^3 + a_2s^2 + a_1s + a_0}{(s^2+\beta^2)(s^2+\lambda^2)} \tag{39}$$

where the a's are constants determined by the circuit parameters and initial conditions.

For the yoke voltage the particular constants are

$$K = v_{1r}, \qquad a_0 = \frac{i_{1r}(0)}{L_2Av_{1r}},$$

$$a_1 = \frac{C_1v_{1r}+C_3v_{1r}+C_3v_{2r}}{L_2Av_{1r}}, \qquad a_2 = \frac{i_{1r}(0)(C_2+C_3) - i_{2r}(0)C_3}{Av_{1r}}. \tag{40}$$

The angular frequencies of oscillation β and λ are the same for all the voltages and currents during the retrace period. These are

$$\beta^2 = \frac{L_1C_1+L_2C_2+L_1C_3+L_2C_3+\sqrt{(L_1C_1+L_2C_2+L_1C_3+L_2C_3)^2-4L_1L_2A}}{2L_1L_2A} \tag{41}$$

$$\lambda^2 = \frac{L_1C_1+L_2C_2+L_1C_3+L_2C_3-\sqrt{(L_1C_1+L_2C_2+L_1C_3+L_2C_3)^2-4L_1L_2A}}{2L_1L_2A} \tag{42}$$

For convenience the corresponding constants of Equation (39) for all the voltages and currents have been tabulated in Table I.

Taking the inverse Laplace transform of Equation (39) results in the time function

$$f(t) = \frac{K}{\beta^2-\lambda^2}\left[\frac{a_2\beta^2-a_0}{\beta}\sin\beta t + (\beta^2-a_1)\cos\beta t + \frac{a_0-a_2\lambda^2}{\lambda}\sin\lambda t + (a_1-\lambda^2)\cos\lambda t\right]. \tag{43}$$

Equation (43) with the proper constants for the particular current or voltage as given in Table I describes the waveforms during the retrace cycle.

Solution of Circuit Equations During Trace

The equations for the trace period can be obtained from the equivalent circuit shown in Figure 7 with the switch S closed. In the yoke circuit a constant voltage is applied across a pure inductance so that

$$E = L_1\frac{di_{1t}}{dt}. \tag{44}$$

When Equation (44) is integrated,

$$i_{1t}(t) = -\frac{v_{1t}}{L_1}t + i_{1r}(t_r), \tag{45}$$

where $E = -v_{1t}$ and the initial current for the trace period is equal to the retrace yoke current at time t_r.

The differential equations for the leakage and high-voltage circuit are

$$e_{3t} - \frac{1}{C_3}\int_0^t i_{3t}dt - v_{3t} = 0, \tag{46}$$

TABLE I—Constants for Equation (39)

$(A \equiv C_1C_2 + C_1C_3 + C_2C_3)$

$F(s)$	K	a_0	a_1	a_2
$E_{1r}(s)$	v_{1r}	$\dfrac{i_{1r}(0)}{L_2Av_{1r}}$	$\dfrac{C_1v_{1r} + C_3v_{1r} + C_3v_{2r}}{L_2Av_{1r}}$	$\dfrac{i_{1r}(0)\,(C_2+C_3) - i_{2r}(0)\,C_3}{Av_{1r}}$
$I_{1r}(s)$	$i_{1r}(0)$	$\dfrac{-(C_1v_{1r}+C_3v_{1r}+C_3v_{2r})}{L_1L_2Ai_{1r}(0)}$	$\dfrac{L_1C_1i_{1r}(0) + L_1C_3i_{1r}(0) + L_2C_3i_{2r}(0)}{L_1L_2Ai_{1r}(0)}$	$\dfrac{-v_{1r}}{i_{1r}(0)\,L_1}$
$E_{2r}(s)$	$-v_{2r}$	$\dfrac{i_{2r}(0)}{L_1v_{2r}A}$	$\dfrac{C_2v_{2r} + C_3v_{1r} + C_2v_{2r}}{L_1v_{2r}A}$	$\dfrac{-C_3i_{1r}(0) + C_1i_{2r}(0) + C_3i_{2r}(0)}{v_{2r}A}$
$I_{2r}(s)$	$i_{2r}(0)$	$\dfrac{-(C_2v_{2r}+C_3v_{1r}+C_3v_{2r})}{L_1L_2Ai_{2r}(0)}$	$\dfrac{L_1C_3i_{1r}(0) + L_2C_2i_{2r}(0) + L_2C_3i_{2r}(0)}{L_1L_2Ai_{2r}(0)}$	$\dfrac{-v_{2r}}{L_2i_{2r}(0)}$
$E_{3r}(s)$	$v_{1r}+v_{2r}$	$\dfrac{L_1i_{1r}(0) + L_2i_{2r}(0)}{L_1L_2A\,(v_{1r}+v_{2r})}$	$\dfrac{L_1C_1v_{1r} + L_2C_2v_{2r} + C_3\,(L_1+L_2)\,(v_{1r}+v_{2r})}{L_1L_2A\,(v_{1r}+v_{2r})}$	$\dfrac{C_2i_{1r}(0) + C_1i_{2r}(0)}{A\,(v_{1r}+v_{2r})}$

$$e_{3t} + L_2 \frac{di_{2t}}{dt} + E = 0, \tag{47}$$

$$L_2 \frac{di_{2t}}{dt} - \frac{1}{C_2} \int_0^t (i_{3t} - i_{2t})\, dt + v_{2t} = 0. \tag{48}$$

Transforming Equations (46), (47), and (48) by use of the Laplace transform,

$$E_{3t}(s) - \frac{1}{C_3 s} I_{3t}(s) - \frac{v_{3t}}{s} = 0, \tag{49}$$

$$E_{3t}(s) + L_2 s I_{2t}(s) - L_2 i_{2t}(0) - \frac{v_{1t}}{s} = 0, \tag{50}$$

$$L_2 s I_{2t}(s) - L_2 i_{2t}(0) - \frac{1}{C_2 s} I_{3t}(s) + \frac{1}{C_2 s} I_{2t}(s) + \frac{v_{2t}}{s} = 0. \tag{51}$$

When the transformed equations are solved simultaneously, the leakage current is found to be

$$I_{2t}(s) = \frac{i_{2t}(0)\ L_2(C_2+C_3)s - v_{2t}(C_2+C_3)}{L_2(C_2+C_3)s^2 + 1}. \tag{52}$$

The corresponding voltage across the leakage inductance during the trace period is

$$E_{2t}(s) = \frac{-L_2[v_{2t}(C_2+C_3)s + i_{2t}(0)]}{L_2(C_2+C_3)s^2 + 1}, \tag{53}$$

and the high voltage across C_3 is

$$E_{3t}(s) = \frac{L_2(C_2+C_3)\,(v_{1t}+v_{2t})\ s^2 + L_2 i_{2t}(0)\ s + v_{1t}}{s\,[L_1(C_2+C_3)\ s^2 + 1]}. \tag{54}$$

Taking the inverse transform of Equation (52) results in the time function for the leakage current;

$$i_{2t}(t) = K_1 \left[\frac{b_0}{\delta} \sin \delta t + \cos \delta t \right], \tag{55}$$

where

$$K_1 = i_{2r}(t_r),$$

$$b_0 = \frac{-v_{2t}}{L_2 I_{2r}(t_r)},$$

$$\delta^2 = \frac{1}{L_2(C_2+C_3)},$$

$$v_{2t} = -e_{2r}(t_r).$$

It is noted that the initial conditions for the trace period are found from the equations for the retrace period evaluated at time equal to t_r. Since Equation (53) for the voltage across the leakage inductance is of the same form as for the current $I_{2t}(s)$, this voltage is also given by Equation (55) with the appropriate constants

$$\begin{aligned} K_1 &= -v_{2t} \\ &= e_{2r}(t_r), \\ b_0 &= \frac{i_{2r}(t_r)}{e_{2r}(t_r)(C_2+C_3)}. \end{aligned} \tag{56}$$

The angular frequency δ remains unchanged. The variation of the high voltage with time is obtained from the inverse transform of Equation (54) which results in

$$e_{3t}(t) = K_2\left[\frac{d_0}{\delta^2} - \frac{d_0-\delta^2}{\delta^2}\cos\delta t + \frac{d_1}{\delta}\sin\delta t\right], \tag{57}$$

with

$$K_2 = v_{1t} + v_{2t},$$

$$\delta^2 = \frac{1}{L_2(C_2+C_3)},$$

$$v_{1t} = -E,$$

$$d_0 = \frac{v_{1t}}{L_2(C_2+C_3)(v_{1t}+v_{2t})},$$

$$d_1 = \frac{i_{2r}(t_r)}{(C_2+C_3)(v_{1t}+v_{2t})},$$

$$v_{2t} = -e_{2r}(t_r).$$

APPENDIX II

Steady-State Solution of Repeating Transient

Determination of the Retrace Time: The conditions on the deflection system are such that the switch S in the equivalent circuit shown in Figure 6 must be closed at the instant when the voltage $e_{1r}(t)$ across L_1 is equal to $-E$. This interval of time between the opening and closing of the switch is the retrace time t_r. For a given set of circuit constants and supply voltage, the time t_r must first be found and then corrected to the desired value by a change in the circuit constants. A convenient means to find the retrace time is by application of Newton's method to Equation (43) for $f(t) = e_{1r}(t)$. This is done by equating $f(t)$ in Equation (43) to $-E$ and solving for the zero of the difference voltage $g(t)$.

$$g(t) = f(t) + E$$

$$= \frac{K}{\beta^2 - \lambda^2}\left[\frac{a_2\beta^2 - a_0}{\beta}\sin\beta t + (\beta^2 - a_1)\cos\beta t + \frac{a_0 - a_2\lambda^2}{\lambda}\sin\lambda t + (a_1 - \lambda^2)\cos\lambda t\right] + E, \tag{58}$$

where the constants are given in the first row of Table I. In Newton's method, a trial value of time t_1 is inserted in Equation (58) and the quantities $g(t_1)$ and $[dg(t)/dt]_{t=t_1}$, or $g'(t_1)$, are determined. The second approximation to t_r is then

$$t_2 = t_1 - \frac{g(t_1)}{g'(t_1)} \tag{59}$$

The process is repeated until t_r is obtained to the desired degree of accuracy.

Initial Conditions: Let it be assumed that the circuit constants from a practical design have been used as a starting point. These constants must be modified to give the desired retrace time and the minimum ringing condition. Any convenient value can be assumed for the current $i_{2r}(0)$ and the voltage v_{2r} to start the solution. The initial yoke current can be approximated by $Et_t/2L_1$ as given by Equation (15).

With these initial conditions, the retrace time t_r is first found. The capacitance C_1 is then changed to obtain the desired retrace time.

At the end of the retrace period, the initial values for the trace period are given by

$$\begin{aligned} i_{1t}(0) &= i_{1r}(t_r), \\ i_{2t}(0) &= i_{2r}(t_r), \\ v_{2t} &= e_{2r}(t_r), \\ v_{1t} &= -E. \end{aligned} \tag{60}$$

Following the various currents and voltages through the trace cycle, the final currents $i_{1t}(t_t)$ and $i_{2t}(t_t)$, and the voltage $e_{2t}(t_t)$ are obtained. The initial conditions for the second deflection cycle are then

$$\begin{aligned} i_{1r}(0)_1 &= \frac{i_{1r}(0) + i_{1t}(t_t)}{2}, \\ i_{2r}(0)_1 &= \frac{i_{2r}(0) + i_{2r}(t_t)}{2}, \\ v_{2r1} &= \frac{v_{2r} - e_{2t}(t_t)}{2}, \\ v_{1r1} &= -E, \end{aligned} \tag{61}$$

where the second set of subscripts is used to denote the second cycle.

The process indicated above is repeated until the final values agree with the initial values to the desired degree of closure. Figure 17 illustrates the convergence of the initial conditions for the voltage v_{2r} and the corresponding current i_{2r} for a given set of circuit constants.

Appendix III

Impedance-Level Change

Let it be assumed that the impedance level of the deflection system is changed by a factor k. This means that all the inductances are multiplied by k and all the capacitances are divided by k. The L_1/C_1 ratio of the yoke circuit is then multiplied by k^2 and the characteristic impedance $\sqrt{L_1/C_1}$ is k times as great. If the voltages remain the same, the currents are divided by the factor k. Using the Equations (40) defining the constants for Equation (43), we have the new constants corresponding to the impedance change k;

$$a_0' = \frac{\frac{1}{k} i_{1r}(0)}{kL_2 \frac{1}{k^2} A\, v_1} = a_0,$$

$$a_1' = \frac{\frac{1}{k} (C_1 v_1 + C_3 v_1 + C_3 v_2)}{kL_2 \frac{1}{k^2} A\, v_1} = a_1,$$

$$a_2' = \frac{\frac{1}{k^2} i_{1r}(0)\ (C_2 + C_3) - \frac{1}{k^2} i_{2r}(0)\ C_3}{\frac{1}{k^2} A\, v_1} = a_2. \qquad (62)$$

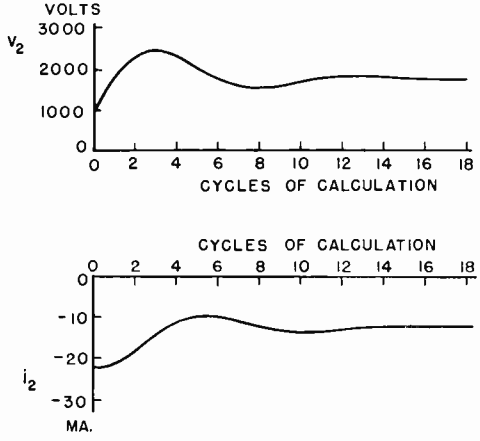

Fig. 17—Convergence of initial conditions.

Similarly, substituting inductances k times as large and capacitances $1/k$ times as large in Equations (41) and (42) shows that the angular frequencies β and λ remain unchanged. It can be shown that the change in impedance level does not affect the other equations for the deflection system. Thus it is evident that if a change in impedance level does not change the equations for the system, a solution at a given impedance level can be scaled for other impedance levels.

Time-Scale Changes

If the time scale is to be changed by a constant factor η, all the inductances and capacitances must be multiplied by the constant η. This operation does not change the characteristic impedance $\sqrt{L_1/C_1}$; however, the angular frequencies β and λ are each divided by the factor η. Substituting inductances and capacitances η times as large in Equations (40), we find the new constants

$$\begin{aligned} a_0' &= a_0/\eta^3, \\ a_1' &= a_1/\eta^2, \\ a_2' &= a_2/\eta. \end{aligned} \tag{63}$$

Using these constants in Equation (43) results in the new function $f'(t)$,

$$\begin{aligned} f'(t) = \frac{K}{\frac{\beta^2}{\eta^2} - \frac{\lambda^2}{\eta^2}} \Bigg[& \frac{\frac{a_2}{\eta}\frac{\beta^2}{\eta^2} - \frac{a_0}{\eta^3}}{\frac{\beta}{\eta}} \sin\frac{\beta}{\eta}t + \left(\frac{\beta^2}{\eta^2}\frac{a_1}{\eta^2}\right)\cos\frac{\beta}{\eta}t \\ & + \frac{\frac{a_0}{\eta^3}\frac{a_2}{\eta} - \frac{\lambda^2}{\eta^2}}{\frac{\lambda}{\eta}} \sin\frac{\lambda}{\eta}t + \left(\frac{a_1}{\eta^2} - \frac{\lambda^2}{\eta^2}\right)\cos\frac{\lambda}{\eta}t \Bigg] \\ = f\left(\frac{t}{\eta}\right), & \end{aligned} \tag{64}$$

which shows that the time scale has been changed by the factor η. Since the horizontal-deflection period of 63.6 microseconds remains fixed, the trace period must change in accord with

$$t_t = 63.6 \times 10^{-6} - t_r. \tag{65}$$

Thus the trace period will decrease as the retrace period increases. For the proper mathematical relations, the total horizontal period must change by the same factor η as does the retrace period t_r. This means that the time scaling of the circuit constants is not exact; experience has shown, however, that the results obtained by this method are close enough for practical purposes.

THE INFLUENCE OF MAGNETIC TAPE ON THE FIELD OF A RECORDING HEAD*

By

E. Della Torre†

Summary—In making accurate measurements of the field of a recording head it is desirable to know the effect of magnetic tape. The method of images is used here to make a first-order correction on the field in the absence of tape. Two assumptions are made in these calculations. First, it is assumed that the tape coating does not affect the magnetization of the head. The validity of this assumption is examined and it does not seem very restrictive. The second assumption is that the tape coating has a constant permeability. A measure of the effect of the tape is introduced in the form of two parameters. These are plotted for various tape thicknesses in the case where the "far" field approximation is valid.

Introduction

THE record and playback performance of a magnetic-tape recording system is influenced by the pattern as well as the strength of the field at the recording gap. In the absence of magnetic tape, the field may be calculated by means of the Schwarz–Christoffel transformation. It is assumed that the permeability of the head material is infinite, i.e., the pole pieces are magnetic equipotentials. Using this method, Weber[1] has given solutions for many configurations and Westmijze[2] has calculated the effect of gap length on the playback characteristic.

Since the permeability of the magnetic oxide coating of the tape is relatively low, this solution is often sufficiently accurate. It is desirable, however, to have a better understanding of the tape's effect upon the field when precise measurements are to be made. The following calculations are a first-order correction for the effect of the tape coating in altering the field about the gap. The case of an infinitely thick tape coating and that of a tape coating of finite thickness are computed separately.

The effect of the coating upon the recording field is computed by

* Manuscript received October 14, 1959.

† Formerly, RCA Laboratories, Princeton, N. J.; now with the Electrical Engineering Department, Rutgers University, New Brunswick, N. J.

[1] E. Weber, *Electromagnetic Fields*, John Wiley and Sons, Inc., New York, 1950, pp. 325-354.

[2] W. K. Westmijze, "Studies on Magnetic Recording," *Philips Research Reports*, Vol. 8, p. 161, June, 1953.

using the method of images. In the case of a coating of finite thickness, there are an infinite number of images. In the region where the approximation is valid, however, the resulting infinite series solution converges rapidly. Since the "far" field over a semi-infinite gap is simple, a complete calculation is made for that case.

The effect of the coating upon the pole pieces shall be assumed, to a first-order approximation, to be so small that the magnetization in them does not change. The field at the coating, on the other hand, will be changed to satisfy the usual boundary conditions, i.e., that the potentials on both sides at the boundary are equal, and that the normal derivatives of the potentials are in the ratio of the permeabilities of the two media.

Method of Images

It has been shown[3] that when a charge distribution is placed in front of a dielectric of relative permittivity ϵ, the field outside the dielectric can be computed by replacing the dielectric with an image distribution. This distribution is located at the mirror image of the original distribution, but the charge density is decreased by the factor $(1 - \epsilon)/(1 + \epsilon)$. The field inside the dielectric is assumed to be $2/(1 + \epsilon)$ times the charge density of the original distribution. The boundary conditions for the magnetic scalar potential are the same as those for the electric potential if ϵ is replaced by the relative permeability, μ. Thus, the method of images is also valid in the treatment of magnetic fields if ϵ is replaced by μ in the image values.

A magnetized material will induce a potential ϕ_m as a function of its magnetization, M, given by[4]

$$\phi_m = \frac{1}{4\pi}\left[\int \frac{M \cdot ds}{r} - \int \frac{\nabla \cdot M}{r}\, dv\right]. \qquad (1)$$

In Equation (1), the divergence of M may be thought of as a magnetic pole, and the normal component of M at the surface as a surface magnetic pole density. Therefore, a given head magnetization will induce in the tape coating an image magnetization that has the geometrical distribution of the mirror image, but the magnitude of the magnetic-pole density will be multiplied by the appropriate factor.

---

[3] A. Somerfeld, *Electrodynamics*, Academic Press, New York, 1952, p. 63.

[4] W. K. H. Panofsky and M. Phillips, *Classical Electricity and Magnetism*, Addison-Wesley Publishing Company, Redding, Mass., 1955, p. 136.

At this point, it is necessary to assume that introduction of the tape coating near the head will not change the magnetization of the head. In other words, no images are induced in the head due to the presence of magnetic poles in the tape. This assumption may be regarded as a first-order approximation. The region of validity may be ascertained by computing the field at the head due to the coating. If this field is appreciable, then this method is no longer valid for the case in which the source has high permeability. In the case in which the head is near saturation, however, the magnetization is only slightly affected by the image poles, and this method is valid. A calculation of the limit of accuracy is given in the next section.

Infinitely Thick Tape Coating

If the thickness of the tape coating is large compared to the dimensions of the gap, it may for all practical purposes be considered infinitely thick. In this case, there is only one set of boundary conditions

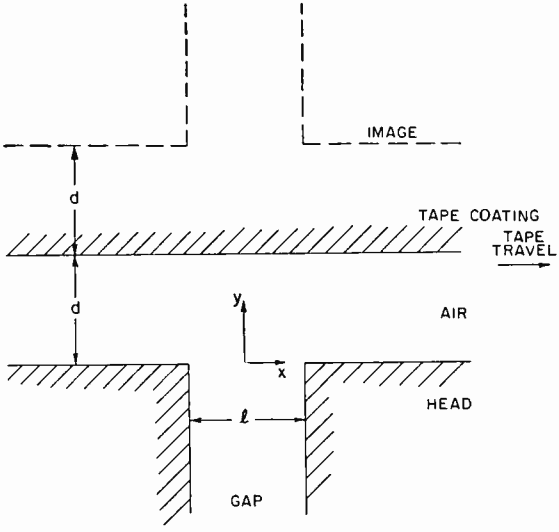

Fig. 1—Infinitely thick tape coating above a recording **gap.**

to be matched, and thus a single magnetic pole will have only one image.

A coordinate system whose origin is at the surface of the head, as shown in Figure 1, is used. By a method such as that discussed by Weber,[1] it is possible to find $\phi_0(x,y)$, the potential in the absence of the tape coating. If the coating is a distance d above the head, then in the region between the head and the tape, the potential due to the

image configuration is given by $[(1-\mu)/(1+\mu)]\,\phi_0\,(2d-x,y)$. Thus, the potential in the presence of the tape is

$$\phi(x,y) = \phi_0(x,y) + \frac{1-\mu}{1+\mu}\phi_0(x, 2d-y). \tag{2}$$

In the particular case where the dimensions of the gap are small compared to the distance to the tape, ϕ_0 can be approximated by

$$\phi_0 = \frac{\Phi}{\pi}\tan^{-1}\frac{x}{y}. \tag{3}$$

According to this function, the right pole face would be at a potential $\Phi/2$, and the left pole face at $-\Phi/2$. In this case, it is possible to calculate the region in which the approximation is valid.

Due to continuity, the magnetic field inside the head is approximately the same as that in the gap. If l is the gap length, this field is Φ/l. Inside the head, the magnetic field due to the tape is strongest at the corners of the gap $(\pm l/2, 0)$. Thus, this is the largest field that need be considered. The condition that the horizontal component of the field is negligible when compared to the field in the head can be expressed by

$$\left(\frac{\mu-1}{\mu+1}\right)\frac{\Phi}{\pi}\frac{2d}{\left(\frac{l}{2}\right)^2+(2d)^2} \ll \frac{\Phi}{l} \tag{4}$$

or

$$\left(\frac{\mu-1}{\mu+1}\right)\frac{2ld}{\pi\left[\left(\frac{l}{2}\right)^2+(2d)^2\right]} \ll 1. \tag{5}$$

In the region in which this condition is valid, l is much smaller than d due to the conditions in Equation (3). Therefore, Equation (5) reduces to

$$\frac{d}{l} \gg \frac{1}{2\pi}\frac{\mu-1}{\mu+1}. \tag{6}$$

For magnetic recording tape, μ is about 4. Thus, d must be large compared to .096 gap length. This head-to-tape spacing is usually exceeded

with high-resolution heads. For this short-gap case, the potential in the region between the tape and the head is given by (from Equations (2) and (3))

$$\phi = \left\{ \frac{\Phi}{\pi} \tan^{-1} \frac{x}{y} + \frac{1-\mu}{1+\mu} \tan^{-1} \frac{x}{2d-y} \right\}, \tag{7}$$

and the potential inside the tape coating is given by

$$\phi = \frac{2\Phi}{(1+\mu)\,\pi} \tan^{-1} \frac{x}{y}. \tag{8}$$

Tape Coating of Finite Thickness

If the tape coating is of finite thickness t, as shown in Figure 2, image reflections occur at two tape surfaces and an infinite number

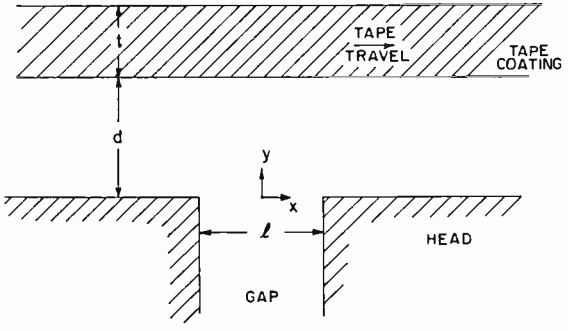

Fig. 2—Tape coating of finite thickness above a recording gap.

of images result for a single pole. In this case the solution cannot be expressed in closed form as above, but is given by an infinite series. The resulting images are located at integral multiple distances of twice the coating thickness, t, above the image configuration discussed previously. The images progressively decrease in magnitude by the factor $(1-\mu)^2/(1+\mu)^2$. In this case, therefore, Equation (2) is replaced by

$$\phi = \phi_0(x,y) + \frac{1-\mu}{1+\mu} \phi_0(x, 2d-y) + \sum_{n=1}^{\infty} \frac{4\mu}{(\mu+1)^2} \left(\frac{\mu-1}{\mu+1} \right)^{2n-1} \phi_0(x, 2d+2nt-y). \tag{9}$$

The right-hand side of Equation (9) consists of three terms: the first is the field in the absence of tape; the second is the correction made previously in the case of the infinitely thick coating; the third term is the new correction. Since, for positive x, $\phi_0(x,y)$ decreases monotonically when y increases, the following inequality holds:

$$\sum_{n=1}^{\infty} \frac{4\mu}{(\mu+1)^2}\left(\frac{\mu-1}{\mu+1}\right)^{2n-1} \phi_0(x, 2d+2nt-y) \leq$$

$$\left(\frac{\mu-1}{\mu+1}\right)\Phi_0(x, 2d-y)\,\frac{4\mu}{(\mu+1)^2}\sum_{n=0}^{\infty}\left(\frac{\mu-1}{\mu+1}\right)^{2n}.$$

By use of the formula for the infinite sum of a geometric series, it is seen that the right-hand term in this inequality is the negative of the second term on the right-hand side of Equation (9). Thus, the solution for thin coating lies between the solution for zero-thickness tape coating (no tape) and infinitely thick tape coating. Due to this fact, the condition for validity previously discussed certainly holds in this case and is much too stringent for thin tape coatings.

The region of interest is in the coating. The potential at the lower surface of the tape is obtained by letting y equal d, since Equation (9) is valid between the head and the tape. The component of the field in the direction of tape motion is obtained by differentiating ϕ with respect to x. In the region in which Equation (3) is valid, the field at the lower surface of the tape is given by

$$H = \frac{2\Phi}{5\pi d}\left\{\frac{1}{1+\left(\frac{x}{d}\right)^2} + \frac{10\mu}{(\mu+1)^2}\sum_{n=1}^{\infty}\left(\frac{\mu-1}{\mu+1}\right)^{2n-1}\frac{1}{\left(1+\frac{2nt}{d}\right)\left[1+\frac{\frac{x}{d}}{1+\frac{2nt}{d}}\right.}\right.$$

(1

CONCLUSION

It should be remembered that Equation (10) is not valid very close to the gap. Otherwise, it is independent of the size of the gap. The horizontal component of the field at the lower surface of the tape is shown in Figure 3 as a function of distance along the tape. Various tape coating thicknesses are plotted assuming that $\mu = 4$. It is noted

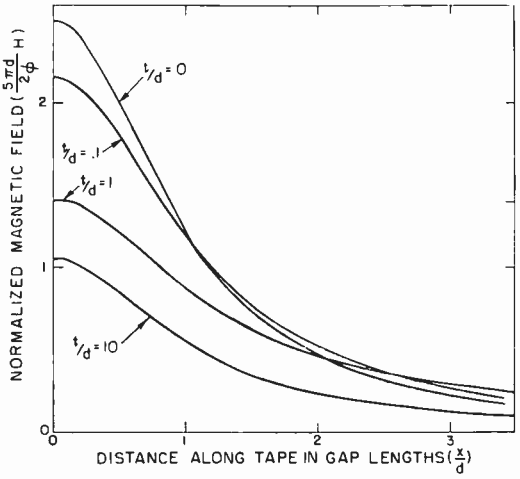

Fig. 3—Variation of field for different thicknesses of tape coating when $\mu = 4$.

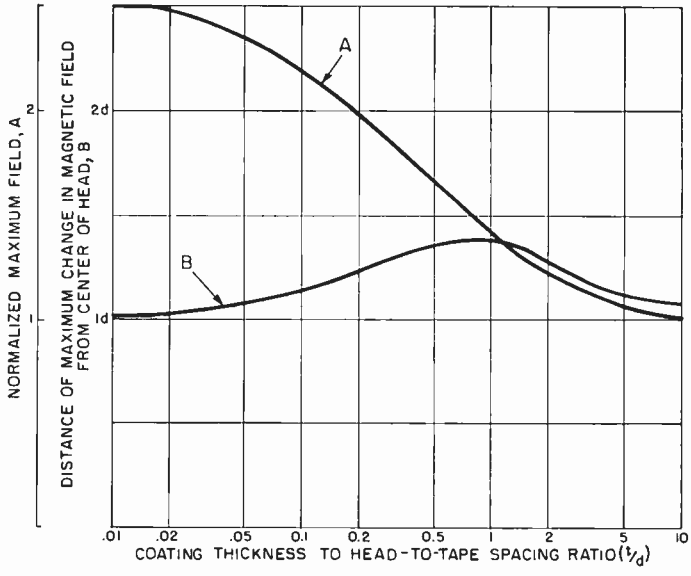

Fig. 4—Effect of tape on the field of a recording head.

that these curves can be approximated by a function of the form

$$H = \frac{2\Phi}{5\pi d} \frac{A}{1 + \left(\frac{x}{B}\right)^2}. \tag{11}$$

The accuracy of such an approximation is within 7 per cent of the maximum field when t/d is 1. This is the poorest case, and much better agreement is obtained for other thicknesses. It is felt, therefore, that A and B give a good measure of the effect of the tape coating. Their variation as a function of coating thickness is shown in Figure 4.

It should be kept in mind that this is the field at the lower surface of the tape. For thin coatings this might be a good approximation to the field inside the coating as well. For thick coatings, however, Equation (8) gives the potential inside the coating.

NONLINEAR THEORY OF A VELOCITY-MODULATED ELECTRON BEAM WITH FINITE DIAMETER*

By

F. Paschke

RCA Laboratories,
Princeton, N.J.

Summary—*In this solution of the nonlinear space-charge-wave equation obtained by third-order successive approximation, the fringe field of the beam is taken into account. The solution consists of space-charge waves with the following plasma-frequency reduction factors:* $p(\omega)$, $3p(\omega)$, $p(2\omega) + p(\omega)$, *and* $p(2\omega) - p(\omega)$ *at the fundamental frequency;* 0, $p(2\omega)$, *and* $2p(\omega)$ *at the second harmonic; and* $p(3\omega)$, $p(\omega)$, $3p(\omega)$, $p(2\omega) + p(\omega)$, *and* $p(2\omega) - p(\omega)$ *at the third harmonic. Here* $p(n\omega)$ *is the well-known small-signal reduction factor of the fundamental radial mode at the frequency* $n\omega$. *The modulation is therefore a periodic function of distance along the beam only if both* $p(\omega)/p(2\omega)$ *and* $p(\omega)/p(3\omega)$ *are rational numbers. For very thin beams, both the second and third harmonics grow with distance. An investigation of the fundamental current (bunching) in a beam enclosed by a perfectly conducting drift tube reveals that, as the driving voltage increases, the optimum bunching position moves from the small-signal value of one-fourth effective plasma wavelength towards the input cavity. A maximum saturation efficiency of* $(2/3)^{3/2} = 54.4$ *per cent is obtained for small bunching distances; a very small minimum occurs at a bunching distance of half the effective plasma-wavelength. The theoretically predicted variation of the fundamental and harmonic currents along the beam agrees very well with experimental results reported by others.*

As a result of this investigation, two high-efficiency devices are proposed. One is a two-cavity klystron with a disc-loaded nonpropagating drift tube. The other is a three-cavity klystron with the second cavity idling and tuned to approximately the second harmonic.

Introduction

THE classical problem in the theory of beam-type microwave tubes is that of velocity modulation. The small-signal analyses are well understood and, at least for strong magnetic focusing fields, have been confirmed by experiments. This is not the case for large signal levels. The early paper of Webster[1] deals with a one-dimensional model and is applicable only for $\omega_p/\omega \ll 1$ where ω is the angular signal frequency and ω_p the plasma frequency. Paschke[2,3] uses the "Eulerian" hydrodynamic approach and solves the resulting

* Manuscript received August, 1959.

[1] D. L. Webster, "Cathode Ray Bunching," *Jour. Appl. Phys.*, Vol. 10, p. 501, July, 1939.

nonlinear space-charge-wave equation by successive approximations. In this model, the effects of fringe fields of the beam are taken into account. In the first paper[2], a solution is given for the one-dimensional case, i.e., for negligible frings fields, but with the space-charge parameter ω_p/ω unrestricted. This solution confirms for $\omega_p/\omega \ll 1$ the results of Webster[1]. It has, however, been demonstrated by Chodorow, Ginzton and Nalos,[4] by Cullen and Stephenson,[5] and by Mihran[6,7] that the one-dimensional theories do not explain their experimental findings. In a two-dimensional theory, German and Kompaneets[8] simplify the analysis by the assumption of a periodic variation of the space-charge density along the beam. Mihran[6] and Paschke[3] demonstrated that this assumption is unrealistic. Webber[9] confirmed the importance of the fringe field by machine computations on the disc-electron model introduced earlier by Tien, Walker, and Wolontis.[10] Aside from the obvious disadvantages inherent in machine computations, the theory based on the disc-electron model does not agree with several experiments.[7] This inadequacy can be blamed on the fact that the beam is replaced by, for example, 16 disc-shaped supercharged particles per r-f cycle, whereas the actual number of electrons per r-f cycle is at least in the millions. The hydrodynamic model is therefore expected to be superior to the disc-electron model.

Recently, Paschke[3] has derived a second-order solution of the hydrodynamic equations given in Reference (2) with the fringe field of the beam taken into account. This analysis predicts the somewhat strange behavior of the second harmonic found experimentally by Mihran[6]. In the present paper, this analysis is carried on to the third order in

---

[2] F. Paschke, "On the Nonlinear Behavior of Electron-Beam Devices," *RCA Review*, Vol. 18, p. 221, June, 1957.

[3] F. Paschke, "Generation of Second Harmonic in a Velocity-Modulated Electron Beam of Finite Diameter," *RCA Review*, Vol. 19, p. 617, December, 1958.

[4] M. Chodorow, E. L. Ginzton, and E. J. Nalos, "Debunching of Electron Beams Constrained by Strong Magnetic Fields," *Proc. I.R.E.*, Vol. 41, p. 999, August, 1953.

[5] A. L. Cullen and I. M. Stephenson, "An Experimental Investigation of Velocity-Modulated Electron Beams," *Proc. I.E.E.*, Vol. 105B, Supplement 12, p. 843, May, 1958.

[6] T. G. Mihran, "Harmonic Current Growth in Velocity-Modulated Electron Beams," *Jour. Appl. Phys.*, Vol. 30, p. 1346, September, 1959.

[7] T. G. Mihran, "The Effect of Space Charge on Bunching in a Two-Cavity Klystron," *Trans. I.R.E., PGED*, Vol. 6, p. 54, January, 1959.

[8] V. I. German and A. S. Kompaneets, "Theory of a Buncher," *Sov. Phys., Techn. Phys.*, Vol. 1, No. 3, p. 654, 1956.

[9] S. E. Webber, "Ballistic Analysis of a Two Cavity Finite Beam Klystron," *Trans. I.R.E., PGED*, Vol. 5, p. 98, April, 1958.

[10] P. K. Tien, L. R. Walker, and V. M. Wolontis, "A Large Signal Theory of Traveling Wave Amplifiers," *Proc. I.R.E.*, Vol. 43, p. 260, March, 1955.

order to predict saturation of the fundamental and excitation of the third harmonic. The results are compared with measurements reported by others, and an investigation is made as to how the efficiency of a two-cavity klystron can be improved.

It is hoped that this contribution will help to dispel the widespread belief that, because of overtaking, the hydrodynamic model must break down at large levels. Overtaking can, in principle, be treated by a multi-velocity hydrodynamic theory. This paper demonstrates, however, that at least for $\omega_p/\omega \ll 1$ the univelocity theory gives an adequate prediction of the behavior of the beam up to saturation level.

Solution of Nonlinear Space-Charge-Wave Equation

The following assumptions underlie the analysis:

(1) The electron flow is confined by an infinitely strong magnetic field.

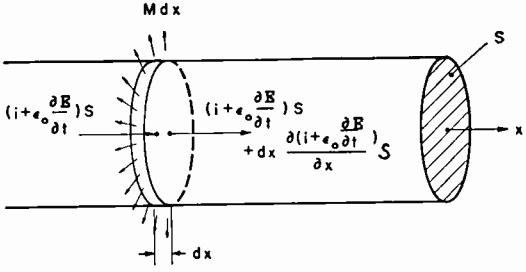

Fig. 1—Current flow through an infinitesimal element of the beam.

(2) The electron and phase velocities are small compared to the velocity of light.

(3) The electric r-f field E in the direction of the stream is approximately constant over the cross section of the beam. This is tantamount to assuming that the transverse electric field varies linearly across the beam.

(4) The effects of the potential depression caused by space charge across the beam and the thermal velocity distribution are negligible.

Figure 1 shows the current flow through an infinitesimal element of the beam; E is the axial electric field strength, i is the convection-current density, and S is the area of the beam cross section. The displacement current per unit length, M, which flows away from the beam accounts for the fringe field. This field is particularly important

in traveling-wave amplifiers, for it establishes the coupling between beam and delay line. According to the continuity equation of Maxwell's field theory, the total current flux into a given volume is zero. Thus for the infinitesimal beam element,

$$\frac{\partial i}{\partial x} + \epsilon_0 \frac{\partial^2 E}{\partial x \partial t} + \frac{M}{S} = 0. \tag{1}$$

As a variable, the displacement, a scalar quantity defined by

$$y = \epsilon_0 E + m, \tag{2}$$

is used, where m represents the fringe field, and is given by

$$\frac{\partial^2 m}{\partial x\, \partial t} = \frac{M}{S}. \tag{3}$$

The fields are approximated by first-, second-, and third-order perturbations which are denoted by the subscripts 1 to 3. The subscript 0 refers to steady-state quantities. The perturbations satisfy the following system of equations (taken from Reference (2)).*

$$\frac{\partial^2 y_1}{\partial x^2} + \frac{2}{v_0} \frac{\partial^2 y_1}{\partial x\, \partial t} + \frac{1}{v_0^2} \frac{\partial^2 y_1}{\partial t^2} + \beta_p^2 (y_1 - m_1) = 0, \tag{4a}$$

$$\frac{\partial^2 y_2}{\partial x^2} + \frac{2}{v_0} \frac{\partial^2 y_2}{\partial x\, \partial t} + \frac{1}{v_0^2} \frac{\partial^2 y_2}{\partial t^2} + \beta_p^2 (y_2 - m_2)$$

$$+ \frac{2}{i_0 v_0} \left(\frac{\partial y_1}{\partial x} \frac{\partial^2 y_1}{\partial t^2} - \frac{\partial y_1}{\partial t} \frac{\partial^2 y_1}{\partial x \partial t} \right) + \frac{2}{i_0} \left(\frac{\partial y_1}{\partial x} \frac{\partial^2 y_1}{\partial x \partial t} - \frac{\partial y_1}{\partial t} \frac{\partial^2 y_1}{\partial x^2} \right)$$

$$+ \frac{3\eta}{\epsilon_0 v_0^2} \frac{\partial y_1}{\partial x} (y_1 - m_1) = 0, \tag{4b}$$

$$\frac{\partial^2 y_3}{\partial x^2} + \frac{2}{v_0} \frac{\partial^2 y_3}{\partial x \partial t} + \frac{1}{v_0^2} \frac{\partial^2 y_3}{\partial t^2} + \beta_p^2 (y_3 - m_3)$$

$$+ \frac{2}{i_0 v_0} \left(\frac{\partial y_1}{\partial x} \frac{\partial^2 y_2}{\partial t^2} + \frac{\partial y_2}{\partial x} \frac{\partial^2 y_1}{\partial t^2} - \frac{\partial y_2}{\partial t} \frac{\partial^2 y_1}{\partial x \partial t} - \frac{\partial y_1}{\partial t} \frac{\partial^2 y_2}{\partial x \partial t} \right)$$

* The term with the factor m_2 in Equation (4c) was erroneously omitted in Reference (2).

$$+\frac{2}{i_0}\left(\frac{\partial y_1}{\partial x}\frac{\partial^2 y_2}{\partial x \partial t}+\frac{\partial y_2}{\partial x}\frac{\partial^2 y_1}{\partial x \partial t}-\frac{\partial y_1}{\partial t}\frac{\partial^2 y_2}{\partial x^2}-\frac{\partial y_2}{\partial t}\frac{\partial^2 y_1}{\partial x^2}\right)$$

$$+\frac{1}{i_0^2}\left[\frac{\partial^2 y_1}{\partial x^2}\left(\frac{\partial y_1}{\partial t}\right)^2-2\frac{\partial y_1}{\partial t}\frac{\partial y_1}{\partial x}\frac{\partial^2 y_1}{\partial x \partial t}+\frac{\partial^2 y_1}{\partial t^2}\left(\frac{\partial y_1}{\partial x}\right)^2\right]$$

$$+\frac{3\eta}{\epsilon_0 v_0^2}\left(\frac{\partial y_2}{\partial x}(y_1-m_1)+\frac{\partial y_1}{\partial x}(y_2-m_2)\right)$$

$$+\frac{3\eta}{\epsilon_0 v_0 i_0}(y_1-m_1)\left(\frac{\partial y_1}{\partial x}\right)^2=0. \tag{4c}$$

The velocities are given by

$$-\rho_0 v_1=\frac{\partial y_1}{\partial t}+v_0\frac{\partial y_1}{\partial x}, \tag{5a}$$

$$-\rho_0 v_2=\frac{\partial y_2}{\partial t}+v_0\frac{\partial y_2}{\partial x}+v_1\frac{\partial y_1}{\partial x}, \tag{5b}$$

$$-\rho_0 v_3=\frac{\partial y_3}{\partial t}+v_0\frac{\partial y_3}{\partial x}+v_2\frac{\partial y_1}{\partial x}+v_1\frac{\partial y_2}{\partial x}, \tag{5c}$$

and the current densities by

$$i_n=-\frac{\partial y_n}{\partial t}. \tag{6}$$

β_p is the plasma-wave number of the infinitely extended beam and ρ_0 the d-c space-charge density. Equation (4a) determines the first-order term of the fundamental frequency. Equation (4b) determines the second-harmonic content of the beam. All third-order quantities can be split into two terms:

$$\left.\begin{aligned} y_3&=y_{31}+y_{33},\\ m_3&=m_{31}+m_{33},\end{aligned}\right\} \tag{7}$$

and so forth. The index 31 designates third-order terms of the fundamental frequency. These terms lead to the prediction of saturation. The index 33 designates third-order terms of the third-harmonic frequency.

Thus far the analysis is applicable for all O-type devices. In the following, solutions will be sought for a velocity-modulated beam inside of a drift tube. To determine the fringe-field terms m_1, m_2, and m_3, one can make use of the fact that the solutions of the homogeneous parts of the linear differential Equations (4) must yield the well-known Hahn–Ramo waves. If it is assumed that the fundamental radial mode, the mode with the largest effective plasma frequency, is predominant, so that all higher-order modes are negligible,

$$\left.\begin{aligned} y_1 - m_1 &= p^2\,(\omega)\; y_1, \\ y_2 - m_2 &= p^2\,(2\omega)\; y_2, \\ y_{31} - m_{31} &= p^2\,(\omega)\; y_{31}, \\ y_{33} - m_{33} &= p^2\,(3\omega)\; y_{33}. \end{aligned}\right\} \tag{8}$$

Here $p(n\omega)$ is the plasma-frequency reduction factor of the fundamental mode at the n^{th} harmonic frequency. By this procedure it seems to be possible to obtain valid solutions for all geometries. However, caution must be exercised in the application of this analysis to cases where the field distribution across the beam is *not* approximately constant, contradictory to one of the basic assumptions made earlier. Thus, for a gap-excited klystron, a close quantitative agreement of this theory with experiments is expected only for values of the normalized beam radius $\beta_e b = \omega b/v_0 < 1$. This disadvantage is shared with the theories using the disc-electron model.[9,10] It is believed that the present analysis yields results which are in *qualitative* agreement with measurements on gap-excited klystrons even for $\beta_e b > 1$. For grid-modulated tubes the theory is expected to agree quantitatively with experiments over a wider range of beam radii.

It is convenient to introduce the following two parameters:

$$\xi = p(\omega)/p(2\omega), \tag{9}$$

$$\sigma = p(\omega)/p(3\omega). \tag{10}$$

These parameters were evaluated from the curves for $p(\omega)$ given in the literature[11,12] for a pencil beam of radius b inside of a perfectly conducting cylinder (drift tube) of radius a. The results are shown

[11] G. M. Branch and T. G. Mihran, "Plasma Frequency Reduction Factors in Electron Beams," *Trans. I.R.E., PGED*, Vol. 2, p. 3, April, 1955.

[12] W. Kleen, *Einführung in die Mikrowellen-Elektronik*, S. Hirzel Verlag, Stuttgart, 1952, p. 104.

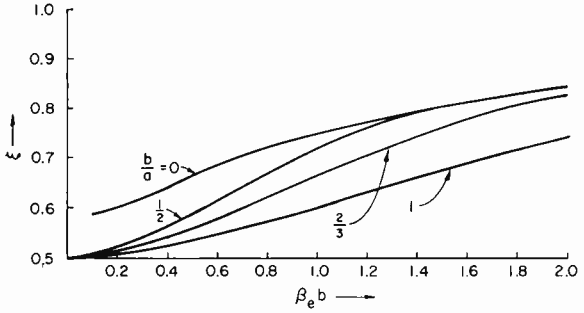

Fig. 2—$\xi = p(\omega)/p(2\omega)$ versus normalized beam radius with the ratio of beam-to-drift tube radius as parameter.

in Figures 2 and 3. For an infinitely broad beam, $\xi = 1$ and $\sigma = 1$. For extremely thin beams, $\xi \to 1/2$ and $\sigma \to 1/3$, unless $a = \infty$.

It is assumed that the beam is modulated at $x = 0$ by a double layer with the small voltage $V_1 \sin \omega t$. If the further assumption is made that

$$\omega_p/\omega \ll 1, \tag{11}$$

one can neglect the excitation of harmonic velocities by the double layer.[2] Then the velocity modulation produced by the double layer at $x = 0$ is $(\eta V_1/v_0) \sin \omega t$. The solution of Equations (4) through (6) for this excitation follows. In these equations,

$$\alpha = p(\omega)\ \beta_p x, \tag{12}$$

and the index $n\omega$ refers to the components of the n^{th} harmonic.

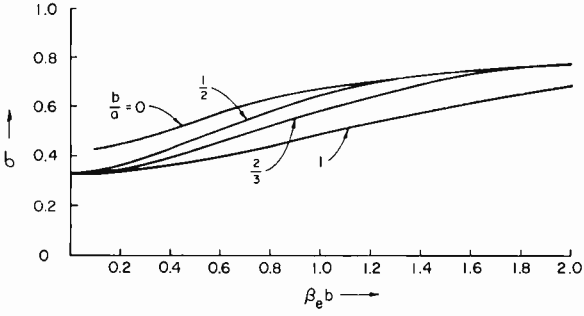

Fig. 3—$\sigma = p(\omega)/p(3\omega)$ versus normalized beam radius with the ratio of beam radius to drift-tube radius as parameter.

Fundamental Current

$$\frac{i_\omega}{i_0} = \frac{2\omega}{\omega_p\, p(\omega)}\,\frac{V_1}{4V_0}\cos(\omega t-\beta_e x)\left\{\sin\alpha-\left(\frac{\omega}{\omega_p\, p(\omega)}\,\frac{V_1}{4V_0}\right)^2\left[\frac{7\xi^2-1}{4(4\xi^2-1)}\sin^3\alpha\right.\right.$$
$$+\frac{(1-\xi^2)(2\xi^2+2\xi-1)}{(2\xi+1)(4\xi^2-1)}\left(\xi^2\sin\alpha\left(\frac{1}{\xi}+1\right)-\xi(1+\xi)\sin\alpha\right)$$
$$+\frac{(1-\xi^2)(-2\xi^2+2\xi+1)}{(2\xi-1)(4\xi^2-1)}\left(-\xi^2\sin\alpha\left(\frac{1}{\xi}-1\right)+\xi(1-\xi)\sin\alpha\right)$$
$$\left.\left.+\frac{(1-\xi^2)(8\xi^2+1)}{4(4\xi^2-1)}\left(-\alpha\cos\alpha+\sin\alpha\right)\right]\right\}, \qquad (13)$$

Fundamental Velocity

$$\frac{v_\omega}{v_0} = 2\,\frac{V_1}{4V_0}\sin(\omega t-\beta_e x)\left\{\cos\alpha-\left(\frac{\omega}{\omega_p\, p(\omega)}\,\frac{V_1}{4V_0}\right)^2\right.$$
$$\left[\frac{29\xi^2+1}{16(4\xi^2-1)}\left(\cos\alpha-\cos 3\alpha\right)\right.$$
$$+\frac{(1-\xi^2)(1-2\xi-2\xi^2)(1+\xi)\xi}{(2\xi+1)(4\xi^2-1)}\left(-\cos\alpha\left(\frac{1}{\xi}+1\right)+\cos\alpha\right)$$
$$+\frac{(1-\xi^2)(1+2\xi-2\xi^2)(1-\xi)\xi}{(2\xi-1)(4\xi^2-1)}\left(-\cos\alpha\left(\frac{1}{\xi}-1\right)+\cos\alpha\right)$$
$$+\frac{(1-\xi^2)(8\xi^2+1)}{4(4\xi^2-1)}\alpha\sin\alpha+\frac{\xi(1-\xi^2)}{4\xi^2-1}\left(\cos\alpha\left(\frac{1}{\xi}+1\right)-\cos\alpha\left(\frac{1}{\xi}-1\right)\right.$$
$$-\xi^2\cos\alpha+\frac{3\xi^2}{2(4\xi^2-1)}\left(\cos\alpha+\cos 3\alpha\right)$$
$$\left.\left.-\frac{2\xi^2(1-\xi^2)}{4\xi^2-1}\left(\cos\alpha\left(\frac{1}{\xi}+1\right)+\cos\alpha\left(\frac{1}{\xi}-1\right)\right)\right]\right\}, \qquad (14)$$

Second-Harmonic Current

$$\frac{i_{2\omega}}{i_0} = 2\left(\frac{\omega}{\omega_p\, p(\omega)}\,\frac{V_1}{4V_0}\right)^2\xi^2\left[1-\frac{3}{4\xi^2-1}\cos 2\alpha\right.$$
$$\left.+\frac{4(1-\xi^2)}{4\xi^2-1}\cos\frac{\alpha}{\xi}\right]\cos 2(\omega t-\beta_e x), \qquad (15)$$

Second-Harmonic Velocity

$$\frac{v_{2\omega}}{v_0} = \frac{\omega}{\omega_p p(\omega)} \left(\frac{V_1}{4V_0} \right)^2 \left[\frac{2\xi^2 + 1}{4\xi^2 - 1} \sin 2\alpha - \frac{4\xi(1-\xi^2)}{4\xi^2 - 1} \sin \frac{\alpha}{\xi} \right] \sin 2(\omega t - \beta_e x), \tag{16}$$

Third-Harmonic Current

$$\begin{aligned} \frac{i_{3\omega}}{i_0} = 6 \left(\frac{\omega}{\omega_p p(\omega)} \frac{V_1}{4V_0} \right)^3 \Bigg[& \frac{3(5\xi^2+1)}{2(4\xi^2-1)\left(9 - \frac{1}{\sigma^2}\right)} \left(3\sigma \sin \frac{\alpha}{\sigma} - \sin 3\alpha \right) \\ & + \frac{(1-\xi^2)(8\xi^2+1)}{2(4\xi^2-1)\left(\frac{1}{\sigma^2} - 1\right)} \left(\sin \alpha - \sigma \sin \frac{\alpha}{\sigma} \right) \\ & + \frac{(1-\xi^2)(1+6\xi+2\xi^2)}{(4\xi^2-1)\left((1+\xi)^2 - \frac{1}{\sigma^2}\right)} \left(\xi^2 \sin \alpha \left(\frac{1}{\xi} + 1 \right) - \xi(1+\xi)\,\sigma \sin \frac{\alpha}{\sigma} \right) \\ & + \frac{(1-\xi^2)(-1+6\xi-2\xi^2)}{(4\xi^2-1)\left((1-\xi)^2 - \frac{1}{\sigma^2}\right)} \left(\xi^2 \sin \alpha \left(\frac{1}{\xi} - 1 \right) - \xi(1-\xi)\,\sigma \sin \frac{\alpha}{\sigma} \right) \Bigg] \cos 3(\omega t - \beta_e x). \end{aligned} \tag{17}$$

Third-Harmonic Velocity

$$\begin{aligned} \frac{v_{3\omega}}{v_0} = \left(\frac{\omega}{\omega_p p(\omega)} \right)^2 \left(\frac{V_1}{4V_0} \right)^3 \Bigg[& \frac{(1-\xi^2)(8\xi^2+1)}{(4\xi^2-1)\left(\frac{1}{\sigma^2} - 1\right)} \left(\cos \alpha - \cos \frac{\alpha}{\sigma} \right) \\ & - \frac{9(5\xi^2+1)}{(4\xi^2-1)\left(9 - \frac{1}{\sigma^2}\right)} \left(\cos 3\alpha - \cos \frac{\alpha}{\sigma} \right) \end{aligned}$$

$$+\frac{2(1-\xi^2)(1+6\xi+2\xi^2)\left(\frac{1}{\xi}+1\right)}{(4\xi^2-1)\left(\left(\frac{1}{\xi}+1\right)^2-\frac{1}{\sigma^2}\right)}\left(\cos\alpha\left(\frac{1}{\xi}+1\right)-\cos\frac{\alpha}{\sigma}\right)$$

$$+\frac{2(1-\xi^2)(-1+6\xi-2\xi^2)\left(\frac{1}{\xi}-1\right)}{(4\xi^2-1)\left(\left(\frac{1}{\xi}-1\right)^2-\frac{1}{\sigma^2}\right)}\left(\cos\alpha\left(\frac{1}{\xi}-1\right)-\cos\frac{\alpha}{\sigma}\right)$$

$$-\frac{2\xi^2+1}{2(4\xi^2-1)}(\cos\alpha-\cos 3\alpha)+\frac{2\xi(1-\xi^2)}{4\xi^2-1}$$

$$\left(\cos\alpha\left(\frac{1}{\xi}-1\right)-\cos\alpha\left(\frac{1}{\xi}+1\right)\right)$$

$$-2\xi^2\cos\alpha+\frac{3\xi^2}{4\xi^2-1}\left(\cos\alpha+\cos 3\alpha\right)$$

$$-\frac{4\xi^2(1-\xi^2)}{4\xi^2-1}\left(\cos\alpha\left(\frac{1}{\xi}+1\right)+\cos\alpha\left(\frac{1}{\xi}-1\right)\right)\Bigg]\sin 3(\omega t-\beta_e x). \tag{18}$$

From these solutions and from the definitions (9), (10), and (12), it is seen that there are plasma waves with the following plasma-frequency reduction factors: $p(\omega)$, $3p(\omega)$, $p(2\omega)+p(\omega)$, and $p(2\omega)-p(\omega)$ at the fundamental frequency; 0, $p(2\omega)$, and $2p(\omega)$ at the second harmonic; and $p(3\omega)$, $p(\omega)$, $3p(\omega)$, $p(2\omega)+p(\omega)$, and $p(2\omega)-p(\omega)$ at the third harmonic. Additional waves would be obtained if one extended the theory to higher than third-order harmonics. The fundamental modulation predicted by the above equations is a non-periodic function of distance. The second-harmonic modulation is periodic only if ξ is a rational number. The third harmonic modulation is periodic only if both ξ and σ are rational numbers. Moreover, even if ξ and σ are rational numbers, the pattern is rather complex because it is composed of at least two sine functions with different wavelengths so that in most practical cases the period is relatively large. The case of very small beam diameter must be excepted from these considerations, because $\xi\to\frac{1}{2}$ and $\sigma\to\frac{1}{3}$ (unless $a=\infty$) and the inhomogeneous part of Equation (4b) as well as Equation (4c) contains terms which are solutions of the corresponding homogeneous differential equation. Thus there are resonant solutions. From Equations (13) to (18) one finds, for $\xi\to\frac{1}{2}$ and $\sigma\to\frac{1}{3}$,

$$\frac{i_\omega}{i_0} = \frac{2\omega}{\omega_p p(\omega)} \frac{V_1}{4V_0} \left\{ \sin\alpha - \left(\frac{\omega}{\omega_p p(\omega)} \frac{V_1}{4V_0} \right)^2 \left[\frac{33}{256} \sin\alpha + \frac{1}{256} \sin 3\alpha \right.\right.$$
$$\left.\left. - \frac{3}{32} \alpha \cos\alpha - \frac{3}{64} \alpha \cos 3\alpha + \frac{9}{32} \alpha^2 \sin\alpha \right] \right\} \cos(\omega t - \beta_e x), \tag{19}$$

$$\frac{v_\omega}{v_0} = 2 \frac{V_1}{4V_0} \left\{ \cos\alpha - \frac{3}{32} \left(\frac{\omega}{\omega_p p(\omega)} \frac{V_1}{4V_0} \right)^2 \left[\frac{7}{24} (\cos 3\alpha - \cos\alpha) \right.\right.$$
$$\left.\left. - \alpha \sin\alpha + \frac{3}{2} \alpha \sin 3\alpha + 3\alpha^2 \cos\alpha \right] \right\} \sin(\omega t - \beta_e x), \tag{20}$$

$$\frac{i_{2\omega}}{i_0} = \frac{1}{2} \left(\frac{\omega}{\omega_p p(\omega)} \frac{V_1}{4V_0} \right)^2 [1 - \cos 2\alpha + 3\alpha \sin 2\alpha] \cos 2(\omega t - \beta_e x), \tag{21}$$

$$\frac{v_{2\omega}}{v_0} = \frac{1}{4} \frac{\omega}{\omega_p p(\omega)} \left(\frac{V_1}{4V_0} \right)^2 [\sin 2\alpha + 6\alpha \cos 2\alpha] \sin 2(\omega t - \beta_e x), \tag{22}$$

$$\frac{i_{3\omega}}{i_0} = \frac{3}{16} \left(\frac{\omega}{\omega_p p(\omega)} \frac{V_1}{4V_0} \right)^3 \left[9\alpha^2 \sin 3\alpha - 5\alpha \cos 3\alpha + \frac{9}{2} \alpha \cos\alpha \right.$$
$$\left. - \frac{5}{24} \sin 3\alpha + \frac{9}{8} \sin\alpha \right] \cos 3(\omega t - \beta_e x), \tag{23}$$

$$\frac{v_{3\omega}}{v_0} = \frac{3}{16} \left(\frac{\omega}{\omega_p p(\omega)} \right)^2 \left(\frac{V_1}{4V_0} \right)^3 \left[9\alpha^2 \cos 3\alpha + 3\alpha \sin 3\alpha \right.$$
$$\left. - \frac{3}{2} \alpha \sin\alpha + \frac{1}{8} (\cos 3\alpha - \cos\alpha) \right] \sin 3(\omega t - \beta_e x). \tag{24}$$

Thus, for very thin beams, the harmonics grow with distance. This has been interpreted as parametric oscillation[3] with the fundamental acting as pump frequency. It should be noted, however, that the modulation by a double layer does not require power and that the real kinetic power flow in the beam is zero. Therefore, the harmonic power which can be coupled out derives, as is well known for klystrons, from the d-c power of the beam and not from the pumping source.

The growth predicted by Equations (21) through (24) is linear for the second harmonic and quadratic for the third harmonic. However, terms of higher than third order which have been neglected in the present analysis have amplitudes of higher than square power in distance. Thus, the solutions are valid only relatively close to the exciting cavity.

Even for $\xi \doteq 1/2$ and $\sigma \doteq 1/3$ there are third-order resonant solutions for the fundamental frequency. These terms do not lead to a real growth of the fundamental modulation, however, because, for values of α and V_1/V_0 where the successive approximation is applicable, they are small compared to the sinusoidal first-order terms.

For $\xi = 1$ and $\sigma = 1$ the results of the one-dimensional theory[2] are recovered.

Discussion of Convection-Current Distribution (Bunching)

Figures 4 to 6 show how the fundamental and harmonic convection

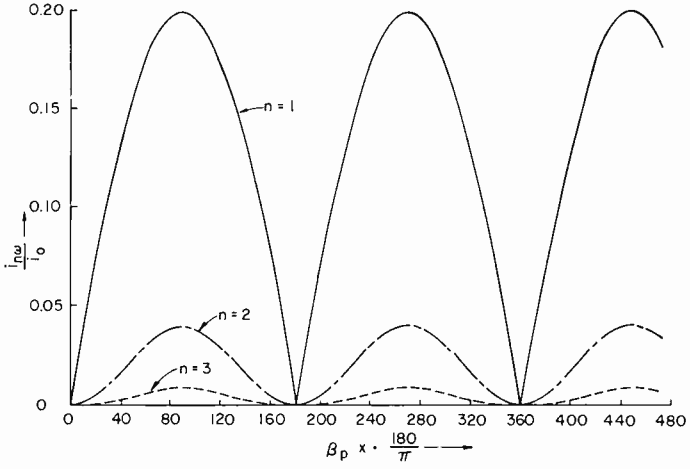

Fig. 4—Convection current of the n^{th} harmonic versus distance from the input cavity measured in plasma-phase angle. The beam is assumed to be infinitely broad ($\xi = 1$, $\sigma = 1$, one-dimensional case). The normalized input voltage A defined by Equation (25) is 0.1.

currents vary along the beam if the normalized input voltage

$$A = \frac{V_1}{4V_0} \frac{\omega}{\omega_p p(\omega)} \tag{25}$$

has the relatively small value of 0.1. In Figure 4, the familiar pattern of the one-dimensional theory ($\xi = 1$, $\sigma = 1$) is shown. However, from Figures 2 and 3 it is seen that for any practical beam both ξ and σ deviate considerably from unity. Figure 5 depicts the current variation for the practical values $\beta_e b \doteq 1.2$ and $b/a = 2/3$, which correspond to $\xi \doteq 0.707$ and $\sigma \doteq 0.64$. The harmonic growth predicted for thin beams ($\xi \doteq 1/2$, $\sigma \doteq 1/3$) is shown in Figure 6. Note that the funda-

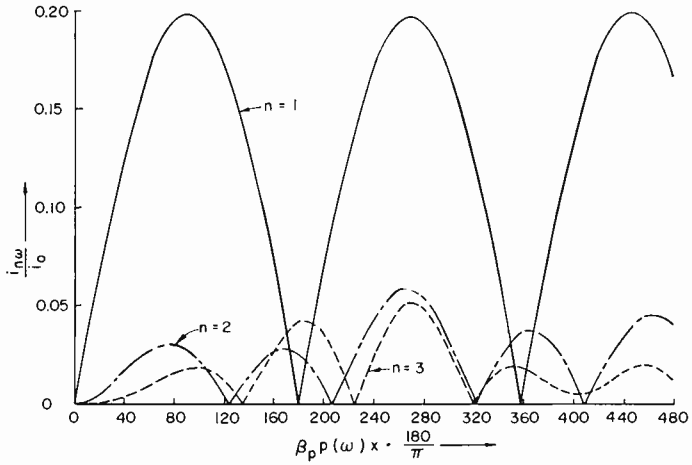

Fig. 5—Convection current of the n^{th} harmonic versus distance from the input cavity measured in plasma-phase angle. $\beta_e b = 1.2$, and $b/a = 2/3$, which corresponds to $\xi = 0.707$, and $\sigma = 0.64$. The normalized input voltage A defined by Equation (25) is 0.1.

mental peaks decay. This is emphasized in Figure 7 where $i_\omega/2i_0\ A$ is plotted versus distance for various values of the normalized input voltage A. The validity of the third peak of the lowest curve ($A^2 = 0.05$) is somewhat in doubt because it corresponds to a level beyond saturation where the third-order theory must break down.

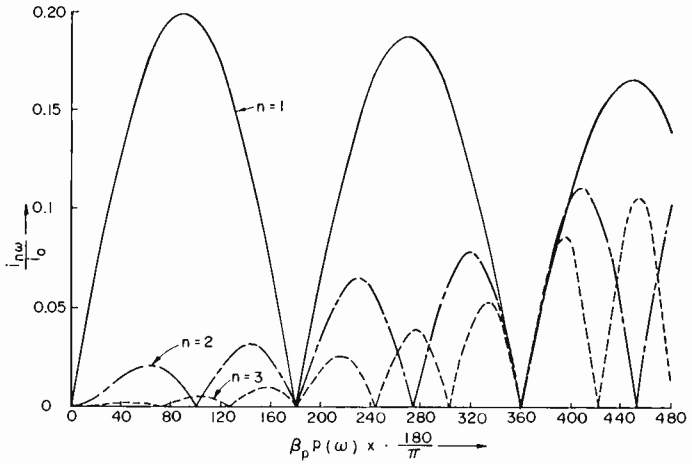

Fig. 6—Convection current of the n^{th} harmonic versus distance from the input cavity measured in plasma-phase angle. The beam is assumed to be very thin ($\xi = 1/2$, $\sigma = 1/3$). The normalized input voltage A defined by Equation (25) is 0.1.

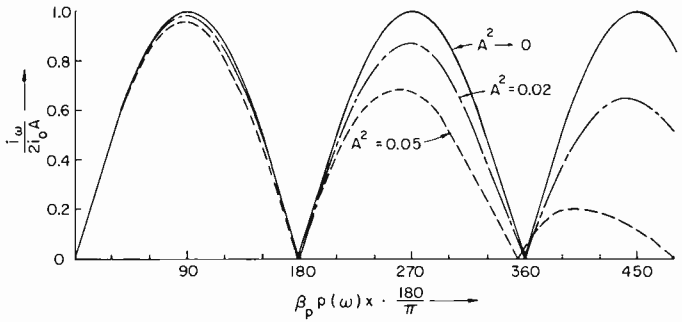

Fig. 7—Fundamental convection current versus distance from the input cavity measured in plasma-phase angle for very thin beams ($\xi \doteq \frac{1}{2}$) and various values of the normalized input voltage A defined by Equation (25).

Experimental results of Mihran[6] agree at least qualitatively with the results shown in Figures 5 and 6.

In Figure 8, the fundamental convection current is plotted versus distance for $\xi = 1/\sqrt{2}$ and the various values of the normalized input voltage, A, measured in decibels. The zero point was arbitrarily chosen to correspond to the relatively low level of $A^2 = 0.008$. At low levels

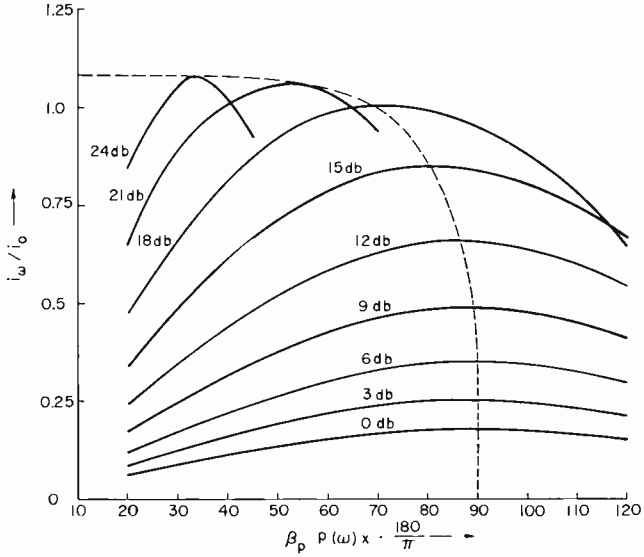

Fig. 8—Fundamental convection current versus distance from the input cavity measured in plasma phase angle for $\beta_e b \doteq 1.2$ and $b/a = \frac{2}{3}$, which corresponds to $\xi \doteq 0.707$ and $\sigma \doteq 0.64$. The parameter is the normalized input voltage A from Equation (25), measured in decibels. Zero decibels corresponds to $A^2 = 0.008$.

the current exhibits a maximum at a plasma phase angle of 90 degrees, as is well known. With increasing driving voltage, however, the maximum shifts towards the input cavity along the dotted curve in Figure 8. This behavior is confirmed by experimental results of Cullen and Stephenson,[5] and particularly by the results of Mihran (Figure 8, Reference (7)). Note that the analysis of the disc-electron model,[9] in contrast to the present theory, predicts a hump in the dashed curve representing the maximum current points which could not be observed experimentally.[7] The theoretical curve of optimum plasma-phase angle versus relative input power can be made to coincide with the experimental data taken from Figure 8 of Reference (7) if the zero-decibel level of the relative input power is chosen so as to obtain best agreement. A quantitative comparison could not be made because no data concerning the absolute value of the input power were given in Reference (7).

The envelope of the curves shown in Figure 8 represents the saturation current. One can write, from Equations (13) and (25),

$$\frac{i_\omega}{i_0} = 2A\ (\sin\alpha - A^2 f(\alpha)). \tag{26}$$

Here $f(\alpha)$ is the term in the square brackets of Equation (13). The current exhibits a maximum (saturation) at an input voltage given by

$$A^2_{\text{sat}} = \frac{\sin\alpha}{3f(\alpha)}. \tag{27}$$

Thus the saturation current is

$$\frac{i_{\omega\text{sat}}}{i_0} = \left(\frac{2}{3}\right)^{3/2} \left(\frac{2\sin^3\alpha}{f(\alpha)}\right)^{1/2}. \tag{28}$$

Maximum output power is achieved if the Q of the output cavity is adjusted so that the gap voltage is maximized without reflection of electrons. Thus the optimum peak voltage in the output gap is to a good approximation equal to the d-c voltage V_0, and the saturation efficiency is

$$\eta_{\text{sat}} = \frac{i_{\omega\text{sat}}\, V_0}{2\, i_0\, V_0} = \left(\frac{2}{3}\right)^{3/2} \left(\frac{\sin^3\alpha}{2f(\alpha)}\right)^{1/2}. \tag{29}$$

This function is plotted in Figure 9 for various values of ξ. For $\alpha \to 0$, the saturation efficiency approaches $(2/3)^{3/2} \doteq 54.4$ per cent. From

Equations (13) and (27), $A^2_{sat} \rightarrow \infty$ for $\alpha \rightarrow 0$. Thus, for extremely small values of α, the saturation efficiency cannot be calculated by a third-order theory. However, for any small values of α which are of practical interest, the third-order approximation does suffice. From Equations (27), (28) and (13), both the driving voltage required for saturation of the current and the saturation current at $\alpha = \pi$ is zero. There are at least four reasons why this result cannot be expected to agree with experiments. First, a third-order theory is not sufficient to predict saturation at values of α where the linear terms vanish. Second, the present analysis is based on the assumption of predominance of the fundamental space-charge mode. This assumption is unrealistic at values of α where the fundamental mode has a zero, because

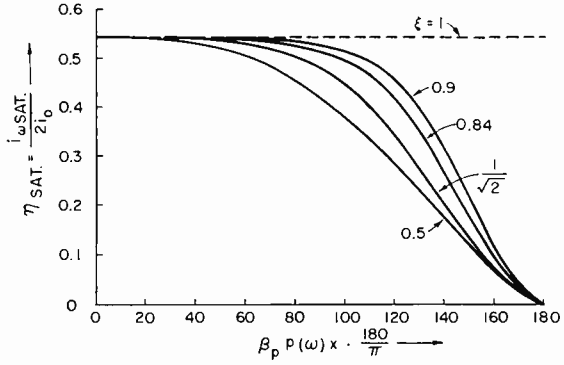

Fig. 9—Saturation efficiency (or fundamental saturation current) versus distance from the input cavity measured in plasma-phase angle for various values of the parameter $\xi = p(\omega)/p(2\omega)$.

in practice higher order modes are to a certain degree excited. Third, practical bunching cavities are not ideal double layers. Fourth, higher-order space-charge terms ignored in this analysis, Expression (11), may lead to a finite current at $\alpha = \pi$. In spite of these limitations, one can expect a very small minimum in saturation current to exist close to $\alpha = \pi$. This is confirmed by the experimental results of Chodorow, Ginzton, and Nalos,[4] Cullen and Stephenson,[5] and Mihran.[7] Chodorow et al also found the modulation close to $\alpha = \pi$ to be dominated by a higher-order radial mode. The measured curves of saturation current versus plasma phase angle in References (4), (5), and (7) show the same shape as the theoretical curves in Figure 9. A detailed comparison of the present analysis with experiments is made possible by the numerous and accurate data of Mihran.[7]

From Figure 9, optimum efficiency appears at $\alpha = 0$, but infinite driving voltage would be required for saturation. Thus, there must be an "optimum" value of α where the efficiency is still high but where

the input voltage required to saturate is at a reasonable level. This optimum plasma phase angle ("peel-off angle") has been defined by Mihran[7] as the angle where the saturation current is 0.5 decibel below its optimum value. The peel-off angle has been evaluated from Figures (2) and (9) for various geometries. The result is plotted in Figure 10 and compared with the experimental points from Reference (7). The value of b/a in the experimental setup was somewhere between zero and 1/2. Thus the agreement is very good for $\beta_e b < 1$. For $\beta_e b > 1$, some discrepancies are to be expected because in this case the axial r-f field in a gap-modulated beam is not approximately constant across

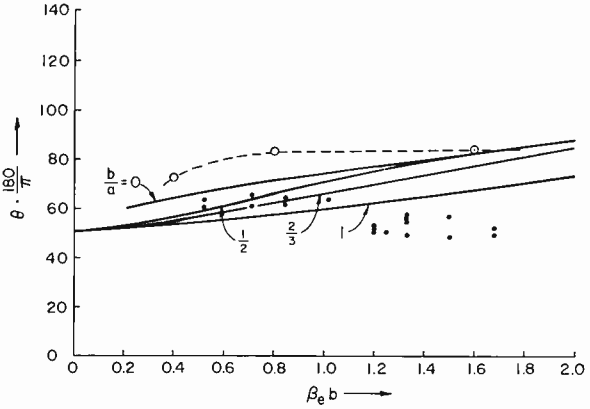

Fig. 10—Peel-off angle θ versus normalized beam radius for various ratios of beam radius to drift-tube radius. The peel-off angle is defined as the plasma-phase angle where the saturation current is 0.5 decibel below its optimum value. The dots are experimental points from Reference (7). The three circled points, also taken from Reference (7), result from the analysis of the disc-electron model (Reference (9)).

the beam, contradictory to one of the basic assumptions. The theoretical points derived from the disc electron model (taken from Reference (7)) are in poor agreement with the experimental results even at small $\beta_e b$. Note that the peel-off angle θ is a very critical quantity to compare with measurements because a small change in the slope of the curves in Figure 9 produces a large change in θ. With this in mind, the theory can be regarded as quite satisfactory even for $\beta_e b > 1$.

Improving the Efficiency of Klystrons

The nature of the curves shown in Figure 9 immediately suggests an investigation of cases where $\xi > 1$. From Equation (13) one finds for $\xi > 1$ values of α where the third-order fundamental terms is zero or in phase with the linear term so that the theory is unable to predict

saturation. Presumably the fifth-order term, which is not given in this analysis, would lead to saturation. Nevertheless, it is fair to say that the saturation efficiency of a klystron can be improved over the value $(2/3)^{3/2}$ by boundary conditions such that $\xi > 1$.

To understand this physically, the saturation process must be considered. Saturation can be explained in the following manner. *The fundamental modulation first produces a second harmonic via the second-order nonlinearity of the beam. This second harmonic beats with the fundamental; this produces a third harmonic plus a fundamental term. This third-order fundamental term usually is opposite in phase to the linear term and is therefore at least partly*‡ *responsible for the saturation.* From these considerations, it is clear that the second-harmonic modulation plays an important role in the saturation process. It should be recalled that the only force acting on the electrons is that due to the axial electric field. Due to the strong magnetic focusing field, the effective mass of the electrons in radial direction is so large that the particles are unaffected by the radial electric field. For a given space-charge distribution, the partition of the displacement current into radial and axial components is determined by the boundary conditions. The radial displacement current is (from Equation (8)) proportional to $(1 - p^2)$. It follows that the radial displacement current of the second harmonic is comparatively smaller than the fundamental for $\xi < 1$, while for $\xi > 1$ it is comparatively larger. Consequently, for $\xi < 1$ there is a larger second-harmonic force (axial-displacement current) acting on the electrons than for $\xi > 1$. Thus the magnitude of the saturation term is smaller for $\xi > 1$ than for $\xi < 1$. The saturation level must, therefore, be higher for $\xi > 1$ than for $\xi < 1$.

This explanation is oversimplified, of course, and at least a fifth-order analysis must be carried out for a quantitative prediction of saturation efficiency in the case of $\xi > 1$. For a beam inside of a perfectly conducting cylinder, it was found that $\xi < 1$. This is well understood since the second harmonic bunches are closer spaced axially than the fundamental bunches and less field leaks to the wall. This is not necessarily so for a boundary more complicated than a perfectly conducting, smooth cylinder. The planar model shown in Figure 11 can be used as an example. A ribbon beam, infinitely extended in the y-direction, fills the space between two vane-type structures. The fields are assumed to be independent of y. The vanes are infinitely thin and closely spaced to that they can be replaced by a wall with a surface impedance

‡ Another saturation term is produced by the first-order fundamental modulation via the third-order nonlinearity of the beam.

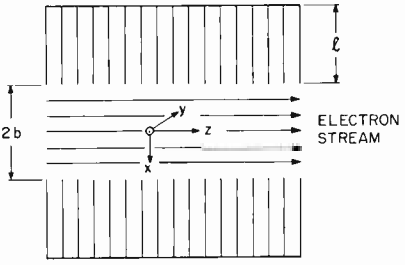

Fig. 11—An infinitely broad ribbon beam with a thickness 2b fills the space between two vane type structures. l is the length of the vanes which are assumed to be infinitely thin and closely spaced.

$$Z = -\frac{E_x}{H_y} = j\sqrt{\frac{\mu_0}{\epsilon_0}}\tan\frac{2\pi l}{\lambda}. \tag{30}$$

The linearized space-charge-wave equation has been solved with the boundary conditions (30) at $x = \pm b$. For an electron velocity of 1000 volts, and $l/b = 37.8$, the plasma-frequency reduction factor follows the pattern shown in Figure 12. The curves labelled with $Z = 0$ or $Z = \infty$ correspond to the cases of frequency-independent zero or infinite wall impedance, respectively. Due to the frequency dependence of the wall impedance (Equation (30)), the reduction factor of the fundamental space-charge wave is close to the curve for $Z = 0$ at low

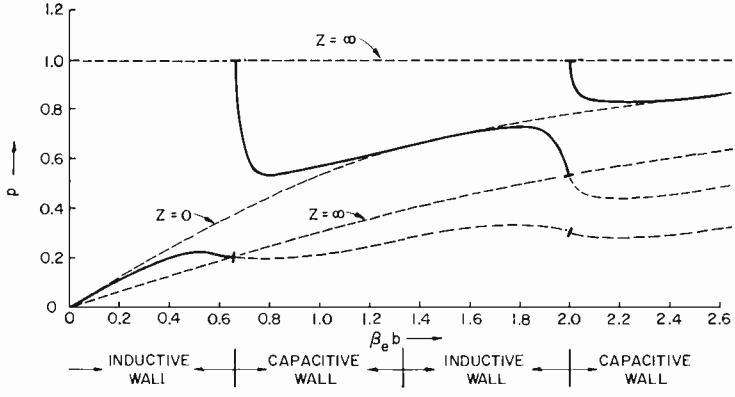

Fig. 12—Plasma-frequency reduction factor of the ribbon beam shown in Figure 11 versus frequency (normalized beam radius) for $l/b = 37.8$ and an electron velocity of 1000 volts. The solid curve corresponds to the reduction factor of the fundamental space-charge wave. The curves labeled with $Z = 0$ and $Z = \infty$ correspond to beams with zero electric field (short circuit) and zero magnetic field (open circuit) at the boundary.

frequencies (small $\beta_e b$), but shifts towards the lower open-circuit curve as $\beta_e b$ increases. At the resonance of the vanes, i.e., when $l = \lambda/4$, the plasma-frequency reduction factor of the fundamental mode jumps to $p = 1$, again approaches the curve for $Z = 0$ as $\beta_e b$ increases, and crosses it for $l = \lambda/2$. Other discontinuities of the reduction factor appear at higher-order resonances of the vane structure. At resonance, the curve of any space-charge mode smoothly joins that of the next higher-order mode. In Figure 13, the parameter ξ of the fundamental mode is plotted versus $\beta_e b$. There are two rather

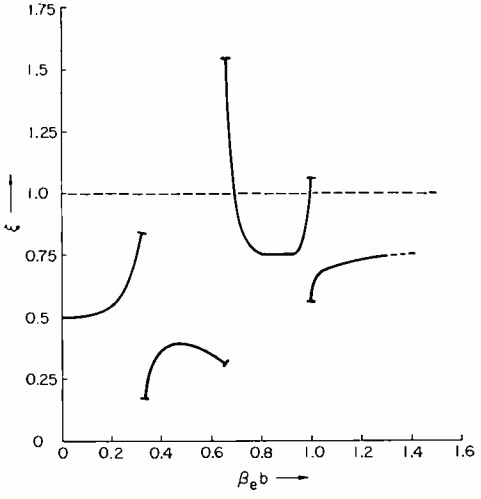

Fig. 13—$\xi = p(\omega)/p(2\omega)$ for the fundamental space-charge wave from Figure 12.

narow ranges where $\xi > 1$, but only the larger range around $\beta_e b \doteq 0.67$ is of practical interest. In the region of an inductive wall impedance where the vane structure is propagating, there can be a growing wave due to traveling-wave-type interaction. In the interesting range around $\beta_e b \doteq 0.67$ where $\xi > 1$, however, the wall impedance is capacitive for the fundamental frequency. For the second harmonic, the wall impedance is inductive, but the inductance is so small that no appreciable growth can occur. Note that this high-efficiency scheme is nothing but a traveling-wave tube operating in the cutoff region of the structure.

The considerable reduction of the plasma frequency caused by a large inductive wall impedance (Figure 12) indicates strong coupling of the space-charge wave to the structure, as is necessary to obtain

practical traveling-wave-type gains. Associated problems are discussed in Reference (13).

Another device having improved efficiency, which has been proposed before by Feenberg,[14] is depicted in Figure 14. Between the two main cavities at a normalized distance α_0 from the input cavity, there is a third cavity which is tuned to *approximately* the second harmonic frequency. When unloaded, this "idling cavity" has a negligible immediate effect on the fundamental modulation but presents an appreciable

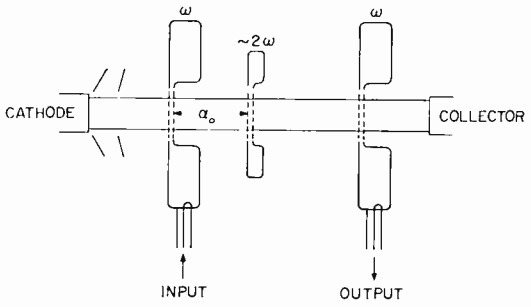

Fig. 14—Three-cavity klystron with an "idling" cavity tuned to approximately the second harmonic. α_0 is the distance between idling and input cavity measured in plasma phase angle.

reactance X to the second harmonic. Thus the second-harmonic current at $\alpha = \alpha_0$ produces an additional second-harmonic velocity modulation which has a 90-degree phase shift towards the exciting second-harmonic current. The additional velocity modulation is transformed into a relatively strong current modulation which, by beating with the fundamental, leads to a term which has a strong influence on the saturation process. A pertinent analysis has been carried out for the resonant case, $\xi = 1/2$. For $\alpha \leq \alpha_0$, Equation (19) is a valid solution for the fundamental convection current. For $\alpha \geq \alpha_0$, however, the following expression must be added to the term in the square bracket of Equation (19):

$$f_{add}(\alpha) = \frac{X\omega I_0}{128\omega_p p(\omega) V_0} [1 - \cos 2\alpha_0 + 3\alpha_0 \sin 2\alpha_0]$$
$$[-\cos(3\alpha - 2\alpha_0) + 12(\alpha - \alpha_0)\sin(\alpha - 2\alpha_0)$$
$$+ \cos\alpha_0 \cos(\alpha - \alpha_0) - 7\sin\alpha_0 \sin(\alpha - \alpha_0)]. \quad (31)$$

[13] F. Paschke, "Die Wechselseitigkeit der Kopplung in Wanderfeldröhren," *Arch. d. elektr. Übertrag.*, Vol. 11, p. 137, April, 1957.

[14] E. Feenberg, "Ultrahigh-Frequency Electron Discharge Apparatus," U.S. Patent 2,579,480, December, 1951.

Here I_0 is the d-c current. The factor in the first bracket is proportional to the second harmonic current at $\alpha = \alpha_0$. The factor in the second bracket describes the transformation of the second harmonic velocity modulation into a fundamental current modulation caused by the idling cavity. The reactance is limited to a value at which no electrons are reflected by the field in the idling cavity. This is expressed by the condition

$$\frac{XI_0}{2V_0}(1 - \cos 2\alpha_0 + 3\alpha_0 \sin 2\alpha_0) < \frac{1}{A^2}. \tag{32}$$

There are values of α where the third-order term of the current vanishes so that no saturation is predicted and the third-order analysis breaks down. It is a fair prediction, however, that the efficiency can be improved over the value $(2/3)^{3/2}$ by introducing the idling cavity. In both schemes, that of the non-propagating periodic structure and that of the idling cavity, experimental work is required to confirm or disprove the predicted improvement in efficiency.

A FREQUENCY-LOCKED GRID-CONTROLLED MAGNETRON*

BY

C. LOUIS CUCCIA

RCA Electron Tube Division,
Harrison, N. J.

Summary—An 800-megacycle magnetron is described which uses a cathode–grid structure in which a standing wave is set up around the cathode close to the source of emission to introduce a frequency-locking signal into the electron cloud. An experimental magnetron has been locked in frequency over a range exceeding 10 megacycles. The output power of this magnetron can be modulated from virtually zero power to several hundred watts without attendant frequency modulation.

INTRODUCTION

THE cavity magnetron came into widespread use during World War II because it was particularly suited for the generation of large amounts of power in the form of pulses as required by radar. It was efficient in such operation, and small in size. In radar, the only modulation required is pulse modulation of the output signal.

Following World War II, numerous applications arose for a microwave oscillator which could be amplitude modulated for communication systems. Despite its small size and high efficiency, the magnetron was unsuitable for these applications because of the frequency modulation which was attendant with amplitude modulation, and because of the difficulty in modulating the magnetron output without producing actual loss of power output in regions of low current where the magnetron breaks into oscillation.

Many methods have been devised to permit amplitude and frequency modulation of the magnetron. These methods include the use of electron couplers,[1] spiral-electron-beam absorption tubes,[2] servo-control circuits, injection locking in the output circuitry of the magnetron,[3,4] and a locking signal applied to electrodes positioned in the

* Manuscript received January 8, 1960.

[1] C. L. Cuccia, "Spiral Beam Tube Modulates 1-KW at UHF," *Electronics*, Vol. 26, p. 130, April, 1953.

[2] J. S. Donal, Jr., and R. R. Bush, "A Spiral Beam Method for the Amplitude Modulation of Magnetrons," *Proc. I.R.E.*, Vol. 37, p. 375, April, 1949.

[3] L. L. Koros, "Frequency Control of Modulated Magnetrons by Resonant Injection System," *RCA Review*, Vol. XIII, p. 47, March, 1952.

[4] J. S. Donal, Jr., and K. K. N. Chang, "An Analysis of the Injection Locking of Magnetrons Used in Amplitude-Modulated Transmitters," *RCA Review*, Vol. XIII, p. 239, June, 1952.

magnetron adjacent to the vane tips.[5] Among the difficulties encountered with all these methods were low efficiency, complexity of equipment, limited range of amplitude or frequency modulation, and failure to meet frequency distortion requirements.

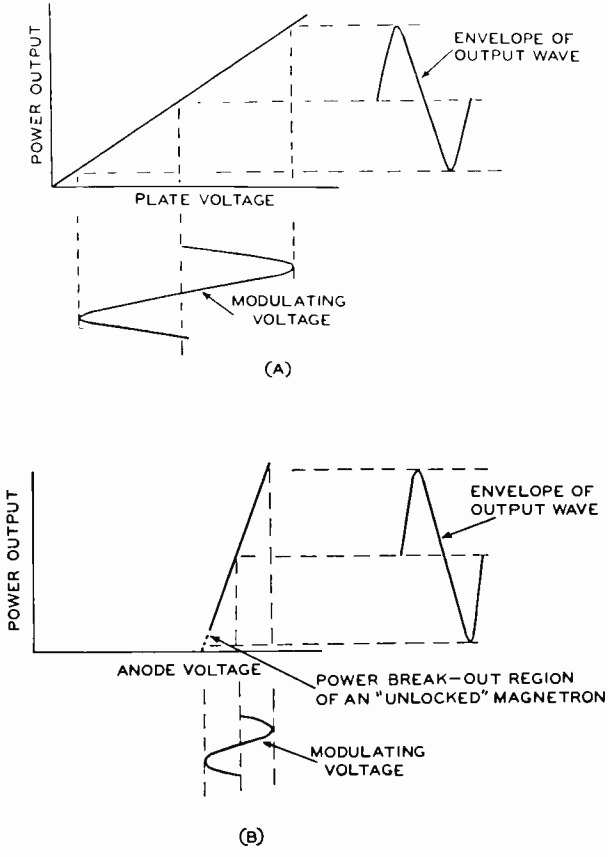

Fig. 1—Characteristic curves relating output power to modulating voltage for both conventional tube oscillators and magnetrons.

The potential attractiveness of the magnetron as a controlled-output-power device has never diminished, however, because of its inherent advantages: (1) the magnetron operates with very high efficiencies at low anode–cathode potentials and at very high current levels

[5] P. L. Spencer, "Grid Magnetron Delivers Modulated UHF Output," *Electronics*, Vol. 26, p. 148, May, 1953.

generated in a relatively small interaction space, and (2) while conventional high-power triode or tetrode oscillators or output stages require modulating voltages swinging between the maximum plate voltage and virtually zero as shown in Figure 1(a), the magnetron requires a modulating voltage having a magnitude no greater than the difference between the magnetron cutoff voltage and the maximum anode voltage, as shown in Figure 1(b). This aspect is important for amplitude-modulated systems used in communication systems because such systems require an output-voltage swing of at least 85 per cent or a power swing from maximum power down to only a few per cent of maximum.

Of the many methods employed for frequency control of a magnetron, the most promising is that of injection locking. In this system, a locking signal injected into the oscillator circuit at a proper point locks the free-running oscillations to its frequency and phase. Utilizing this principle, L. L. Koros[3] has injected a crystal-controlled locking signal into the output circuit of an anode-modulated magnetron and successfully produced an output signal representation of a high-definition television signal. One problem encountered, however, was the design of a circuit capable of providing proper isolation between the magnetron and the locking-signal source.

The frequency-locked grid-controlled magnetron described here is a unique crossed-field device which utilizes the basic magnetron oscillator structure without sacrificing its high efficiency, but which introduces the locking signal at the source of the electrons in a manner whereby satisfactory control of magnetron oscillation is obtained. The structures used to introduce the locking signal provide for complete isolation between the magnetron output circuit and the locking-signal circuit. Experimental tubes of this type have provided frequency-locked outputs from virtually zero output power to almost a kilowatt in the 800-megacycle frequency range and have achieved locking bandwidths in excess of 10 megacycles.

Basic Structure

In the normal magnetron structure, as shown in Figure 2(a), the cathode emits a space-charge cloud. Under the influence of the radial d-c electric field, the axial magnetic field, and the traveling electric field $E_{\theta 1}$ of the anode resonator, this space-charge cloud develops "spokes" which interact with $E_{\theta 1}$ and provide energy to the anode resonator.

In the basic frequency-locked grid-controlled magnetron structure,[6,7] the cathode is replaced by a periodic structure which acts both as a cathode and as a traveling-wave device which supports an electric field traveling at the proper angular velocity around the cathode in the area where the space-charge-cloud characteristic of the magnetron is formed, as shown in Figure 2(b). The configuration is so designed that the traveling electric field of the anode, $E_{\theta 1}$, does not extend too close to the cathode. Due to the injection-lock signal, a second independent traveling electric field, $E_{\theta 2}$, is developed close to the cathode as shown. On their way to the anode, the electrons encounter $E_{\theta 2}$ first and then $E_{\theta 1}$.

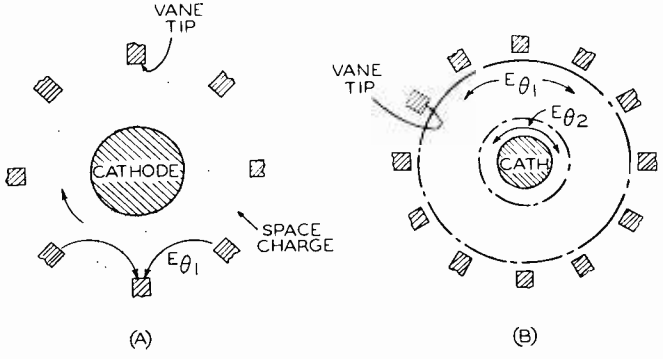

Fig. 2—(A) Space-charge configuration in a magnetron, and (B) traveling azimuthal wave developed in a frequency-locked grid-controlled magnetron.

This traveling electric field $E_{\theta 2}$ was induced in the experimental tubes through the use of a structure, similar to that shown in Figure 3, consisting of an array of small-diameter cathodes arranged in a circle having a peripheral diameter corresponding to the diameter of a normal cathode for the particular anode resonator. Interleaved with these cathodes are grid rods having the same peripheral diameter as the cathodes. The cathodes are all at the same potential, as are the grid rods. A locking voltage, having the frequency required to provide an electric field traveling around the cathode at the angular velocity of the traveling electric field supported (developed) by the

---

[6] C. L. Cuccia and J. T. Wallmark, "A Frequency-Locked Grid-Controlled Magnetron for Amplitude and Frequency Modulation," *PGED I.R.E.*, October, 1955.

[7] E. E. David, Jr., "Locking Phenomena in Microwave Oscillators," *MIT Technical Report*, No. 63, April, 1948.

vane tips of the anode resonator, is developed between the cathode array and the grid array.

When the traveling electric field $E_{\theta 2}$ is introduced into the subsynchronous electron swarm which is formed adjacent to the cathode array, the electrons in this swarm will interact with this traveling electric field at the outset of their trajectories. In this region, the electrons have relatively low velocity and even a traveling electric field of relatively small amplitude will have considerable effect on them. Every electron in this swarm encounters an electric field traveling

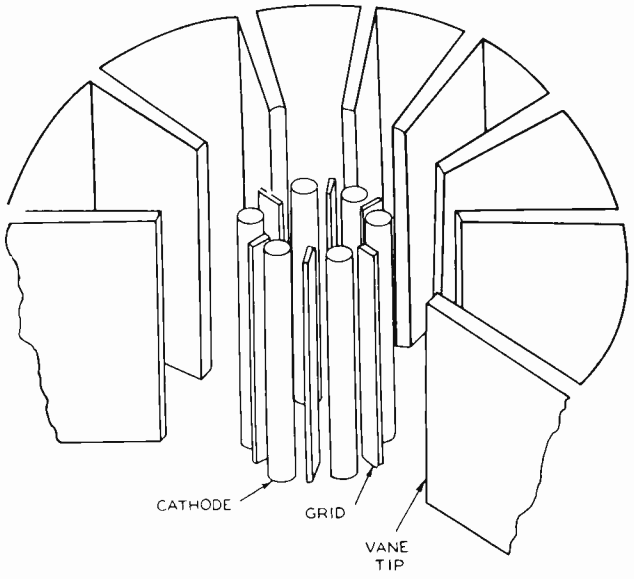

Fig. 3—Grid and cathode configuration in a grid-controlled magnetron.

azimuthally, and the radial velocity of each electron will be dependent upon the phase of the field that it encounters.

These electrons, varying in radial velocity, will enter the electron spokes. The electrons whose radial velocity has increased will reach the tips of the spokes faster than the electrons of decreased radial velocity, and striations of space-charge density will move azimuthally through the tips of the spokes at the angular velocity of the traveling wave at the cathode and induce a locking current in the anode.[8,9] If

---

[8] John C. Slater, *Microwave Electronics*, New York, 1950.

[9] J. S. Donal, Jr., R. R. Bush, C. L. Cuccia, and H. R. Hegbar, "A 1-Kilowatt Frequency-Modulated Magnetron for 900 Megacycles," *Proc. I.R.E.*, Vol. 35, p. 664, July, 1947.

the density variation is at a slightly different angular velocity from the angular velocity of the spokes and if it induces a current of sufficient magnitude in the anode resonator, the equilibrium condition of oscillation of the magnetron will change so that the angular velocity of the spokes will coincide with the angular velocity of the density striations produced by the locking traveling wave injected in the cathode. The magnetron oscillations, therefore, will lock to the frequency of the locking signal.

Figure 4 shows two basic structures for developing the traveling electric field along a cathode–grid array. In the structure shown in

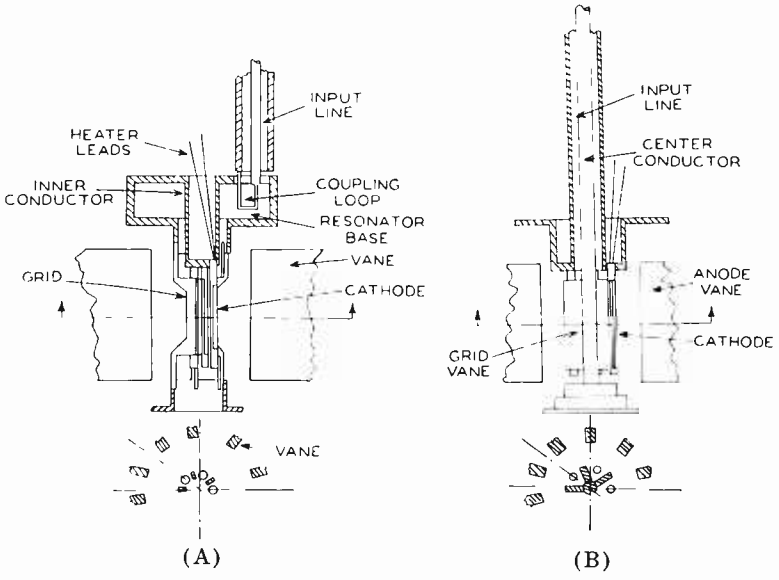

Fig. 4—(A) Cross section of resonator type of grid–cathode arrangement and (B) cross section of coaxial-line type of grid–cathode arrangement.

Figure 4(a), the technique of incorporating the grid and cathode array into a resonant line circuit is used. A structure of cathodes forms the end of the center conductor of a quarter-wave coaxial-line resonator. The grids are components of the outer conductor and are shaped to interleaf with the cathodes to form a coplanar array. A coupling loop is used to introduce the locking signal into the coaxial-line resonator. Two advantages of the use of a loop-driven resonator-type of structure are (1) its ability to develop traveling electric fields of relatively large magnitude with minimum excitation energy, and (2) the absence of a direct connection between the cathode–grid structure and the coupling loop.

Figure 4(b) shows an alternate structure in which the cathode–grid array is incorporated directly into a transmission line. The cathodes are supported by a fixture incorporated into the outer conductor of the transmission line, and the center conductor includes an array of conducting vanes which emanate from the center conductor to interleaf with the cathodes and form a coplanar structure of cathodes and grids. Many other structures are possible, including structures in which both cathodes and grids emit.

Both the structures shown in Figure 4 illustrate an orientation of the grid–cathode structure relative to the anode vanes which provides minimum electromagnetic coupling between the anode and the grid–cathode structure. The orientation of the grid–cathode structure is such that a radial plane passing through a grid or cathode passes halfway between two adjacent vane tips. When each grid or cathode faces a vane tip, maximum coupling is provided between the anode and the cathode–grid structure. Minimum transfer of power from the magnetron output circuit back to the locking signal source requires, however, the structural arrangement shown in Figure 4.

Experimental Grid-Controlled Magnetrons

A high power CW UHF magnetron anode which had been exhaustively tested and which had provided extensive test data with a normal cathode[10] was used in the tests of the grid-controlled magnetrons. This magnetron anode was mechanically tunable from 650 to 890 megacycles and provided CW power output of more than 1 kilowatt with efficiencies of the order of 50 to 60 per cent and with a frequency pushing of 3 megacycles. This anode, shown in Figure 5, had 12 cavities and employed a cathode ⅝ inch in diameter supported in an interaction space (defined by the vane tips) 1⅛ inch in diameter and 2 inches long. It was designed to provide an output power of 1 kilowatt at an anode–cathode potential of approximately 1800 volts with 1 ampere flowing through the anode. The high CW power output was made possible by the use of copper vanes ⅛ inch thick and water-cooling channels installed as an integral portion of the tube envelope. Other physical details and operating characteristics of the magnetron anode, using a standard type cathode, have been described in the literature.[9]

A demountable header technique is employed to facilitate the testing of a wide variety of cathode–grid structures. As shown in Figure 5, a tool-steel ring is incorporated into one end of the magnetron anode, and the grid–cathode assemblies are mounted on a matching tool-steel header. The header and anode rings have a ring of holes in common,

and one gold wire is installed inside and another outside the ring of holes when the header ring is screwed to the anode ring to produce a vacuum-tight seal. This technique was very successful; only one leak was experienced during the experimental program, and headers could be changed within a few hours.

The grid–cathode structures employed during the experimental program are of the loop-driven coaxial-line type shown in Figure 4(a). The grid–cathode resonators are resonant at a single fixed frequency, but the tunability of the anode makes experimental locking tests rapid and easy to control.

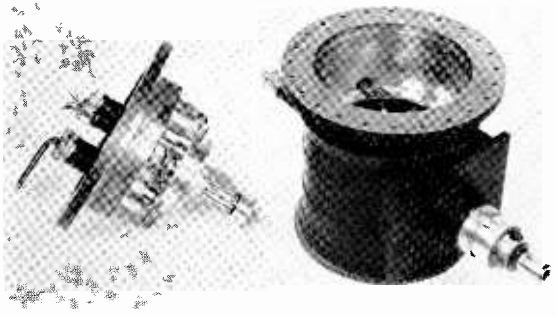

Fig. 5—Photograph of magnetron showing header arrangement which includes a zero-bias grid–cathode structure.

Two types of resonant grid–cathode structures were employed and tested during the program—a zero-bias grid structure and a negative-bias grid structure. The former utilizes a grid array at zero bias relative to the cathode array. It is mechanically simple to construct and provides frequency locking with a range greater than the magnetron pushing. In the negative-bias grid structure, the grids operate at a substantial negative potential relative to the cathode.[5] This structure provides an enhanced locking range for very wideband modulation.

Zero-Bias Grid-Controlled Magnetron

The header shown in the photograph in Figure 5 includes a grid–cathode resonator which is resonant at 780 megacycles. The resonator includes six cathodes, each ⅛ inch in diameter, and six grid rods interleaved to form a coplanar grid–cathode structure. The resonator is mounted on ceramic bushings on the header, and an insulated channel

provides access from the outside of the tube to a water chamber in the resonator. The input transmission line and the coupling loop, as shown in Figure 4(a), do not come into actual physical contact with the resonator, and are at the magnetron anode potential.

Figure 6 is a photograph of the components of the grid–cathode resonator showing the six cathodes forming the end of the center conductor of the resonator, and the cage of grid rods which form the outer conductor of the resonator. Except for the cathodes, the resonator structure, including the water chamber is made of copper. The water chamber surrounds the base of the resonator and affords excellent cooling to this portion of the tube. Each cathode has its own filament, and the header includes connectors for operating these filaments in parallel.

Fig. 6—Photograph of grid and cathode structure disassembled showing cathode cluster and grid arrangement.

When no locking power is applied, the operation of the grid-controlled magnetron is very similar to that of the magnetron having a conventional cathode. The same general relationships among voltage, current, and magnetic field are encountered, and the normal very high magnetron efficiency is maintained.

In one area, however, the nonexcited grid-controlled magnetron presents unique starting characteristics. The space-charge swarm produced by the cathodes includes electrons having a multiplicity of velocities, and this multi-velocity electron motion produces noise which excites the resonant cathode–grid structure. The noise-excitation of the cathode–grid structure then perturbs the space charge in the vicinity of the structure; this causes a delay in the start of oscillation

until a value of current is reached which is higher than that associated with a normal cathode.

The inner diameter of the magnetron anode was 1⅛ inches. In accordance with the Slater criterion[8], the twelve cavities required a cathode diameter of 0.625 inch. A series of grid–cathode structures of different over-all diameters were built and tested for starting current. Figure 7 is a plot of curves showing starting current as a function of both the over-all grid–cathode diameter and the magnetic field.

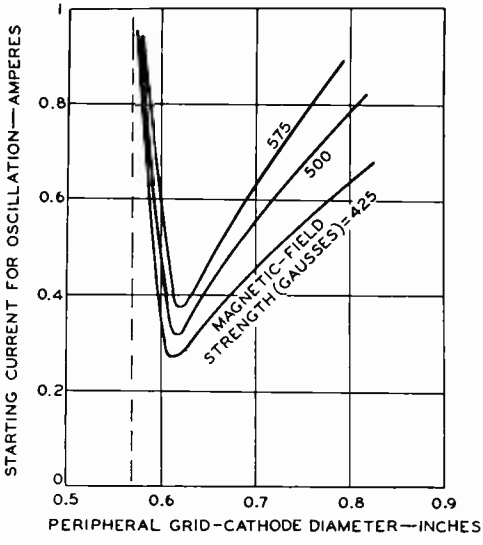

Fig. 7—Magnetron starting current as a function of grid–cathode diameter and magnetic field.

The magnetron, operated with a normal cathode 0.625 inch in diameter, started oscillations at an anode current of approximately 100 milliamperes. The curves in Figure 7 show that for over-all grid–cathode diameters of 0.56, 0.625, 0.7 and 0.775 inch, the lowest starting currents are obtained at an over-all grid–cathode diameter of 0.625 inch, the same as the prescribed diameter of the normal cathode. The starting current for this over-all diameter is of the order of three hundred milliamperes or three times the starting current of the unmodified magnetron.

Figure 8 is the performance chart of the grid-controlled magnetron in the absence of excitation by injected locking power. The anode currents are restricted to less than 0.8 ampere because the length of

cathode coating on the grid–cathode structures is only one inch, or two thirds of the length of coating used for the normal cathode. As is evident from Figure 8, the output of the nonexcited grid-controlled magnetron jumps to almost 100 watts following the start of oscillations and continues to over 600 watts. During the tests of several headers, this high output power was obtained even though one or more cathodes failed.

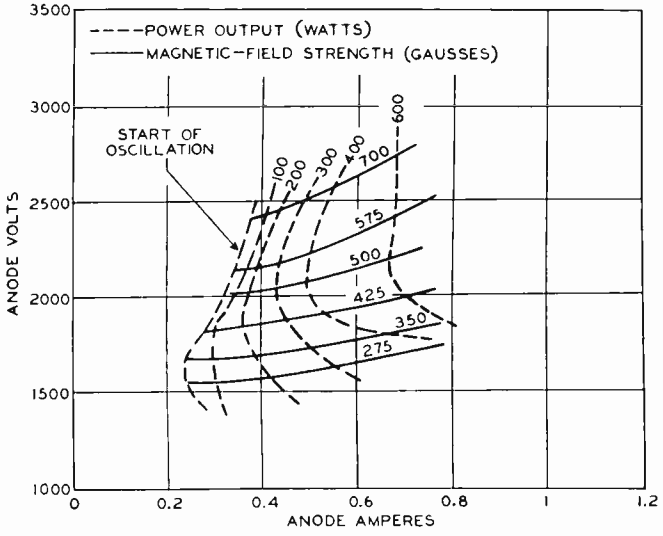

Fig. 8—Performance chart of grid-controlled magnetron when no locking signal is applied.

The header holes are designed so that the grid–cathode resonator is azimuthally oriented with respect to the anode resonator cavities to provide minimum coupling between the two resonators. The minimum coupling was verified by cold resonance measurements before the header was screwed to the tube. The nonexcited magnetron was made to oscillate at a high level, and a spectrum analyzer and a power bridge were coupled to the grid–cathode resonator. Wide-band noise components were observed, and higher-amplitude signal components in the vicinity of the oscillating frequency were of a level which measured less than 250 milliwatts of power. This power level was considered to represent satisfactory decoupling of the grid–cathode resonator from the anode resonator and to assure the operation of the tube as an

injection-locked oscillator in which the locking-signal source was not in turn driven by the oscillator and the locking signal was not directly developed in the output circuit.

Locking the Zero-Bias Grid-Controlled Magnetron

When a locking signal having the resonant frequency of the zero-bias grid–cathode resonator is injected into the resonator, the potential of the grid rods swings positive and negative with respect to the cathodes. While the potential of the grid rods is positive relative to the cathode, the grid rods collect electrons thereby forming an azimuthal periodic reduction in space-charge density close to the cathodes; this in turn enhances the locking process though loading the grid–cathode resonator.

When a locking-frequency signal of sufficient power is injected into the grid–cathode system within the locking bandwidth of the magnetron, the magnetron oscillations lock to the frequency of the injected signal.

The locking bandwidth is determined by sweeping the frequency of the locking signal slowly through the pushing-frequency range of the magnetron output. When the frequency of the locking signal approaches the magnetron pushing-frequency range, the magnetron frequency starts to "hunt," producing many side frequencies, and then locks to the frequency of the locking signal. The magnetron frequency will remain locked to the locking-signal frequency as the latter signal is varied until a frequency is reached at which the magnetron frequency will again hunt and then resume its free-running frequency. The difference between the upper and lower frequencies at which the magnetron frequency remains locked defines the locking bandwidth of the injection-locked magnetron.

The magnetron was successively operated at approximately 790 megacycles with a series of grid–cathode resonators of different diameters. A locking power of 30 watts was injected into the grid–cathode resonator of each, and locking bandwidths at different power levels up to 500 watts CW output were measured. The locking bandwidths of the order of the magnetron-pushing range of 3 megacycles were obtained with grid–cathode diameters slightly greater than the normal cathode diameter of 0.625 inch, as shown in Figure 9.

In experiments where the locking bandwidth overcame the magnetron pushing, the locking-signal frequency was set to approximately the frequency of the magnetron at highest power — near one end of the locking band. With the locking-signal power injected into the grid–cathode resonator, the output power of the magnetron could be varied

from a few milliwatts to full output power without any change in magnetron frequency by varying the anode–cathode voltage. For slowly varying changes in anode–cathode voltage or slowly varying locking-signal frequency, the magnetron frequency was locked with as little as 5 watts net locking power for power outputs up to 500 watts.

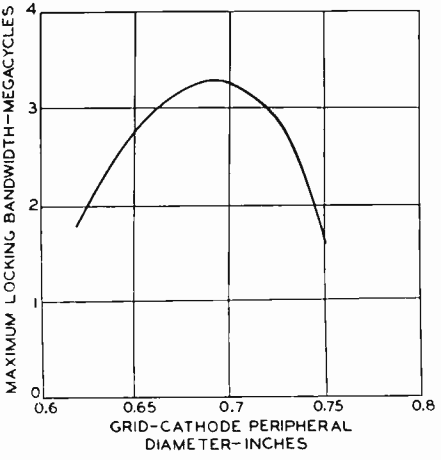

Fig. 9—Locking bandwidth as a function of peripheral grid-diameter in a zero-bias arrangement.

Negative-Bias Grid-Controlled Magnetron

For modulation systems requiring wide-band modulation, the grid–cathode structure was modified to permit negative biasing of the grid structure with respect to the cathodes.

Figure 10 is a cross-sectional diagram of the header and grid–cathode resonator structure used in the experiment. The grids and cathodes were identical in structure to those employed in the zero-bias experiments. The resonator structure differs from that diagrammed in Figure 4(a) in that it incorporates a quarter-wave choke. Thus, the grid and cathode assemblies, which represent portions of the outer and inner conductors respectively, of a resonant transmission line, are no longer conductively connected. The resultant structure is a half-wave, coaxial-line resonator having the cathode and grid assemblies incorporated into one end.

As shown in Figure 10, the resonator assembly, which includes a water-cooled chamber, is mounted on the header by means of ceramic spacers. A transmission line, which passes through the header and

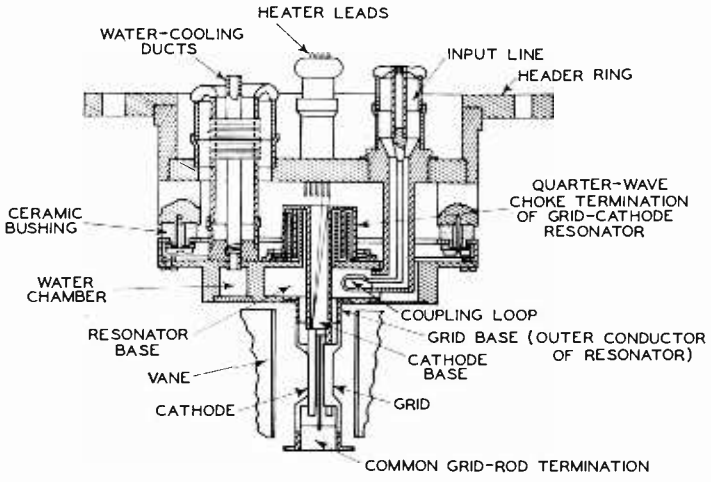

Fig. 10—Cross-sectional diagram of a negative-bias grid–cathode resonator arrangement.

terminates in a coupling loop, drives the resonator but does not contact the resonator wall. The header includes water cooling ducts.

Figure 11 is a photograph of the components of the grid–cathode resonator showing the grid and cathode structure and the choke. Included in the foreground are a pair of ceramic rings and a clamp used

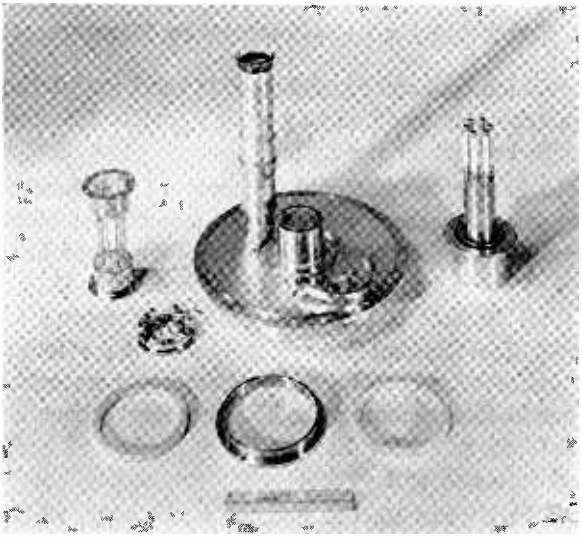

Fig. 11—Photograph of the component parts of negative-bias grid–cathode resonator structure.

for mounting and accurately positioning the center conductor (including the cathodes) of the grid–cathode resonator.

Figure 12 is a photograph of the assembled grid–cathode resonator and the header assembly onto which the grid–cathode resonator is mounted. The coupling loop is shown in the foreground of Figure 12. Except for the ceramics, the cathodes, the filaments, and the tube leading into the water cooling chamber, all parts of the grid–cathode resonator shown in Figure 12 are made of copper.

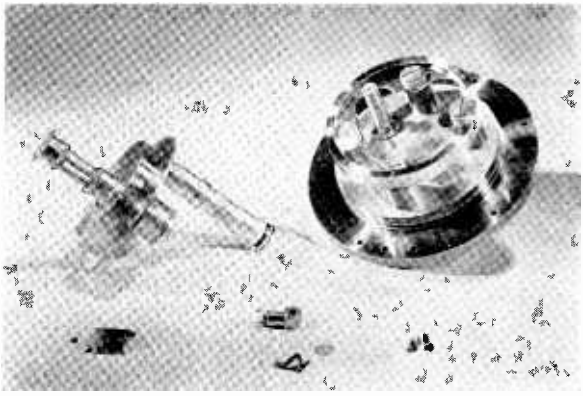

Fig. 12—Photograph of header and assembled structure of negative-bias grid–cathode resonator.

The heaters of the six cathodes are connected to a special connector ring shown behind the ceramic ring shown on the left in Figure 11 and shown mounted on the end of the resonator in Figure 12.

Figure 13 is a photograph of the experimental arrangement showing the grid-controlled magnetron, which was continuously pumped, positioned in an electromagnet. The output of this tube is connected to a high-power load and a spectrum analyzer is coupled to the output line to provide visual representation of the spectrum of the output power.

Locking the Negative-Bias Grid-Controlled Magnetron

A grid-controlled magnetron, using grid–cathode resonators of the type shown in Figure 12 and having a peripheral diameter of 0.675 inch, was operated without locking power applied to the resonator. When operated in the same manner as the zero-bias grid-controlled magnetron, this magnetron had substantially the same operating performance chart and starting-current characteristics.

Provisions were included in the test arrangement for the application of bias voltages as great as 1000 volts between the grids and the cathodes, with the grid biased negative relative to cathode. Figure 14 is a plot of the locking bandwidth as a function of net locking-signal power when the grid is biased at —300 volts and at —400 volts. This data was taken while the magnetron was producing a continuous-wave output power of 500 watts.

For negative bias voltages from zero to —300 volts, the magnetron-locking characteristics are very similar to those of the zero-bias grid-controlled magnetron. The maximum locking bandwidth obtainable is

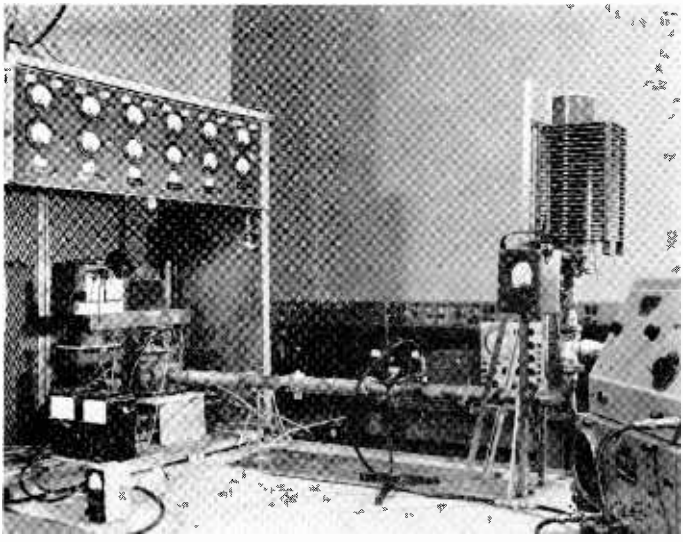

Fig. 13—Experimental setup for testing frequency-locked grid-controlled magnetron.

approximately 3 megacycles. As the net locking power is increased beyond 40 watts, the locking bandwidth decreases showing saturating characteristics due to the collection of electrons by the grid and due to back bombardment.

When the grid was biased 400 volts negative with respect to the cathodes, the collection of electrons by the grid structure was greatly reduced. As is evident from Figure 14, the negative grid bias of —400 volts relative to the cathode prevents saturation of the locking-signal power, and at this high power level, the locking bandwidth increases to 5 megacycles with increasing locking power. At low power levels, locking bandwidths of more than 10 megacycles are realized.

The decrease in locking bandwidth with increasing power is attributable to the increased space-charge density and the resultant reduction in potential in the vicinity of the cathodes. This increased space-charge density and further reduced potential has the effect of reducing the bunching action initiated by the traveling electric field of the grid–cathode structure.

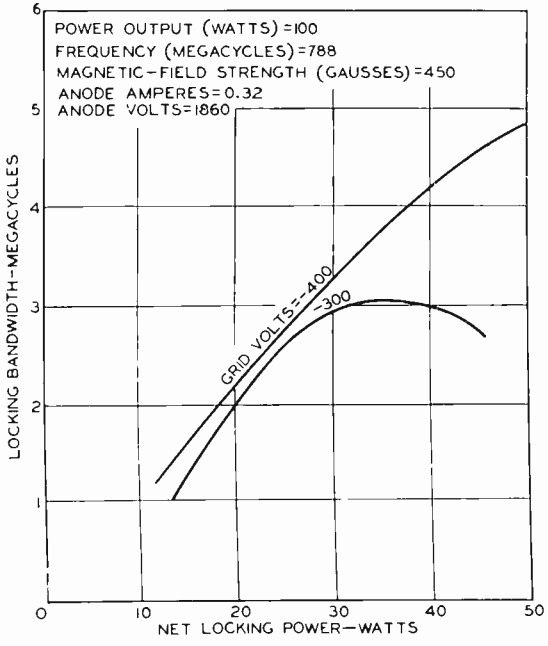

Fig. 14—Chart of locking bandwidth as a function of net locking power and negative grid bias.

The power output of the magnetron varied from substantially zero output power to a high output-power level of 500 watts with complete control of frequency by the injected locking signal. Point-by-point measurements of power output versus anode voltage as a function of both grid bias and magnetic field provided the curves shown in Figure 15. For a magnetic field of 375 gausses, the power output is a substantially linear function of the anode voltage. At the lower magnetic field of 250 gausses, the ability of the grids to "beam" the electron emission from the cathode into the interaction space is enhanced.

Complete and conclusive measurements of locking bandwidth on a dynamic basis rather than a point-by-point basis were beyond the scope of the program. It was possible, however, to use a video signal repre-

senting a test pattern containing signal components up to 4.5 megacycles to modulate the potential of the magnetron anode. The circuit used is shown in Figure 16(a); the frequency of the magnetron was injection-locked with 30 watts net power.

The video signal caused an excursion of output power from full power at a maximum of 600 watts down to a minimum of 3 watts, thereby producing a double-sideband, amplitude-modulated signal having a bandwidth of 9 megacycles. A detector included in the output load and coupled to a video monitor produced a representation of the received test pattern on the video monitor. Inspection of the lines in

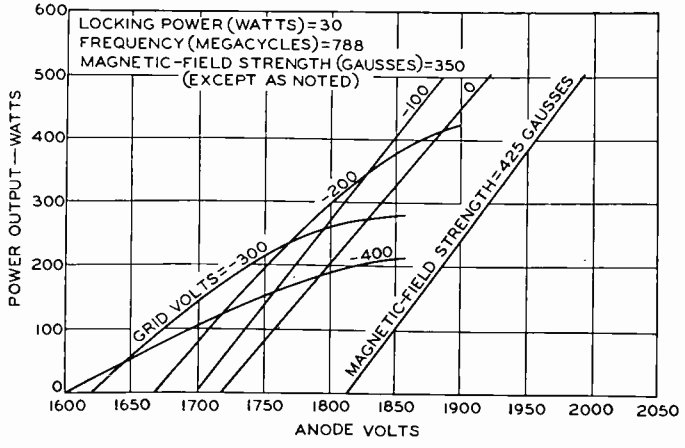

Fig. 15—Power output as a function of anode voltage and magnetic field.

the test pattern showed that the detail representative of the pattern information at 4.5 megacycles was reproduced by the video monitor. When the locking signal was turned off, the magnetron failed to produce output power in the vicinity of the lowest voltage of the anode during the modulation and failed to hold the carrier frequency constant. As a result, the picture "broke up."

General Aspects of Grid-Controlled Magnetron Usage

The preceding sections have described experiments conducted on the grid-controlled magnetron operated as a substantially continuous-wave tube modulated by a television signal. While this achievement indicates that a magnetron may be modulated to transmit high-definition information with an amplitude-modulated signal, other modulation applications are also highly feasible.

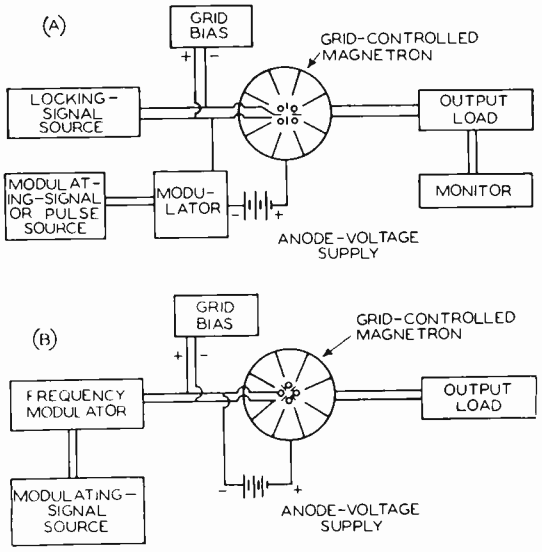

Fig. 16—(A) Circuit arrangement for amplitude modulating or pulsing a frequency-locked grid-controlled magnetron, and (B) circuit arrangement for frequency modulating a grid-controlled magnetron.

The modulator of Figure 16(a) may be a pulser and the grid-controlled magnetron may then be used to produce frequency-locked high-intensity pulses for radar systems, such as MTI radar, where the quality of frequency and phase lock determines the readability of the received information.

A frequency-locked grid-controlled magnetron is also suitable for use in a high-power frequency-modulation system. When a circuit of the type shown in Figure 16(b) is used, a low-power frequency-modulated locking signal will produce a high-power frequency-modulated signal at the output of the magnetron with minimum amplitude modulation. Such a system is capable of high power gain because the absence of anode modulation reduces the power requirements of the locking signal.

THEORETICAL AND EXPERIMENTAL STUDY OF WIDE-BAND PARABOLOID ANTENNA WITH CENTRAL-REFLECTOR FEED*

By

Peter Foldes and Steven G. Komlos

RCA Victor Company, Ltd.,
Montreal, Que.

Summary—*The theory and measurements of a circularly symmetrical high-gain paraboloidal antenna with a central reflector are summarized. The results of the experiments prove that the method of geometrical optics is sufficiently accurate for the pattern calculations. To obtain a reasonably accurate prediction of impedance behavior, however, the wave-theory method should be employed. Thus, it is possible to calculate the antenna shape required to produce the given radiation pattern, while the elements needed to assure an impedance match are determined experimentally.*

Introduction

In recent years after the solution of the basic problems, the development of microwave wide-band communication systems has been directed toward the achievement of exceptionally high quality at the lowest possible cost. To fulfill these requirements, the development of a new type of antenna was undertaken.

This antenna is part of a new, line-of-sight microwave communication system operating in the "R" band (1700 to 2300 megacycles).

The system itself utilizes frequency modulation and is designed to operate up to twelve radio-frequency channels (each with a nominal capacity of 600 message channels or, alternately, one monochrome or color-television signal). The system meets the recommendations of the International Radio Consultative Committee (CCIR).

The most important electrical specifications of this antenna are summarized in Table I. From this data it is evident that there are three main requirements: (1) high gain ($>$ 32 db), (2) low back-lobe level (see Figure 1), and (3) extremely small input VSWR. Also, it is desirable that the system be capable of radiating simultaneously two field components whose polarizations are at right angles to each other. Further, the antenna should have a simple mechanical structure, a small wind load, and maximum resistance to weather.

* Manuscript received August 20, 1959.

Table I

Gain	1700 mc	32.6 db	
	2300 mc	36.5 db	
		Peak	Average
Front-to-back ratio	1700 mc	52.0 db	58.0 db
	2300 mc	58.0 db	64.0 db
VSWR	500-mc bandwidth	1.06	1.04
	600-mc bandwidth	1.08	1.05

Polarization: Dual

Aperture diameter: 10 feet

There are several antenna systems, either in operation or described in the literature, which approximate the given requirements. Some well known examples are the horn-lens radiator, the hoghorn antenna, and the vertex-plate compensated paraboloid. The specified value of gain is easily satisfied by these antennas, but the requirements for a wide-band impedance match, small back-lobe level, and simple mechanical structure are not simultaneously achieved in any of these examples.

There are two main methods by which a wide-band impedance match may be produced:

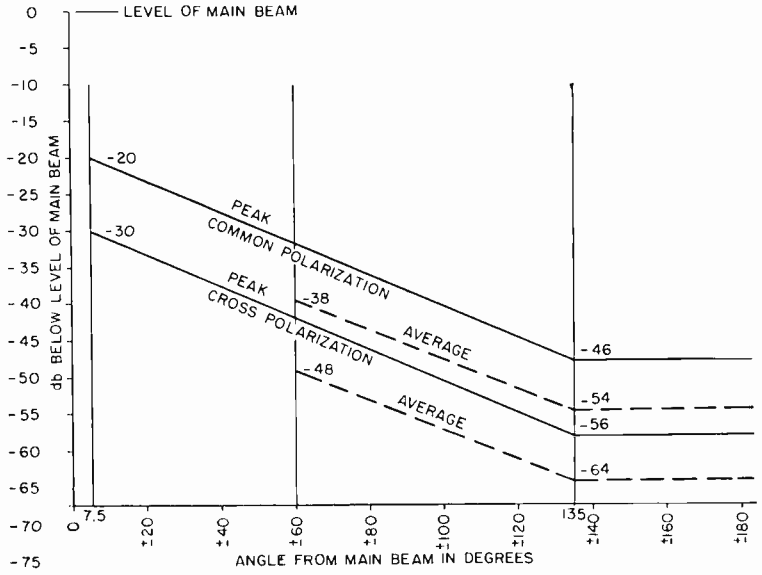

Fig. 1—Lobe structure specification of the antenna.

1. Placing the feed system outside the aperture field (lens radiator, or paraboloid with off-center feed)[1]
2. Cancelling the reflector's effect in the direction of the feed system (rotation of polarization, vertex plate, removing the vertex region of the reflector)[2]

The lens-type radiator fulfills all the electrical requirements, but its mechanical structure is complicated and both its wind load and its cost are high. The construction of the paraboloid with off-center feed is also complicated, and as a result of the lack of symmetry, cross-polarized radiation components appear, even in the main planes.

The rotation-of-polarization technique cannot be used in a system which simultaneously radiates two field components at right angles to each other. The vertex-plate technique requires very accurate adjustments at small focal distances, while at large focal distances the side- and back-lobes are usually high. Above all, the vertex plate always reduces the gain of the antena.

It was therefore decided to investigate an antenna which is similar to a circularly symmetrical hoghorn antenna. (The hoghorn antenna is designed specifically for radio relay use at frequencies of 4000 megacycles and above, and has all the electrical properties desired, but is large and heavy.) This antenna is related to those described by F. L. Henessy[3] and by A. C. Beck and H. T. Friis.[4*] Figure 2 shows the development of the new radiator from the hoghorn antenna. The frontal area of the hoghorn antenna is a sector of a circle (Figure 2a) but it is possible to use the whole circle as shown in Figure 2c. Exactly the same arrangement was used by William Cassegrain[5] two centuries ago for optical frequencies. With this arrangement it was possible to reduce both the height and depth of a paraboloid antenna and still retain the same useful area. When a reflector rather than a tapered coaxial horn is used to guide the waves, the screening effect of the feed system is reduced with a resultant increase in the gain and a reduction in the side lobes of the radiation pattern.

---

[1] A. A. Roetken, K. D. Smith, and R. W. Friis, "The TD-2 Microwave Radio-Relay System," *Bell Sys. Tech. Jour.*, Vol. 30, p. 1041, October, 1951.

[2] N. Ganapathy and P. E. Hopkins, "An Experimental Wide Band Parabolic Aerial for the 2,000 Mc/s Band," *Marconi Review*, Vol. 20, 1957.

[3] F. L. Henessey, *Naval Research Laboratory Report* No. 4071, October 22, 1952.

[4] A. T. Corbin and A. S. May, "Broadband Horn Reflector Antenna," *Bell Record*, Vol. XXXIII, No. 11, November, 1955, p. 401. A. C. Beck and H. T. Friis (U.S. Patent No. 2236393).

[*] A further development of this type of antenna was suggested by R. F. Privett and the authors.

[5] L. C. Martin, *Geometrical Optics*, p. 95, Philosophical Library, Inc., New York, 1956.

The preliminary calculations, used to determine the over-all geometry of the antenna from the point of view of pattern considerations, are based on the method of geometrical optics. The pattern measurements prove that this approach is reasonable, but this method gives only fair approximations to the impedance behavior of the antenna. Therefore, further modifications (for example, elimination of the central pin) are necessary to obtain a good impedance match.

As the aperture diameter was specified to be 10 feet, it seemed advisable to use a 1/3.3 scale model for the development work. This scale model was used to prove the operation principle, basically from the radiation standpoint. The final impedance-matching elements were developed on the full-size antenna. As a byproduct, the scale-model antenna proved to be a very wide-band, high-gain, communication antenna in the 5660-7660 megacycle band.

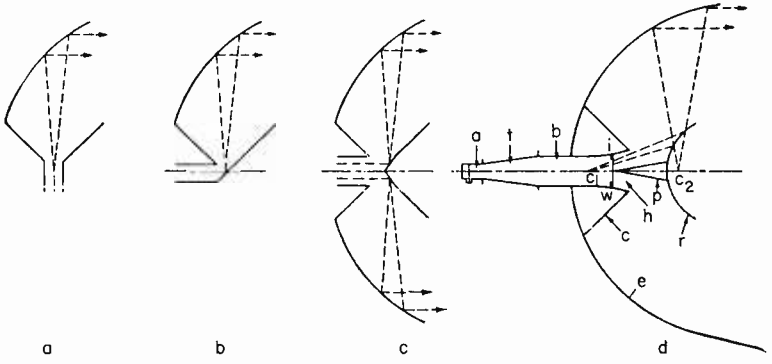

Fig. 2—The antenna as a circularly symmetrical hoghorn antenna.

Principles of Operation

The basic arrangement of the antenna is shown in Figure 2d. The principal parts of the antenna, shown in the figure, are as follows:

Standard rectangular waveguide propagating the TE_{10} mode (a),

Transition (t) which transforms the TE_{10} mode into the TE_{11} mode of the circular waveguide (b),

Horn section (h),

Iris (i),

Plastic window (w),

Central reflector (r) with a vertex plate (p), and

Paraboloid reflector (e) with a conical shaped central cover (c).

The central reflector should (1) act as a feeder which radiates spherical waves from the focal point of the paraboloid, (2) radiate the largest possible amount of energy toward the secondary reflector, and (3) radiate the smallest possible amount of energy back into the feed horn and in the opposite direction. Assuming that the central reflector fulfills all these requirements, the waves reflected from it behave as though they are radiated from a point source which has a radiation pattern directed towards the secondary reflector. The paraboloid (e) reflects these waves into space. The vertex plate (p) and the cover (c) decrease the amount of energy radiated back into the horn.

Assuming that the method of geometrical optics can be used to calculate the aperture distribution of the paraboloid, the phase distribution in the aperture is constant. The amplitude distribution across the paraboloid can be calculated from a knowledge of the given TE_{11} mode in the horn aperture and the geometry of the system. The amplitude maximum in the paraboloid aperture will be on an elliptical "ring" around the center of the aperture, as opposed to the conventional paraboloid antenna system where the field maximum is in the center. This shift of the maximum towards the edges of the paraboloid increases the gain over that of an ordinary paraboloid antenna system. At the same time, the screening effect caused by the central reflector increases the side-lobe level compared to the paraboloid antenna.

The only way to decrease this screening effect of the central reflector is to reduce its diameter. Unfortunately, this increases the diffraction around the edge of this reflector. The proper size of this element is thus a compromise. If the diameter of the paraboloid is fixed and the wavelength is decreased, then the situation improves rapidly, since the diameter of the central reflector (measured in wavelengths) increases without increasing the screening effect.

If the method of geometrical optics were used to calculate the back-reflection properties of the central and paraboloid reflectors, then the reflection coefficient would be 0 per cent. But this method is only approximate, even in the case of reflectors whose dimensions are relatively large compared to the wavelength. This not being the present case, the central reflector will have a finite reflection towards the feed horn, the magnitude of which is nearly impossible to establish except by experimentation. The paraboloid has a definite, but much smaller effect on the feed than in the case of the usual horn or dipole feed systems. This results principally from the fact that the central part of the paraboloid, which would give the bulk of the reflections, is lightly illuminated.

A major advantage of this antenna system is that the necessary compensating elements (cover and central pin, or vertex plate, on the central reflector) do not affect the main radiation as much as they do in the ordinary vertex-plate technique, where the compensating element is placed in the most highly illuminated region of the paraboloid.

Determination of Geometry and Design Considerations

In this section the geometry of the antenna system, mainly the $y = f(x)$ and $\rho = g(\psi)$ functions for the two reflectors are determined (see Figures 2(d) and 3). There are four quantities which must be

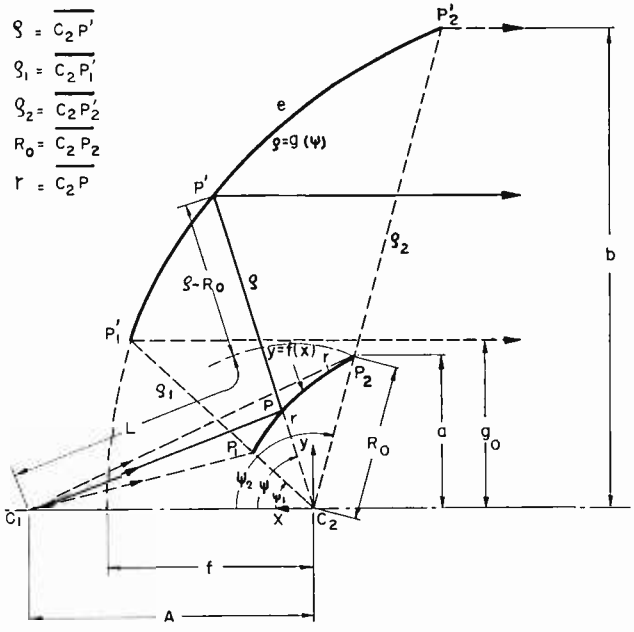

Fig. 3—Coordinate system for determination of the reflector surfaces.

established in advance from different radiation and impedance considerations:

b = the half-aperture diameter,

b/f = the ratio between the half-aperture diameter and the focal length of the paraboloid,

A = the "focal length" of the center reflector, and

$T = 1 - (a/b)^2$ the screening coefficient.

The curve represented by the $\rho = g(\psi)$ is chosen to be a parabola which has an aperture size $D = 2b$, given as 10 feet by the specification. Thus the only free parameter for the $\rho = g(\psi)$ curve is the focal length (f).

An increase in the focal length will decrease the depth of the paraboloid. Generally, this decreases the cross-polarized components of the radiation and simplifies the manufacturing of the paraboloid. On the other hand, an increase in the focal length of a fixed-feed system increases the side and back radiation. In the present case, the focal length has a large influence on the shape of the curve y and especially its end points (i.e., ψ_1 and ψ_2). If the focal length increases, the ψ_2 aperture angle decreases (see Figure 3). Thus the radiation of the feed must be more directive. This increases the size a, and the y curve becomes flatter, resulting in higher reflection coefficient at the input of the system. Thus, it is advisable to choose a relatively small value for f.

The shape of the $y = f(x)$ curve is influenced by two parameters: the distance between the axis and its end point, a, and the "focal" length of the center reflector, A. The former determines the screening effect, while the latter determines the curvature of the reflector and, hence, the impedance properties of the system. The length A is called the focal length since the reflector focuses the negative spherical waves travelling towards point C_2 at point C_1 when the system is used as a receiving antenna.

The spherical wave originating at point C_1 must be reflected by the $y = f(x)$ curve as another spherical wave with the point C_2 as center. After a second reflection from the paraboloid, it must give a plane wave in the paraboloid aperture. Mathematically,

$$(A - x)^2 + y^2 = [L - (R_0 - r)]^2 = (B + r)^2, \tag{1}$$

where $$B = L - R_0 \qquad \text{and} \qquad r = (x^2 + y^2)^{1/2}. \tag{2}$$

The function $\rho = g(\psi)$ is a parabola with the point C_2 as focus. Mathematically,

$$\rho = \frac{f}{\cos^2 \frac{\psi}{2}}, \tag{3}$$

where ρ and ψ are polar coordinates (see Figure 3).

The definition of the ψ_2 aperture angle is given by

$$\rho_2 \cos\left(\psi_2 - \frac{\pi}{2}\right) = \rho_2 \sin \psi_2 = b. \tag{4}$$

From Equation (1),

$$A^2 - 2Ax + x^2 + y^2 = B^2 + 2Br + x^2 + y^2,$$

$$\frac{A^2 - B^2}{2B} - \frac{A}{B}x = r. \tag{5}$$

Combining with Equations (2),

$$y = (\alpha x^2 + \beta x + \gamma)^{1/2}, \tag{6}$$

where

$$= \frac{A^2 - (L - R_0)^2}{(L - R_0)^2}, \quad \beta = A\frac{(L - R_0)^2 - A^2}{(L - R_0)^2}, \quad \gamma = \left[\frac{A^2 - (L - R_0)^2}{2(L - R_0)}\right]^2. \tag{7}$$

The aperture dimension of the horn must be chosen so that the major part of the spherical waves originating at C_1 impinge on the central reflecting surface. In this case, most of the energy travels between the two rays $C_1P_1P'_1$ and $C_1P_2P'_2$.

For $\psi = \psi_2$,

$$y = a = R_0 \cos\left(\psi_2 - \frac{\pi}{2}\right) = R_0 \sin \psi_2$$

or

$$R_0 = \frac{a}{\sin \psi_2} \tag{8}$$

and

$$x = x_0 = R_0 \cos \psi_2. \tag{8a}$$

Since $L = \overline{C_1P_2}$ by definition,

$$L = \lfloor (A - R_0 \cos \psi_2)^2 + a^2 \rfloor^{1/2} = \lfloor A^2 - 2AR_0 \cos \psi_2 + R_0^2 \rfloor^{1/2}. \tag{9}$$

From Equations (3) and (4),

$$\frac{b}{f} = \frac{\sin \psi_2}{\cos^2 \frac{\psi_2}{2}} \equiv S(\psi_2), \tag{10}$$

and

$$f = \frac{b}{S(\psi_2)}. \tag{11}$$

The dimension a can be determined by the screening coefficient. The screening coefficient is the ratio of the unscreened to the total aperture areas, namely:

$$T = \frac{\pi b^2 - \pi a^2}{\pi b^2} = 1 - \left(\frac{a}{b}\right)^2, \tag{12}$$

or

$$\frac{a}{b} = (1 - T)^{1/2}. \tag{13}$$

Finally,

$$\rho_1 \sin \psi_1 = f \sin \psi_1 \frac{1}{\cos^2 \frac{\psi_1}{2}} = a, \tag{14}$$

where it is assumed that $g_0 = a$.

From Equations (1) through (14), therefore, it is possible to determine all the necessary geometrical data of the two reflector systems. Figure 4 is a calculation graph for this purpose. The basic data which serves as the source of the calculations is in double squares, while the end results are shown in double circles. The numbers refer to the equations which must be used.

Calculations were made for a model antenna with aperture size $2b = 36$ inches, and the best compromise was $b/f = 2.55$. The calculations were made with different A values ranging from 3.94 to 13.3 inches, and the optimal value of 3.94 inches was finally chosen. For every value of ψ_1, there is a maximum value of A beyond which there is no solution. Decreasing the value of A increases the curvature of the surface while at the same time decreasing the largest possible value of a.

There is one more parameter, the screening coefficient T, which must be properly chosen in advance. Figure 5 shows the variation of

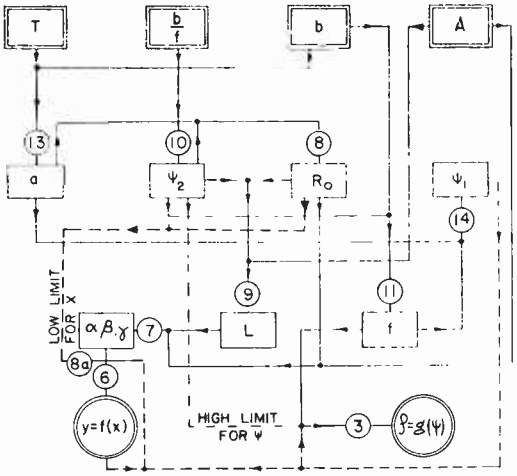

Fig. 4—Calculation graph of the antenna geometry.

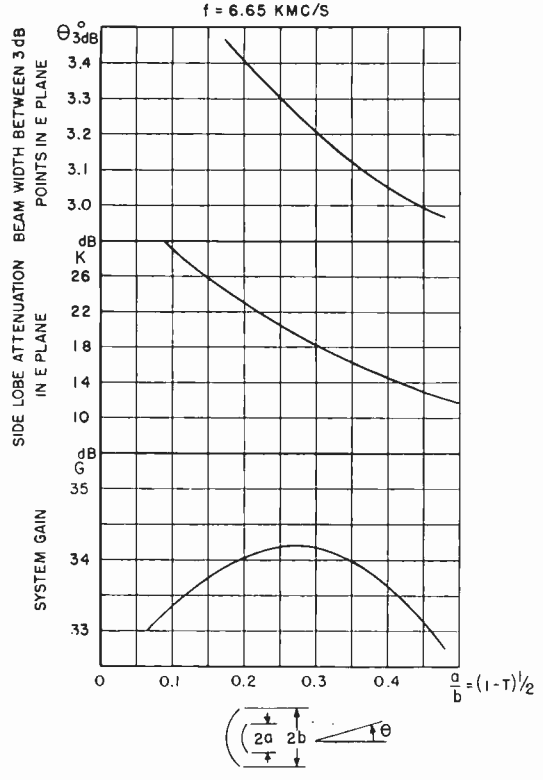

Fig. 5—Calculated beam width, side-lobe attenuation, and gain versus a/b.

the beam width in the E plane, the side-lobe attenuation, and the gain as a function of a/b. The pattern calculations were made for the middle frequency of the model ($f = 6650$ megacycles) with the following simplifying assumptions:

1. Uniform polarization distribution exists in the aperture plane. This assumption affects the E and H plane patterns only slightly.

2. The exact field-amplitude distributions in the aperture can be approximated by the following function:

$$f(r) = 0, \qquad \text{if} \qquad 0 \leq r \leq \frac{a}{b},$$

$$f(r) = k_1 + k_2 (1 - r^2)^2, \qquad \text{if} \qquad \frac{a}{b} < r \leq 1,$$

where $r = (\rho'/b)$ is the normalized and ρ' is the actual distance measured from the center of the aperture, and k_1 and k_2 are two appropriate constants. The given amplitude distribution takes into account only the amplitude transformation effect of the central and paraboloid reflectors and assumes constant field in the horn aperture. Thus, this assumption is less valid for the H-plane aperture distribution than for the E-plane (see Figure 6).

3. The phase is constant across the aperture. This implies that the central reflector gives a perfectly spherical wave, C_2 coincides with the focal point of the paraboloid, and the paraboloid itself is geometrically exact.

4. The side radiation of the horn, and the diffraction around the central reflector can be neglected.

To meet the specified side-lobe level for the radiation close to the axis, the use of a small reflector is dictated (see Figure 5). Unfortunately, the diffraction around the central reflector increases in this case, causing an increase in the large-angle side lobes. From Figure 5, it can be seen that the beam width decreases as the a/b ratio increases, because the maximum of the aperture amplitude distribution shifts nearer to the edge of the paraboloid. This effect, however, increases the level of the small-angle side lobes at the same time. Theoretically, a 17-18 db side-lobe level at small angles corresponds to the condition of maximum gain. This feature of the ring aperture

can be used advantageously when it is necessary to have maximum gain with a given aperture size and the side lobes are of less importance.

It is worthwhile to note that the antenna system contains the following discontinuities which may give relatively large reflections:

(a) Rectangular to circular waveguide transition (0.5%)
(b) Throat range of the feed horn (1%)
(c) Aperture of the horn (5%)
(d) Central reflector (15%)
(e) Paraboloid reflector (3%)

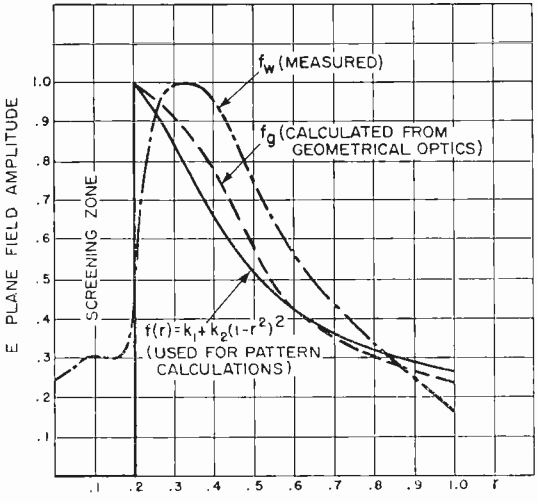

Fig. 6—Typical aperture distribution in E plane.

The wide-band compensation of these reflections is possible only when compensating elements are built into the system close to these discontinuities.

Results of Measurements on the Scale Model

A model with a scaling factor of 1/3.3 was built to provide experimental results. This scale made it relatively easy to change and try out different feed arrangements and, finally, to find the optimum geometry, at least as far as the radiation of the antenna was concerned. With the scale model it was possible to determine, among other characteristics, the optimum feed-system pattern, the far-field pattern, and the gain of the antenna.

Investigation of the feed pattern showed that, depending on the distance between the horn and the central reflector, there are two very distinct modes of propagation. One is the so called "reflector mode," which corresponds to a relatively great distance (approximately 2.8 inches in the model) between the horn and central reflector; the other is the "guided mode," which corresponds to a much smaller distance (0.8 inch). In the latter case, the central element acts as a guide, and the actual radiator is the ring slot which lies between the horn and the reflector. There is a sharp difference between the reflector and guided mode from both the radiation and impedance standpoint. In the guided mode, the field behind the central reflector is small, but the main beam of the feed illuminates the paraboloid at

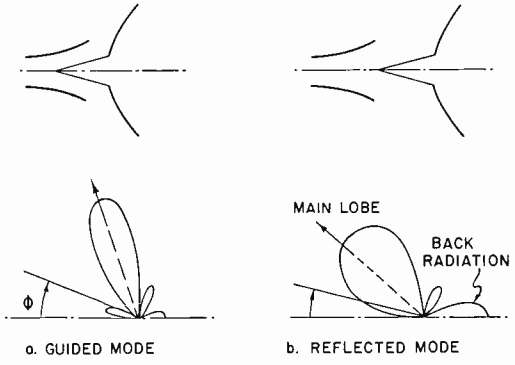

Fig. 7—Guided and reflected radiation modes.

very large angles. Consequently, the screening effect of the reflector is high. The reflector mode, on the other hand, results in a better illumination in the central part of the paraboloid aperture and at the same time the input-reflection coefficient is low.

Figures 7 and 8 illustrate the pattern shapes of the two modes, while Figure 9 shows the variation of the angle of maximum radiation (ψ_m) and the ratio between the back radiation and the maximum of the main beam (α). In the final analysis, the reflector mode of operation was more suitable from the point of view of both far-field measurements and impedance measurements.

Figure 10 shows the frequency dependence of the far-field pattern of the optimum arrangement. Two important features are evident:

1. The first side-lobe level is relatively high. This effect can be attributed to the screening effect of the central reflector and

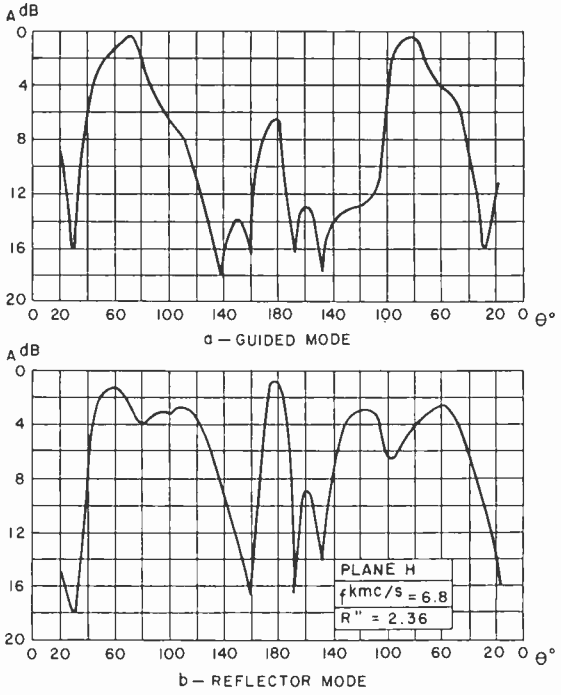

Fig. 8—Measured patterns of the feed system.

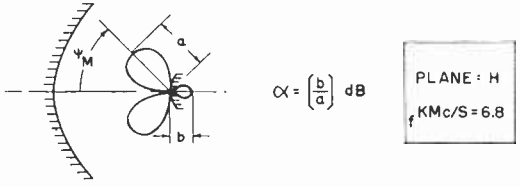

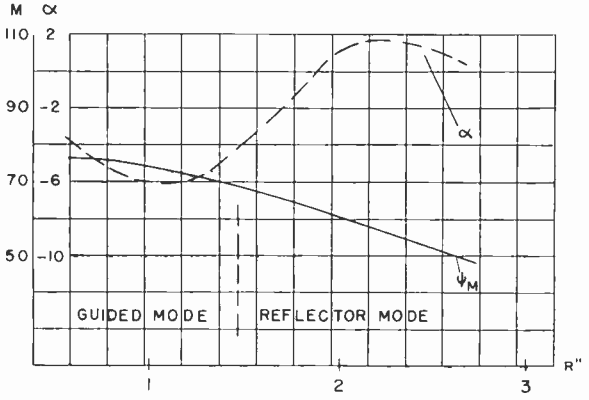

Fig. 9—Angle of maximum radiation and amplitude of back radiation versus R.

small mechanical asymmetries. (In the full-size antenna, the mechanical symmetry was improved and the pattern became symmetrical.)

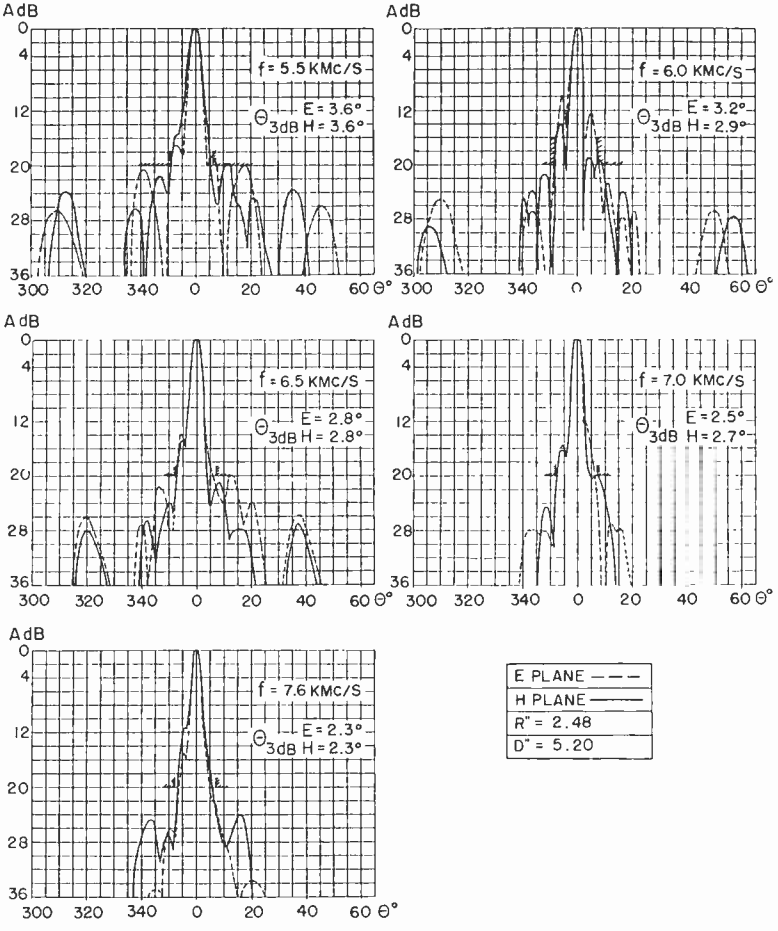

Fig. 10—Far-field pattern at various frequencies.

2. The angles between the 3 db points are smaller than is usual with a paraboloid of this diameter, thus the gain is slightly higher. Although the focal point of the paraboloid is well defined, the phase center of the feed system is only approximately determined by the calculations, and the position of the feed system within the paraboloid dish has to be established

experimentally. Figure 11 shows the 20-db beam width (θ_{20db}) as a function of D and R for two different central-reflector sizes (characterized by the screening coefficient).

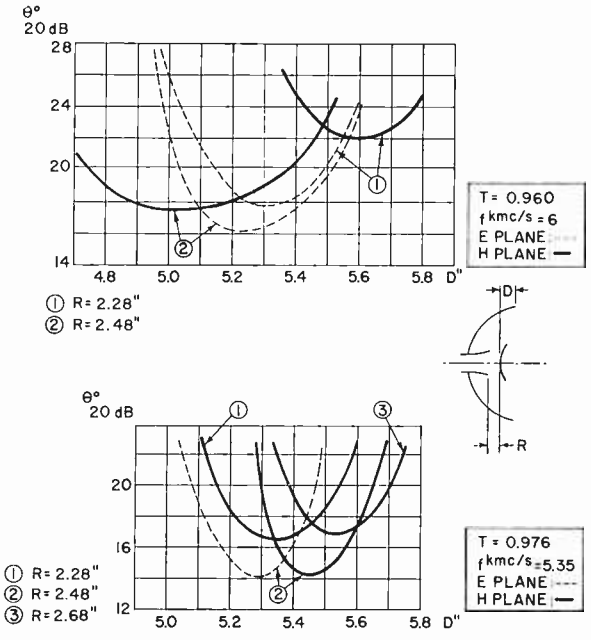

Fig. 11—Beam width between 20 db points (θ_{20db}) versus D.

FULL-SIZE ANTENNA

Mechanical Design

It was specified (Table I) that the antenna is to operate in the frequency range of 1700 to 2300 megacycles. Having obtained very promising results with the model, the full-size antenna designed for this range was built and tested.

The mechanical design was the result of a compromise between severe electrical and mechanical specifications and cost considerations. The antenna and feed, under a ½-inch coat of ice, must withstand gusts of up to 120 miles per hour without structural damage. The radiated beam must not change its direction by more than ±0.3° with a change in wind velocity from zero to 70 miles per hour. The operating temperature range is —54° C to +65° C, and the feed-horn pressurization is 1 psi.

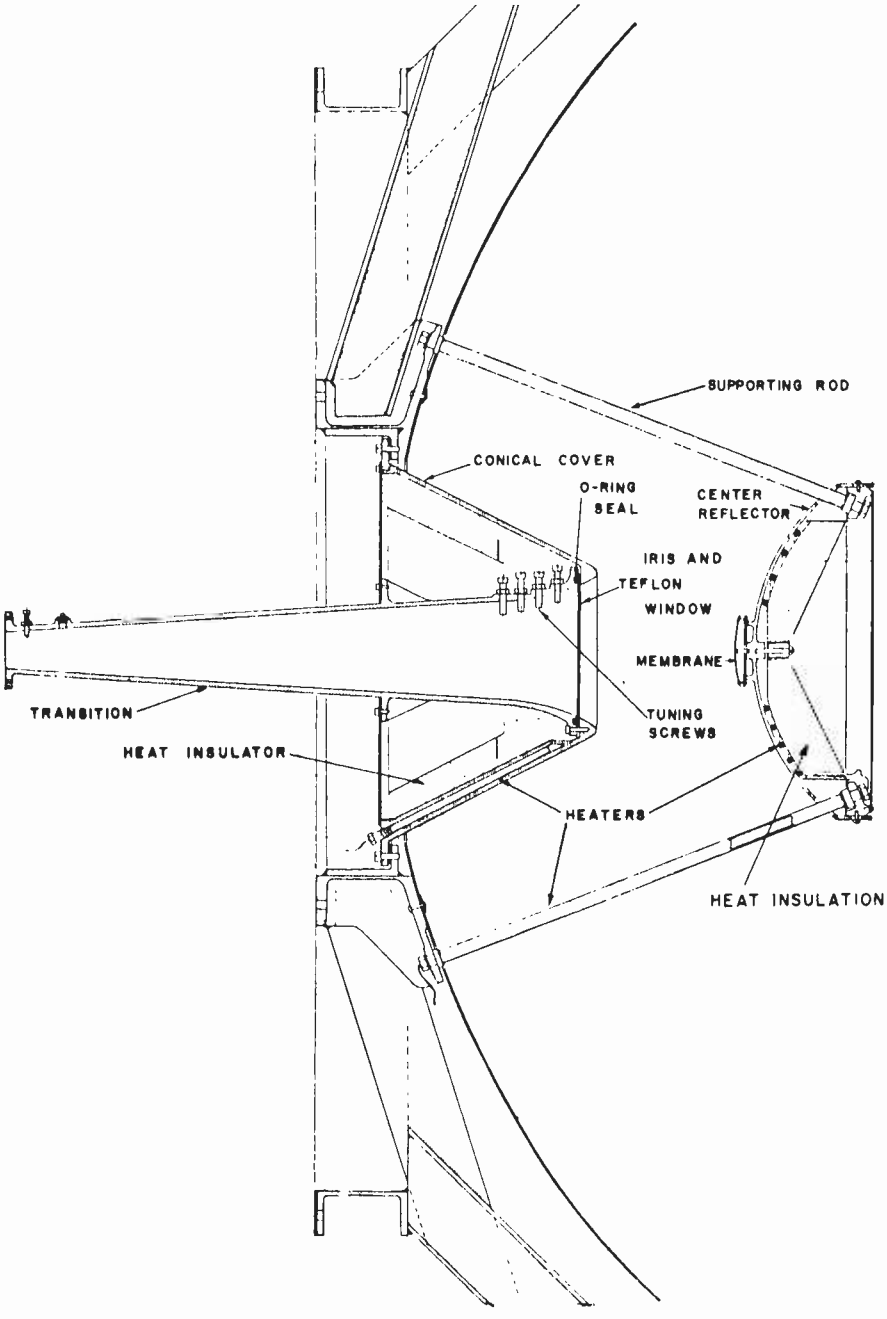

Fig. 12—Outline drawing of the feed system.

While the gain of the antenna is almost completely independent of any practical ice load, it was found that the impedance match of the antenna is sensitive to ice formation on the feed horn and on the central reflector. Therefore, a heating system was designed which supplies a maximum of 2.5 kw of power for deicing these elements. The heater elements are independent of the rest of the antenna and can be installed or replaced from the rear of the antenna without disturbing the electrical operation. In another version of the antenna, a plastic radome is placed around the feed system and no heating is required.

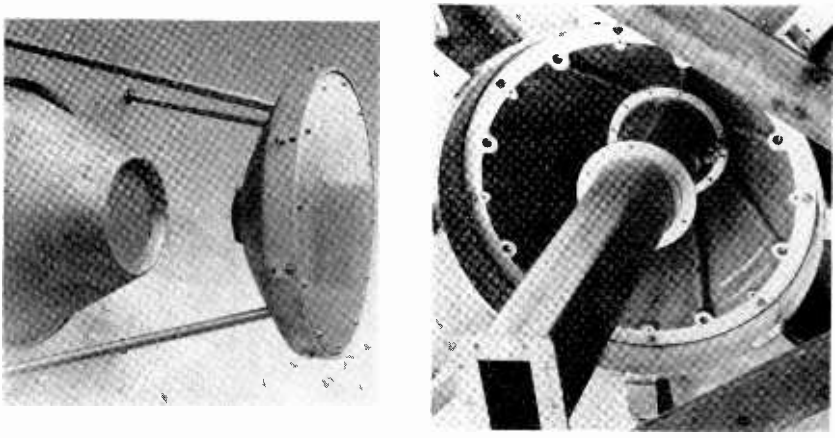

Fig. 13—Front (left) and rear (right) view of the feed system.

Figure 12 shows the construction of the feed system, and Figures 13a and 13b show the actual appearance. Because the transition horn and the central reflector were made as castings, good reproducibility was readily attained. Moreover, it is possible to keep the size and the tolerances of the compensating elements (vertex plate, aperture iris, tuning screws) within practical limits. The most important result obtained from the full-size antenna, particularly from a mechanical point of view, was the fact that a vertex plate alone, without the original center pin, was sufficient to compensate for the reflections from the central reflector. Thus, the design of tne complete structure was simplified and the pressurization of the feed horn was easier to accomplish.

The reflection from the paraboloid back to the horn was small to start with, and it was further decreased by the use of a properly shaped

conical cover around the feed horn. At the early stage of the development work, the center reflector was supported by rods made of insulating material, but these were later replaced by metallic rods. The change in the electrical characteristics were insignificant and amply justified the better rigidity of the structure. The feed horn can be removed from the rear of the antenna, as can be seen from Figures 13a and 13b, thus simplifying the servicing procedure of an installed antenna. The complete antenna system is shown in Figures 14a and 14b.

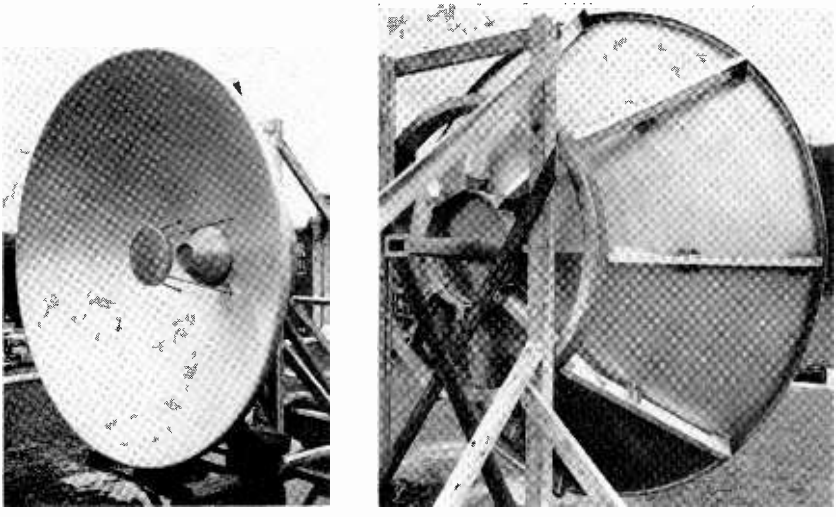

Fig. 14—Front (left) and rear (right) view of the antenna.

Far-field pattern

The complete far-field pattern was measured at the RCA antenna measuring site Gibbsboro, New Jersey. Although this site is relatively clear, it is possible that some nearby objects influenced the measurement accuracy, particularly in the back-lobe region. The separation between the transmitter and measured antenna was about half a mile. The available signal generator and receiver resulted in a power range of 60 db, with ±1 db calibration accuracy.

In the proposed system the front-to-back ratio of the radiator is of particular interest. Under the above circumstances the following front-to-back ratio was measured in the $150° < \theta < 180°$ angular range.

	Front-To-Back Ratio (db) Peak	Estimated Average*
Common Polarization	—56	—64
Cross Polarization	—59	—67

* All data averaged in the frequency band.

The diagrams in Figure 15 show the main and cross-polarized patterns at different frequencies.

VSWR Characteristics

Optimum VSWR characteristics can be obtained by adjustment of the vertex plate and four tuning screws in the feed horn. The vertex plate is constructed from a flexible metallic membrane, which can be adjusted by a screw from the rear of the central reflector.

To simplify the tuning process, a waveguide directional coupler was developed with 50 decibels directivity, and a high-power r-f sweep generator was used. With this equipment, it is possible to tune the individual antennas of a production run to a VSWR < 1.06 over a frequency band of 500 megacycles. The shape and position of the VSWR pattern can be controlled easily and the VSWR adjusted to a lower value when a narrower frequency band is required. The center of the optimum VSWR band can be shifted anywhere between 1700-2300 megacycles. Figure 16 indicates a typical input VSWR curve.

Conclusions

The experimental work has demonstrated that the new antenna system results in a wide-band, high-gain, low input reflection coefficient antenna. The experimental results are close to the calculations. The main features of the antenna are:

1. Its gain is approximately 1.5 decibels higher than the specified value over the entire frequency range.
2. The side-lobe radiation beyond $\theta = 8°$ (where θ is the angle measured from the axis of the main beam) is more than 20 decibels below the level of the maximum, over the entire frequency range.
3. In the above frequency range, the average of the back-radiation peak (in the angular range $150° < \theta < 210°$) is better than —56 decibels for the main polarization component and better than —59 decibels for the cross-polarized field component.

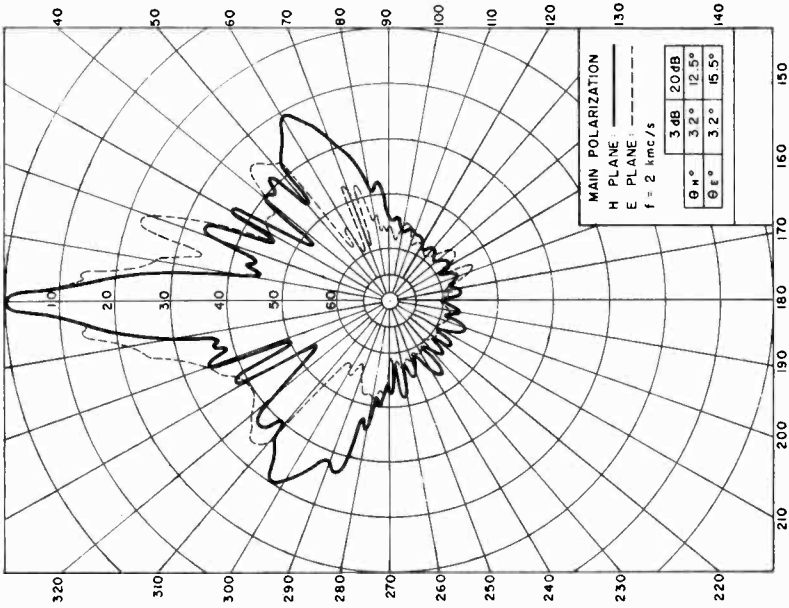
MAIN POLARIZATION
H PLANE
E PLANE
f = 2 kmc/s
3 dB 20 dB
θH° 3.2° 12.5°
θE° 3.2° 15.5°
b

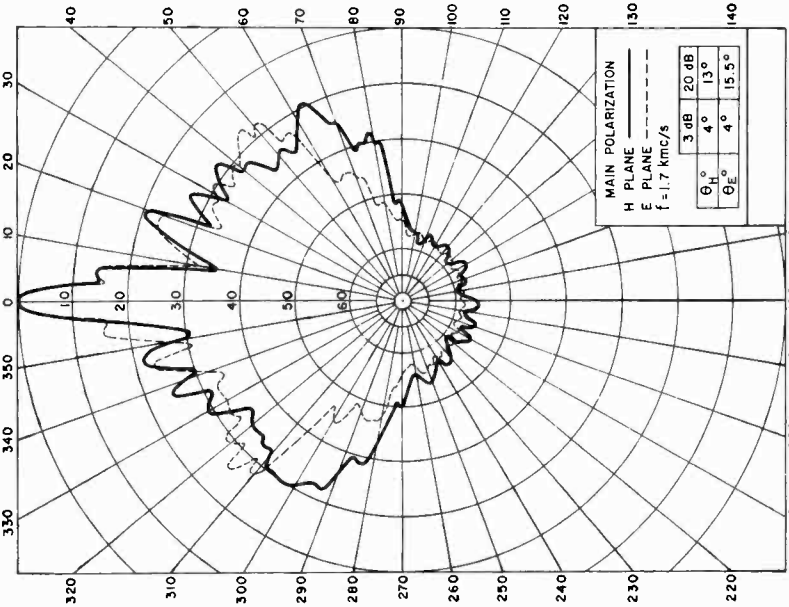
MAIN POLARIZATION
H PLANE
E PLANE
f = 11.7 kmc/s
3 dB 20 dB
θH° 4° 13°
θE° 4° 15.5°
a

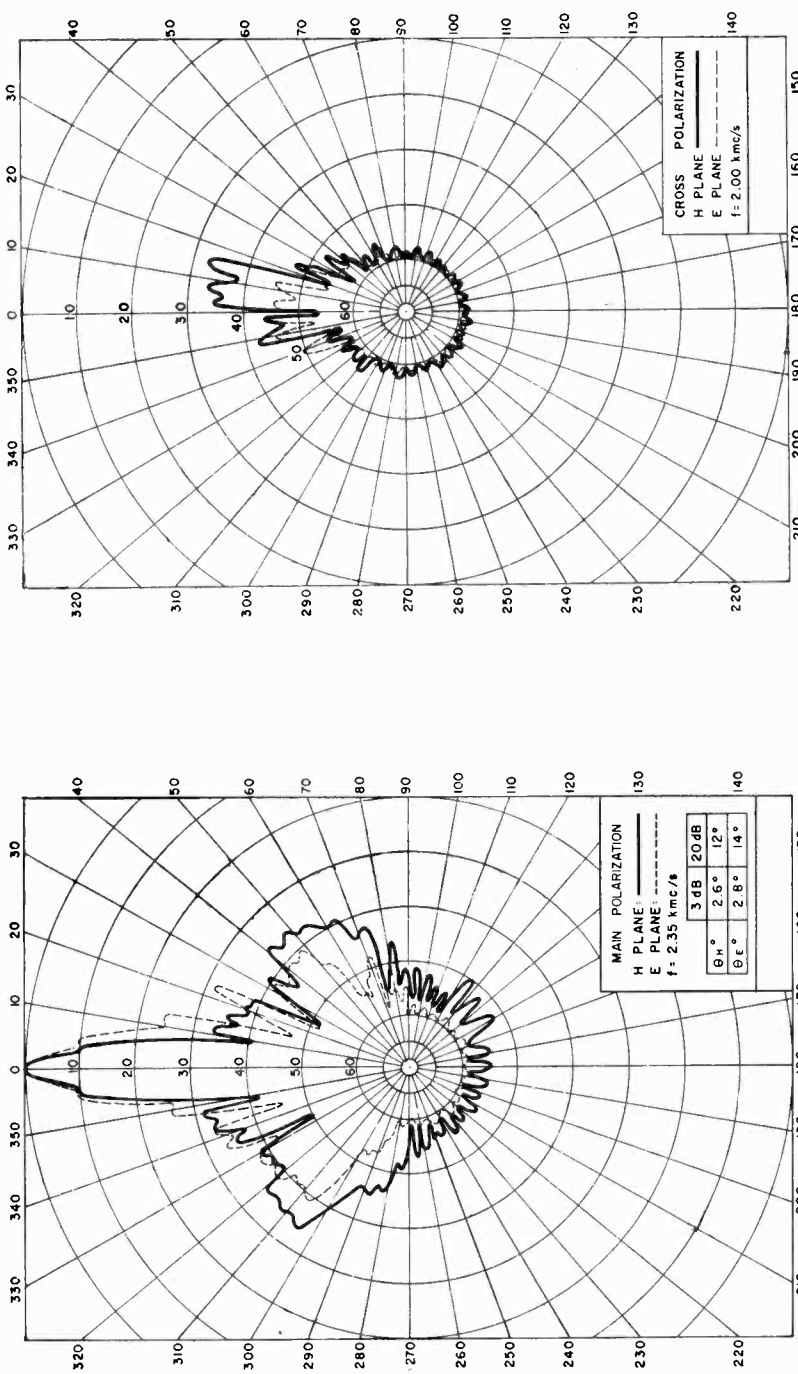

Fig. 15—Far-field radiation pattern (a) at 1700 Mc (main polarization), (b) at 2000 Mc (main polarization), (c) at 2350 Mc (main polarization), and (d) at 2000 Mc (cross polarization).

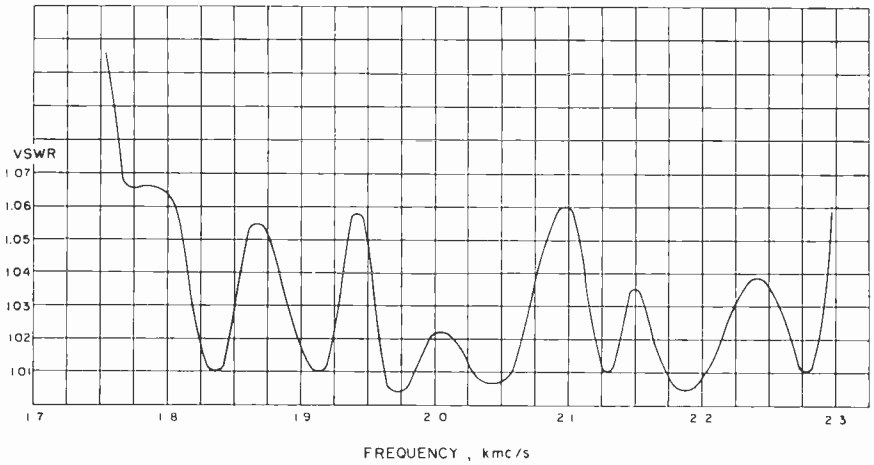

Fig. 16—Input VSWR of the antenna (average VSWR: 1.032).

4. With the present transition and antenna system, it is possible to obtain a VSWR < 1.08 within ± 15 per cent relative frequency band or a VSWR < 1.06 within ± 12 per cent relative frequency band.

ACKNOWLEDGMENTS

Acknowledgments are due to those members of the Antenna Group of the RCA Victor Company, Ltd., Montreal, who participated in the work described. Particular thanks are due to G. B. MacKimmie for corrections and helpful suggestions regarding the manuscript. The work was carried out as part of the MM-600 Microwave Link System Development.

IMPROVED ANTENNAS OF THE RHOMBIC CLASS*

By

Edmund A. Laport** and A. C. Veldhuis†

Summary—*Antennas are described that provide greater sidelobe suppression than conventional rhombic antennas, yet retain all the desirable features of the latter. Measured radiation patterns from a scale model, and from a full-scale double-rhomboid antenna are given. Simultaneous transatlantic transmissions with this antenna and with a conventional rhombic antenna at 10 megacycles are compared.*

Introduction

THE need for cleaner radiation patterns in HF operation has been well stated by Brueckmann.[1] Long-wire antennas always radiate large numbers of sidelobes distributed over the enclosing sphere, and simple wire configurations, such as the rhombus, cannot provide destructive wave interference at all angles to suppress these undesirable sidelobes adequately.

Sidelobe reduction is a matter of finding conductor configurations and current distributions that provide an exceptional degree of destructive interference in all directions except that desired for the main beam. The antennas described here, which may be considered as new wire configurations for antennas of the rhombic class, provide a versatile means for sidelobe control. With only a slight increase in structural complication, they can have substantially lower sidelobe radiation than standard horizontal rhombic antennas with the corollary gain improvement. The desirable properties of the rhombic antenna are preserved in all other essential respects. These antennas also suggest more complicated arrangements of wires by which even higher degrees of sidelobe suppression can be obtained.

Design

Figure 1 shows one antenna consisting of two rhomboid elements connected in parallel at their common apex where the balanced feeder is to be connected. By judicious choice of side lengths and apex angles,

* Manuscript received November 18, 1959.

** Radio Corporation of America, Princeton, N. J.

† Wind Turbine Co., West Chester, Pa.

[1] H. Brueckmann, "Suppression of Undesired Radiation of Directional HF Antennas and Associated Feed Lines," *Proc. I.R.E.*, Vol. 46, p. 1510, August, 1958.

destructive interference in the sidelobe zone can be controlled very much at will without restricting the choice of vertical angle of the main beam.

A double-rhomboid antenna designed for a high order of sidelobe suppression at one frequency retains this property very well over a substantial frequency range, as can be seen in Figure 4.

The design principle involved is the same as for the "vee" and the rhombic antennas where the array radiation pattern is the product of the patterns for the component sides at all points in space. There are zeros in the array pattern at all points in space where there is a zero

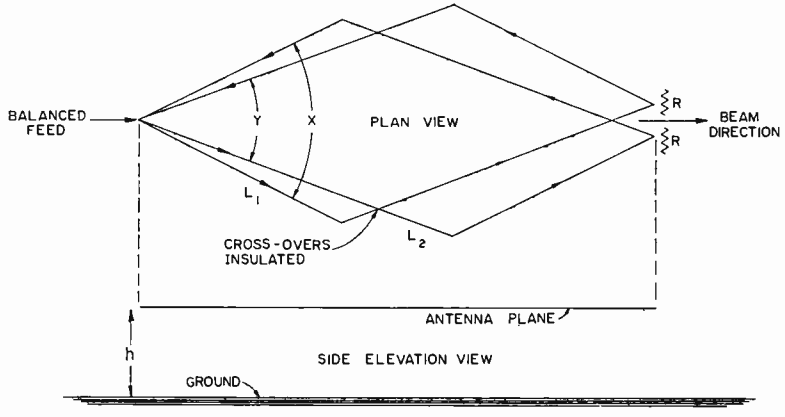

Fig. 1—Double-rhomboid antenna configuration. The only connection between rhomboids is at their common feed points.

in the pattern of any component side. Thus, the suppression of sidelobes is a matter of distributing the zeros outside of the main beam zone in a manner that inhibits lobe growth. The height factor also contributes to the array pattern of a horizontal antenna with its own distribution of zeros. The design objective is to align the main lobes from the component sides to form the main beam by coherent addition of array and ground-reflected fields while avoiding coherence of component secondary lobes elsewhere in surrounding space.

The rapid selection of lengths and angles that accomplish this requires a computing aid that reveals the complete radiation pattern at once. Stereographic transparent charts perform this function very effectively, as shown in Figure 2. Figure 3 illustrates a further extension of this method into a quadruple rhomboid configuration that suggests a very high order of sidelobe inhibition.

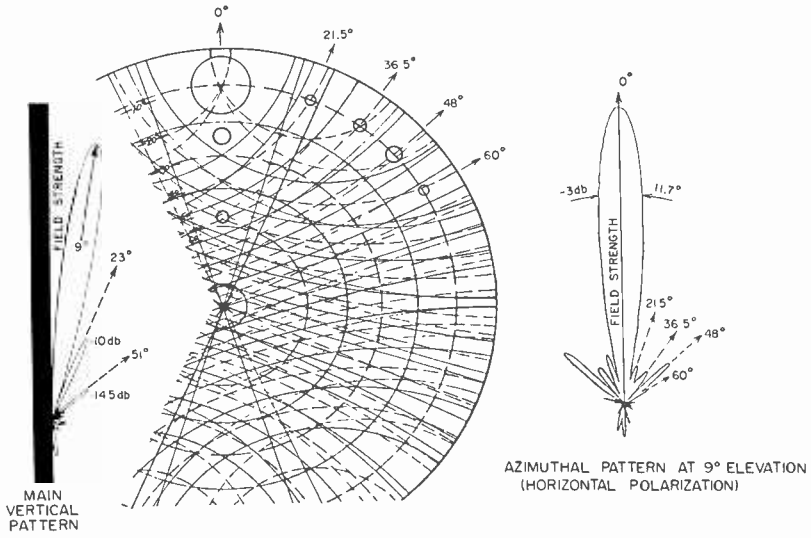

Fig. 2—Comparison of computed and measured radiation patterns for a double-rhomboid antenna.

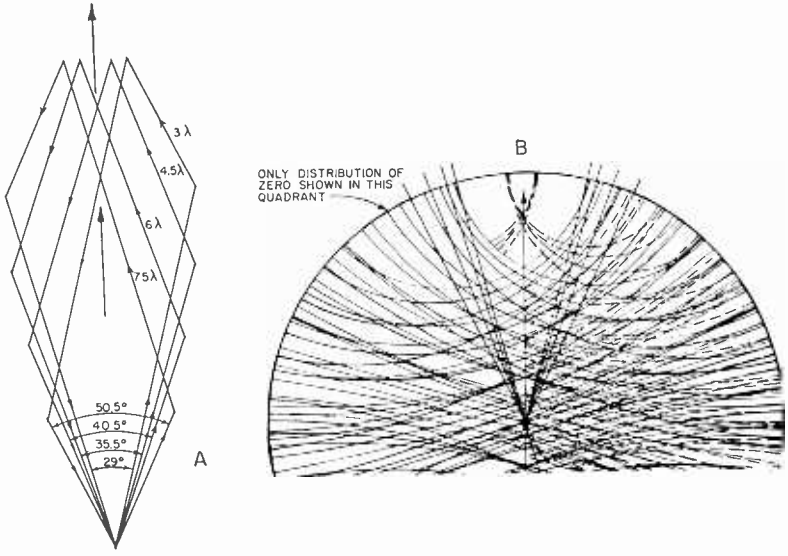

Fig. 3—Configuration and indicated radiation pattern for a quadruple-rhomboid antenna.

Figure 2 shows the measured and stereographically computed radiation pattern for a double-rhomboid antenna of the form shown in Figure 1. The 637-megacycle model used for this test had the following dimensions: $L_1 = 3.5\lambda$, $L_2 = 6.0\lambda$, $h = 1.53\lambda$, $X = 49$ degrees, and $Y = 36$ degrees. The measured vertical pattern at the left in Figure 2 is the field-strength distribution on the axis of the antenna. At the right is the azimuthal field-strength distribution at 9 degrees elevation through the beam maximum. The stereographic chart assembly used to compute this pattern is shown in the middle. Circles indicate the locations of main beam and sidelobes which correspond closely with the two measured patterns.[2,3] The sidelobe asymmetry in the azimuthal pattern was due to imperfect balun feeder balance, because reversal of feeder connections reversed the asymmetry. In this figure, the stereographic pattern shows the distributions of maxima for the four component sides as broken lines and their zero distributions as solid lines. The concentric broken and solid lines are the maxima and zeros in the height factor for the horizontally polarized field components given in stereographic coordinates. Note the coherence of four first maxima to form the main beam. The apex angles for the four wires emanating from the feed point are those appearing as straight radial lines from the centers of the individual charts.

Results

Figure 4 shows azimuthal patterns measured with a full size antenna having dimensions $L_1 = 3.5\lambda$, $L_2 = 6.0\lambda$, height $= 1.53\lambda$ at the design frequency of 8.5 megacycles, $X = 52.2$ degrees and $Y = 37.7$ degrees. The radiation patterns were measured using a transmitter in an optically tracked aircraft flying precision courses of 3.5 to 10 miles radius from the antenna. The measured vertical beam angles are included in Table I. The entire hemisphere was explored for other sidelobes that might be present in the surrounding space, but none were found that were larger than those shown. Field-strength measurements in aircraft at 10 miles and computations from the measured radiation horizontal and vertical patterns indicate a gain at 10 megacycles of about 27 decibels relative to a half-wave dipole.

Table II gives the comparison of signals received over a transatlantic path during five days in January 1959. The comparison is between a horizontal rhombic antenna, 0.68 wavelength above ground,

[2] For theory of stereographic representations of radiation patterns, see D. Roster, "Radiation from Rhombic Antennas," *Proc. I.R.E.*, Vol. 25, p. 1327, October, 1937.

[3] For construction and use of stereographic charts, see E. A. Laport, *Radio Antenna Engineering*, p. 315, New York, 1952.

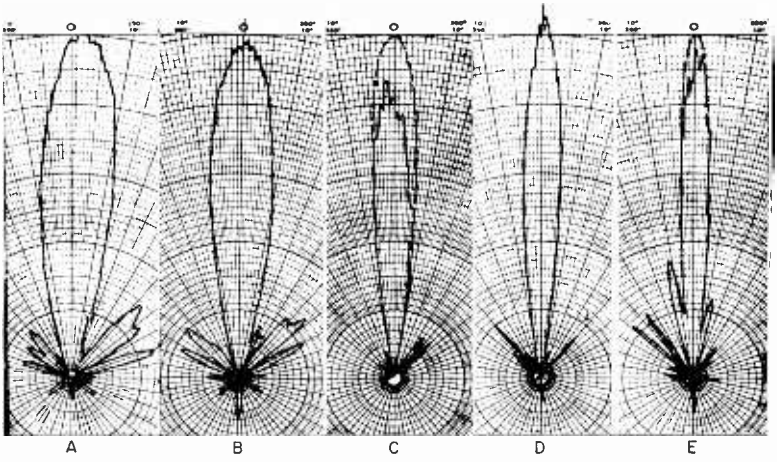

Fig. 4—Measured azimuthal field-strength distribution through the vertical angle of the main beam from 5 to 12 megacycles.

having side lengths of 2.94 wavelengths and the double-rhomboid antenna at the same station and oriented on the same path. Signals from simultaneous transmissions with equal antenna input powers on 9857 and 10,127 kilocycles were recorded. The highest and lowest receiver input voltages within each hour were analyzed to obtain the data given in Table II. On alternate days the frequencies were interchanged on the two antennas. Signal recordings continued each day until the frequency became unuseable.

Conclusion

The double-rhomboid antenna can be designed for a wide range

Table I—Data Relating to Figure 4

Pattern	Freq. kc	Flight Radius Miles	Flight Altitude Feet	Beam Angle Degrees	Vertical Beamwidth Degrees*	Horizontal Beamwidth Degrees*	L_1 λ	L_2 λ
A	4,990	3.5	5,000	15.5	...	16	3.53	2.05
B	5,991	10	9,500	10	...	14.5	4.23	2.47
C	8,145	4	3,000	8	6	11	5.75	3.35
D	10,150	10	7,000	7.5	5.5	8.5	7.42	4.32
E	12,000	5	3,000	6.5	5	7	8.47	4.93

* Half-power values.

of sizes to obtain variously desired beam widths, beam angles, and construction budgets. The principles can be applied to antennas for VHF and UHF where sidelobe suppression is important for interference reduction. Due to the natural sharpness of secondary lobes

Table II—Comparison of Simultaneous Signals Over High-Latitude Transatlantic Path of 3550 Statute Miles at 10 Megacycles.

Signal Level (dbμ)	Rhombic Antenna (Hours*)	Double-Rhomboid Antenna (Hours*)
< 5	9	1
<10	14	6
<20	17	8
<30	45	34
<40	55	43
>40	41	50
>50	26	36
>60	9	20
>70	1	2
Fading Range		
≤ 10	0	2
≤ 20	13	20
>20	40	38
>30	21	20
>40	8	7
>50	2	1
Total db/Hours Signal Above 1 μV (0 dbμ)		
	1934	2453

* Total hours tested is 60.

in the patterns of long straight wires, the apex angles of the antenna must be exact for best sidelobe suppression.

Acknowledgment

The contributions of Norman Diehm of the Wind Turbine Co. to our field and laboratory experimental programs are gratefully acknowledged.

APPENDIX

The following equations are convenient for establishing the angles of zeros and maxima in the radiation pattern for a single, long straight wire with a traveling-wave current distribution.

For the angle θ_{0m}, the m^{th} zero with respect to the conductor axis from 0 to 180 degrees,

$$\theta_{0m} = \text{haversine}^{-1}\left(\frac{m}{\frac{2L}{\lambda}}\right)$$

For the angles θ_{Mn} of the series of maxima of diminishing amplitude starting with the largest at θ_{M1} nearest to the forward axis of the wire,

$$\theta_{Mn} = \text{haversine}^{-1}\left(\frac{K}{\frac{2L}{\lambda}}\right)$$

where L is wire length in wavelengths (λ), and values of K are as shown in the following table:

n	1	2	3	4	5
K	0.371	1.466	2.480	3.486	4.495

For values of n greater than 5, $K \approx n - 0.5$.

Haversines (haversine $\theta \equiv (1 - \cos\theta)/2$) are tabulated in *Handbook of Chemistry and Physics** and in most navigation handbooks.

It is to be noted that the zero distributions are symmetrical in both quadrants for wires an integral number of half-wavelengths long. The distribution of maxima is not symmetrical.

With unity current in the wire, the relative field strength for a lobe maximum is

$$\frac{\sin\theta_{Mn}}{2\,\text{hav}\,\theta_{Mn}}$$

which is the envelope for all lobes.

In stereographic coordinates, the loci of maxima and zeros are all portions of circles centered on the line corresponding to the wire.

* Edited by C. D. Hodgeman, *Handbook of Chemistry and Physics*, Chemical Rubber Publishing Co., Cleveland, Ohio, 1959.

MEASUREMENT OF SEMICONDUCTOR PROPERTIES THROUGH MICROWAVE ABSORPTION*

By

R. D. Larrabee

RCA Laboratories,
Princeton, N.J.

Summary—A technique for utilizing microwave absorption as a probe for measuring semiconductor properties is described. The complete isolation between the microwave measuring circuit and the sample circuit make this technique useful for many applications. It is shown that this technique can be used to measure minority carrier lifetime (decay of conductivity) in a way which requires no physical electrical connection to the sample under test.

Introduction

THE possibility of utilizing the technique of microwave absorption as a probe for measuring semiconductor properties is of great interest, since this technique requires no direct electrical connection to the sample.[1-3] Consequently, complete isolation is possible between the circuit which perturbs the electrical properties of a sample and the microwave circuit which senses the resulting changes in these properties. It is possible, for example, to inject pulses of minority carriers either optically or through suitable contacts and to use the microwave technique to measure their lifetime (decay of conductivity).[3] The price paid for this isolation is the complexity of the microwave interaction with the sample. In general, it is necessary to calibrate the equipment to determine its characteristics (which are generally nonlinear) before quantitative data can be taken. The skin effect will generally limit the usefulness of the technique so that only thin wafer samples can be used. It is concluded, therefore, that microwave absorption provides a useful but limited technique for the study of semiconductor properties.

---

* Manuscript received July 22, 1959.

[1] A. F. Gibson and J. W. Granville, "The Measurement of Drift Modility in Germanium at High Electric Fields," *Jour. Electron.*, Vol. 2, p. 259, March, 1956.

[2] J. B. Arthur, A. F. Gibson, and J. W. Granville, "The Effect of High Electric Fields on the Absorption of Germanium at Microwave Frequencies," *Journal of Electronics*, Vol. 2, p. 145, September, 1956.

[3] A. P. Ramsa, H. Jacobs, and F. B. Brand, "Microwave Techniques in Measurement of Lifetime in Germanium," *Jour. Appl. Phys.*, Vol. 30, p. 1054, July, 1959.

Experimental Apparatus

A block diagram of a simple microwave line suitable for studying semiconductor properties is shown in Figure 1. It consists of the following components:

(a) A reflex klystron (11,000-17,000 megacycles) and associated power supply capable of delivering milliwatts of r-f power into a Ku-band (12,000-18,000 megacycles) waveguide.

(b) An isolator which absorbs all reflected power so that there will be no changes in the klystron output with varying loads.

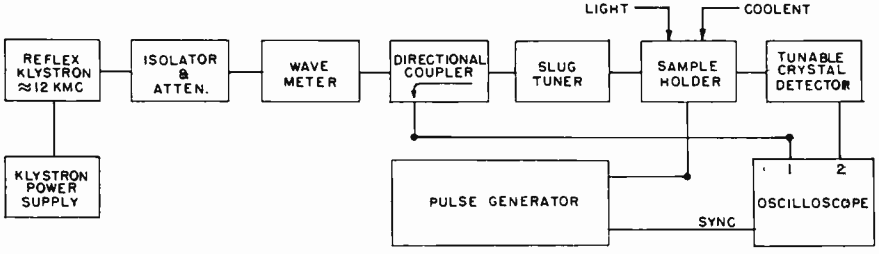

Fig. 1—Block diagram of microwave measuring circuit.

(c) An attenuator to control the r-f power level.

(d) A wavemeter to measure operating frequency.

(e) A directional coupler to sense the total amount of r-f power reflected from all the subsequent apparatus.

(f) A "slug tuner" to introduce a controllable reactive discontinuity into the line for the purpose of tuning out reflections from the sample.

(g) A sample holder.

(h) A tunable crystal detector to detect the r-f power transmitted through the sample.

The output of the directional coupler is rectified by a crystal and applied to an oscilloscope along with the output of the main tunable crystal detector. The oscilloscope, therefore, can measure either the transmitted or reflected power levels. The semiconductor sample is mounted in a waveguide holder in a manner such that it can be supplied with light, controlled atmosphere, coolant, and electrical signals, any or all of which will change its electrical properties. These changes in

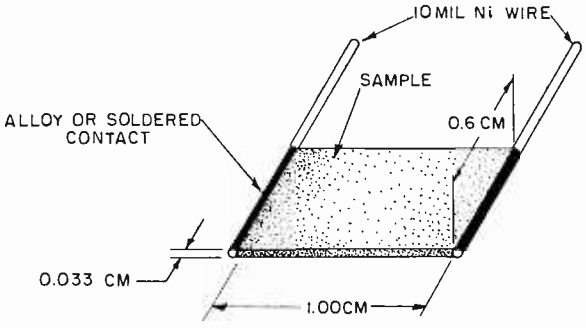

Fig. 2—Sample used in microwave measurements.

electrical properties will cause changes in the transmitted and/or reflected power which, in turn, are observed on the oscilloscope.

Sample holders are easily made for holding almost any reasonable size and shape wafers in the waveguide in a variety of orientations. It was found convenient to standardize on the type of sample shown in Figure 2. This sample is large enough to have adequate microwave–sample interaction, thin enough to minimize skin effect for 20 ohm-centimeter material and above, and is generally quite suitable for study. Such a sample mounted in a sample holder is shown schematically in Figure 3. It is placed in the waveguide so that it is in the microwave-electric-field maximum in the center of the guide for maximum interaction. It is generally advisable to have any applied electric

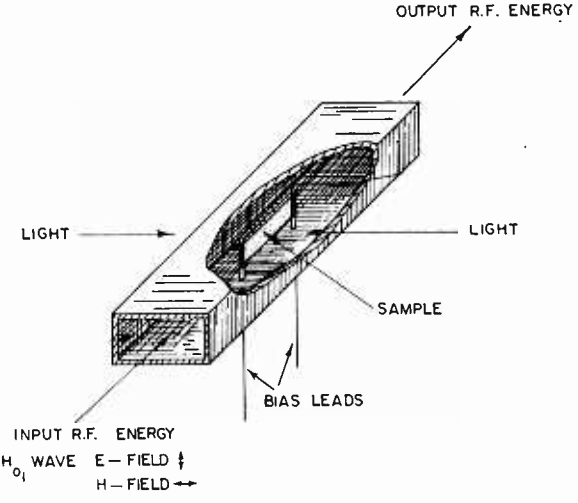

Fig. 3—Schematic drawing of sample holder.

fields (bias field) perpendicular to the microwave electric field as indicated in Figure 3. In this way, the r-f "views" the sample in the most homogeneous fashion. The bias leads that protrude through the waveguide wall are by-passed to the wall by small high-voltage capacitors built into the wall structure. These capacitors are necessary to avoid loss of r-f power through radiation from the bias lead wires.

In addition to the features discussed above, it was found desirable to be able to immerse the sample and sample holder in a coolant such as liquid nitrogen; to provide for illumination of the large flat surfaces of the sample; and to provide for the passage of a vapor over the sample for varying the surface condition.

Basic Results

At low conductivities, the r-f absorption of a sample of the type discussed above is proportional to the conductivity. At the higher conductivities, however, the skin effect becomes important in preventing penetration of r-f into the sample bulk. Consequently, as the sample conductivity is increased, a maximum r-f absorption is reached followed by a slow decrease with increasing conductivity. It has been observed experimentally that a practical limit of the linear conductivity–absorption relationship is reached when the

$$P_{\text{crit}} = \tau^2 f \times 10^{-5},$$

where P_{crit} is the lowest value of resistivity (ohm-cm) for which one can consider absorption proportional to conductivity, τ is the thickness of the sample in mils, and f is the frequency of operation in megacycles. For a frequency of 12,000 megacycles, and a thickness of 0.033 centimeter, $P_{\text{crit}} \approx 20$ ohm-centimeters. This does not mean that measurements with $P < P_{\text{crit}}$ are not possible, but just that the simple linear relationship between absorption and conductivity is lost.

Measurement of Lifetime

A very simple measurement with this technique is that of minority-carrier lifetime. Minority carriers are injected into the sample either by use of suitable contacts or by optical means. The optical method of injection has the advantage that it permits measurement without any contacts whatsoever.[3] If the resistivity during injection never falls below P_{crit}, a simple exponential decay is noted in the microwave transmitted power after the injection is terminated. If the injection is so heavy as to make the resistivity lower than P_{crit}, a more complex

decay curve is observed. Since the lifetime measured by the above technique can be influenced by minority-carrier traps, it may be necessary to illuminate the sample with strong infrared (below band gap) radiation during the experiment to keep the traps empty. Since thin wafer samples are used, this method affords a very convenient way of measuring surface recombination velocity.

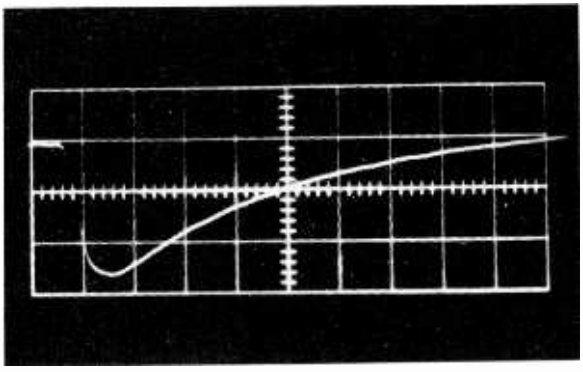

Fig. 4—Illustration of actual lifetime measurement in 30-ohm-centimeter p-type germanium at room temperature. Time scale = 10 microseconds for each of the large divisions on the abscissa; ordinate scale = r-f transmitted power level in arbitrary units. Minority carrier injection is achieved through application of 10-microsecond pulse of bias field through suitable contacts. Notice the decay of r-f power during injection and the exponential approach to equilibrium after termination of the pulse.

Lifetimes varying from one to several hundred microseconds have been observed in many germanium samples in which injection was accomplished by use of suitable contacts (see Figure 4). Not only are these results reproducible in time and from sample to sample, but they also agree quite well with the values measured by the conventional decay of photoconductivity method.

The apparent lifetime of electrons in unilluminated p-type indium antimonide at 77°K was observed to be 10^{-7} second. In practice, the limit of lifetimes observable by this technique is set by the rise time of the oscilloscope (and/or possibly the microwave crystal detector). In the present experiment, a Tetronix 545 oscilloscope with a rise time of about 20 millimicroseconds was used. The limitation was confirmed when an attempt was made to measure the lifetime of gallium arsenide and a value of 20 millimicroseconds was obtained.

Conclusion

A microwave absorption technique has been demonstrated which measures changes in the conductivity of a semiconductor wafer in a

manner which requires no physical contact with the sample. It is felt that this technique is particularly useful in applications such as minority-carrier lifetime measurements in comparatively high-resistivity materials such as germanium and silicon, where lack of contacts or electrical isolation are important considerations.

The possibility of utilizing these techniques to study surface effects and traps is immediately evident. Surface recombination velocity as a function of surface treatment has been measured in this manner.

ACKNOWLEDGMENT

The author is indebted to J. A. Amick, J. J. Thomas, R. A. Braden, E. O. Johnson, M. C. Steele and R. C. Duncan, Jr. for their help in this experiment.

APPLICATION OF THE SAMPLING FUNCTION TO CIRCUIT ANALYSIS OF MODULATORS AND DEMODULATORS USING DIODES.*

BY

A. FELLER

Industrial Electronic Products,
Camden, N. J.

Summary—*In the past, the sampling wave has been used to analyze ideal switching circuits and switching modulator circuits.*[1] *This paper presents a logical extension of this concept to circuits such as frequency converters and mixers where the finite values of the forward and reverse resistances of diodes are taken into consideration.*

THEORY

ANY CIRCUIT with output frequencies not found in its input possesses some degree of nonlinearity.[2] Modulators and demodulators fall into this category. If these circuits are operated under certain conditions, however, they may be regarded as linear systems insofar as the intelligence signals are concerned. Because of this fact, certain simplifying but realistic assumptions can be made which permit linear analysis of these circuits. The sampling wave (square wave) serves as the basic tool for this analysis.

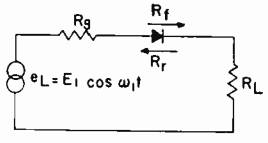

Fig. 1—Simple diode circuit.

Consider the simple diode circuit shown in Figure 1. The static characteristics of the diode are assumed to be as shown in Figure 2. The two slopes R_f and R_r correspond to the forward and reverse resistances, respectively. For a diode with this characteristic, the output

* Manuscript received September 23, 1959.

[1] R. S. Caruthers. "Copper Oxide Modulators in Carrier Telephone Systems," *Bell Sys. Tech. Jour.*, Vol. 18, April, 1939.

[2] E. W. Herold, "Operations of Frequency Converters and Mixers for Super Heterodyne Reception," *Proc. I.R.E.*, Vol. 30, p. 84, February, 1942.

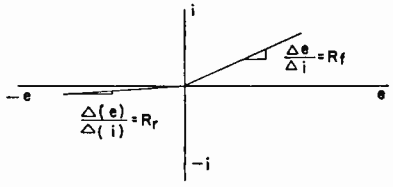

Fig. 2—Diode characteristics showing forward and reverse resistance.

voltage e_L for a cosinusoidal input as indicated in Figure 1 is

$$e_L = \frac{R_L E_1 \cos \omega_1 t}{R_L + R_f + R_g} \qquad -\frac{\pi}{2} < \omega_1 t < \frac{\pi}{2},$$
$$e_L = \frac{R_L E_1 \cos \omega_1 t}{R_L + R_r + R_g} \qquad \frac{\pi}{2} < \omega_1 t < \frac{3}{2}\pi. \tag{1}$$

By definition $R_r \geqslant R_f$; therefore, the waveform e_L will be as shown in Figure 3. F is the transfer function of the circuit when the resistance of the diode is R_f, and B is the transfer function of the circuit when the resistance of the diode is R_r.

The Fourier series for this non-sinusoidal function could be calculated directly by integration. However, an alternate method is available. Consider, initially, that B in Figure 3 is zero, i.e., $R_r = \infty$. In this special case, the output waveform becomes simply a half-wave rectified cosine wave. This waveform can be obtained directly by use of the square wave. Let

$$e_1 = FE_1 \cos \omega_1 t$$

and

$$e_2 = \frac{2}{\pi}\left(\frac{\pi}{4} + \cos \omega_1 t - \frac{1}{3}\cos 3\omega_1 t + \frac{1}{5}\cos 5\omega_1 t + \cdots\right)$$

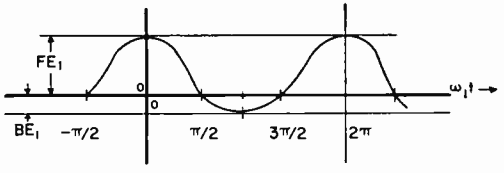

Fig. 3—Output voltage of circuit in Figure 1.

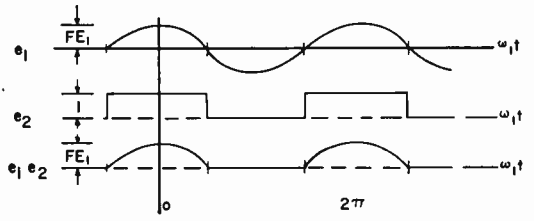

Fig. 4—Multiplication of square wave and cosine wave to produce a half-wave rectified cosine wave.

$$= \frac{2}{\pi}\left[\frac{\pi}{4} + \sum_{n=1}^{\infty} \frac{(-1)^{n+1}}{2n-1} \cos\,(2n-1)\,\omega_1 t\right]$$

e_2 is a square wave whose average value is ½. The product $e_1 e_2$ is shown in Figure 4; it is a rectified cosine wave of amplitude FE_1.

$$e_1 e_2 = (FE_1 \cos \omega_1 t)\,\frac{2}{\pi}\left(\frac{\pi}{4} + \cos \omega_1 t - \frac{1}{3}\cos 3\omega_1 t + \frac{1}{5}\cos 5\omega_1 t + \cdots\right)$$

$$= \frac{FE_1}{\pi}\left(1 + \frac{\pi}{2}\cos \omega_1 t + \frac{2}{3}\cos 2\omega_1 t - \frac{2}{15}\cos 4\omega_1 t + \cdots\right) \qquad (2)$$

$$= \frac{FE_1}{\pi}\left(1 + \frac{\pi}{2}\cos \omega_1 t + 2\sum_{n=1}^{\infty} (-1)^{n+1}\frac{\cos 2n\omega_1 t}{4n^2-1}\right)$$

In Figure 5, the waveform of Figure 3 is shown as a composite of two waveforms. Thus, the non-sinusoidal function of Figure 3 can be expressed as an ideal half-wave rectified cosine wave of amplitude $(F-B)E_1$ plus a cosine function of amplitude BE_1. Therefore, the output voltage of Figure 1, which has the waveform of Figure 3, can be written directly as

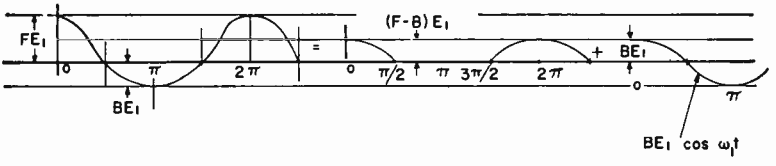

Fig. 5—Non-sinusoidal wave of Figure 3 shown as sum of nonlinear and linear terms.

$$e_L = BE_1 \cos \omega_1 t + \frac{(F-B)E_1}{\pi}$$
$$\left(1 + \frac{\pi}{2}\cos \omega_1 t + \frac{2}{3}\cos 2\omega_1 t - \frac{2}{15}\cos 4\omega_1 t + - - -\right)$$
$$= E_1 \left\{\frac{F+B}{2}\cos \omega_1 t + \left(\frac{F-B}{\pi}\right)\right.$$
$$\left.\left(1 + \frac{2}{3}\cos 2\omega_1 t - \frac{2}{15}\cos 4\omega_1 t + - - -\right)\right\}$$
$$= E_1 \left\{\frac{F+B}{2}\cos \omega_1 t + \left(\frac{F-B}{\pi}\right)\right.$$
$$\left.\left(1 + 2\sum_{n=1}^{\infty} (-1)^{n+1}\frac{\cos 2n\omega_1 t}{4n^2-1}\right)\right\} \qquad (3)$$

Since $R_f \leqq R_r \leqq \infty$, it follows that $0 \leqq B \leqq F$. It is of interest to examine Equation (3) at the limiting values of B:

Case 1: $B = 0$

$$e_L = \frac{FE_1}{\pi}\left(1 + \frac{\pi}{2}\cos \omega_1 t + \frac{2}{3}\cos 2\omega_1 t - \frac{2}{15}\cos 4\omega_1 t + - - -\right)$$
$$= \frac{FE_1}{\pi}\left(1 + \frac{\pi}{2}\cos \omega_1 t + 2\sum_{n=1}^{\infty} (-1)^{n+1}\frac{\cos 2n\omega_1 t}{4n^2-1}\right), \qquad (3a)$$

which is the ideal half-wave rectified cosine wave.

Case 2: $B = F$

$$e_L = FE_1 \cos \omega_1 t. \qquad (3b)$$

This is apparent from Figure 1. When $B = F$, $R_r = R_f$ and the diode becomes an ordinary resistor.

Thus, the ratio F/B can be used to specify all degrees of rectification. Therefore, Equations (3a) and (3b) could have been written directly by multiplying the original cosine input function by a properly chosen square wave.

This is done diagrammatically in Figure 6:

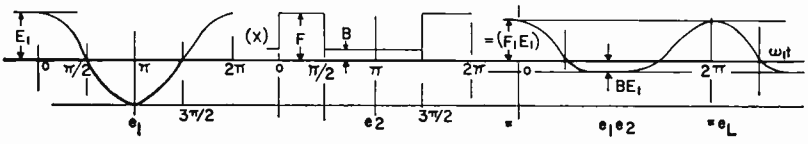

Fig. 6—Multiplication of square wave and cosine wave to produce output voltage of Figure 3.

$$e_L = E_1 \cos \omega_1 t \left[B + \frac{2}{\pi} (F - B) \left(\frac{\pi}{4} + \cos \omega_1 t - \frac{1}{3} \cos 3\omega_1 t + \frac{1}{5} \cos 5\omega_1 t + \cdots \right) \right]$$

which yields the same results as Equation (3).

In general, for an input e_{in},

$$e_L = e_{in} \left\{ B + \frac{2}{\pi} (F - B) \left(\frac{\pi}{4} + \sum_{n=1}^{\infty} \frac{(-1)^{n+1}}{2n-1} \cos (2n-1)\omega_1 t \right) \right\} \quad (4)$$

Thus it has been shown that the action of a diode under certain conditions may be simulated by a square-wave modulation. The finite forward and reverse resistances of the diode may be taken into consideration by proper choice of the average value of the square wave.

Modulators and Demodulation

This theory will now be applied to a circuit which is typical of the type used in modulator and demodulator applications where diodes are the nonlinear circuit elements.

Consider the circuit of Figure 7; here $e_1 = E_1 \cos \omega_1 t$ and $e_2 = E_2 \cos \omega_2 t$. If we make $E_1 \gg E_2$, then the operating point of the diode,

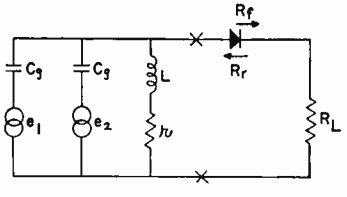

Fig. 7—Basic modulator or demodulator circuit.

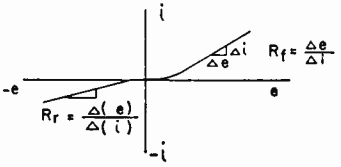

Fig. 8—Diode characteristics showing forward and reverse resistance.

will be determined by E_1. If E_1 is of the proper magnitude, the operating point will be on that part of the diode characteristic curve where both the forward resistance, R_f, and the reverse resistance, R_r, are effectively constant. This is illustrated in Figure 8.

As long as the magnitude of E_2 is such that the variations of the operating point remain on that portion of the diode characteristics where R_f and R_r remain constant, the circuit can be made to act as a reasonably linear modulator or demodulator. Since it is required that R_f and R_r remain constant over the operating range, the modulator or demodulated output is independent of E_1.

Looking toward the generators at the terminals x-x in Figure 7, the system is linear. Hence, superposition can be employed to calculate a Thevenin equivalent circuit, as shown in Figure 9.

In the equivalent circuit of Figure 9,

$$Z_{eq_n} = \left(\frac{r + j\omega L}{1 - \omega^2 LC + j\omega rC} \right)_{\omega=\omega_n},$$

$$C_n = \frac{1}{2} \left(\frac{-\omega^2 LC + j\omega rC}{1 - \omega^2 LC + j\omega rC} \right)_{\omega=\omega_n},$$

Let

$$F_n = \frac{R_L}{R_L + R_f + Z_{eq_n}}, \tag{5}$$

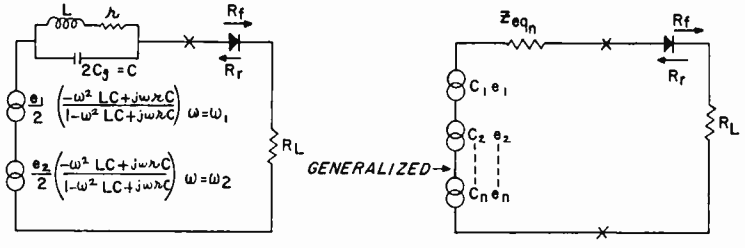

Fig. 9—Thevenin equivalent circuit of Figure 7.

$$B_n = \frac{R_L}{R_L + R_r + Z_{\omega_n}}, \tag{6}$$

where the subscript n indicates the radian frequency at which Z_{ω_1} is evaluated.

In the following equations, the phase information has been neglected. As long as the operating conditions originally specified are maintained, the errors introduced into the frequency spectrum of the output signal and into the amplitude of the desired frequencies will be of a second-order effect. This follows for the same reason that an approximate linear analysis of an essentially nonlinear circuit is possible, i.e., although the action of the circuit is nonlinear with regard to the signal which determines the diode operating point, the circuit is essentially linear with regard to the information-carrying signal.

The output voltage $e_L(t)$ (for the generalized-input circuit of Figure 9) can now be written directly with the aid of Equation (4).

$$e_L = B_1C_1e_1 + \cdots B_nC_ne_n + \frac{2}{\pi}\left\{ (C_1e_1)(F_1 - B_1) + \cdots (C_ne_n)(F_n - B_n) \right\} \left[\frac{\pi}{4} + \sum_{n=1}^{\infty} \frac{(-1)^{n+1}}{2n-1} \cos (2n-1)\omega_1 t \right] \tag{7}$$

$$e_L = \left\{ B_1C_1 + \frac{1}{2}(F_1 - B_1)C_1 \right\} E_1 \cos \omega_1 t + \cdots \left\{ \frac{B_nC_n}{2} + \frac{F_nC_n}{2} \right\} E_n \cos \omega_n t$$

$$+ \frac{2E_1}{\pi}\left\{ (F_1 - B_1)(C_1) \right\}\left\{ \frac{1}{2} + \frac{2}{3}\cos 2\omega_1 t - \frac{1}{6}\cos 4\omega_1 t + \cdots \right\} + \cdots$$

$$+ \frac{2E_n}{\pi}\left\{ (F_n - B_n)C_n \right\}\left\{ \frac{1}{2}\cos (\omega_1 + \omega_n)t + \frac{1}{2}\cos (\omega_1 - \omega_n)t \right.$$

$$\left. - \frac{1}{6}\cos (3\omega_1 + \omega_n)t - \frac{1}{6}\cos (3\omega_1 - \omega_n)t + \cdots \right\} \tag{8}$$

Equation (8) is a general solution for the circuit of Figure 7, whether it is used as a modulator or demodulator, so long as E_1 is sufficiently greater than E_n that E_1 is the primary voltage determining the operating point of the diode.

Incidentally, the curvature of the diode characteristic at extremely low levels has played no direct part in the calculation thus far. How-

ever, the curvature does affect the values of R_f and R_r of the diode. Since R_f and R_r are included in the results, no additional error is introduced.

Heterodyne Demodulation

An obvious advantage of Equation (8) is that it permits the desired frequency outputs to be extracted immediately. For example, suppose the circuit of Figure 7 is a continuous-wave demodulator. The desired output is then a signal whose frequency will be $\omega_1 - \omega_2$. Presumably, this is an audio signal which will be coupled to an audio amplifier. Only the last term is capable of producing a $\omega_1 - \omega_2$ signal. The desired difference-frequency signal is:

$$e_L = \frac{1}{\pi} (F_2 - B_2) C_2 E_2 \cos (\omega_1 - \omega_2) t. \tag{9}$$

Note the E_1 does not appear in Equation (9). This is a direct result of the assumption that $E_1 \gg E_2$. Varying E_1 will not affect $e_L(\omega_1 - \omega_2)t$ only as long as R_f and R_r remain constant. Note also that $e_L(\omega_1 - \omega_2)t$ varies directly with E_2; thus, the output voltage is a linear function of the input voltage.

In terms of the parameters of the network in Figure 7, Equation (9) becomes

$$e_L(\omega_1 - \omega_2)t = \frac{E_2}{2\pi} \left\{ \left| \frac{R_L(1 - \omega^2 LC + P_2 rc)}{(R_L + R_f)(1 - \omega_2^2 LC + P_2 rc) + r + P_2 L} \right| - \left| \frac{R_L(1 - \omega_2^2 LC + P_2 rc)}{(R_L + R_f)(1 - \omega_2^2 LC + P_2 rc) + r + P_2 L} \right| \right\} \left\{ \left| \frac{-\omega_2^2 LC + P_2 rc}{1 - \omega_2^2 LC + P_2 rc} \right| \right\} \cos (\omega_1 - \omega_2) t \tag{10}$$

where $P_2 = j\omega_2$.

Although no mention has been made of the other frequencies specified by Equations (7) and (8), they too will appear across the load R_L. However, the next higher frequency of significant amplitude appearing across the load will be ω_1. Therefore, a simple low-pass filter connected to R_L will allow only the d-c component and the desired $(\omega_1 - \omega_2)$ signal to pass.

Amplitude Modulator

As a second example, suppose the network in Figure 7 is a modulator. $e_1 = E_1 \cos \omega_1 t$ will now be considered the frequency which is to be modulated. Consider $e_2 = E_2 \cos \omega_2 t$ as the modulating frequency.

From Equations (7) and (8), those frequencies containing ω_1, $\omega_1 + \omega_2$, and $\omega_1 - \omega_2$ constitute the modulated wave. If all other frequencies are disregarded, the voltage across the load R_L becomes

$$e_L = B_1 C_1 E_1 \cos \omega_1 t + \frac{1}{2} (F_1 - B_1) C_1 E_1 \cos \omega_1 t + \frac{1}{\pi} (F_2 - B_2) C_2 E_2 \cos (\omega_1 + \omega_2) t + \frac{1}{\pi} (F_2 - B_2) C_2 E_2 \cos (\omega_1 - \omega_2) t \tag{11}$$

$$e_L = \left\{ \frac{B_1 + F_1}{2} \right\} C_1 E_1 \cos \omega_1 t + \frac{1}{\pi} (F_2 - B_2) C_2 E_2 \cos (\omega_1 \pm \omega_2) \text{ t.} \tag{12}$$

The first and second terms of Equation (11) both contribute to the carrier level. The first term represents a direct contribution to the carrier level by the linear component of the circuit, while the second term is the contribution of the nonlinear component to the carrier level, i.e., an ideal diode-rectification process.

Equation (12) now contains quantitative information as to the variation of per-cent modulation and power distribution of the modulated signal with finite forward and reverse resistance of the diode.

Frequency Converter

As a third example of the application of Equation (7), consider the case in which $e_1 = E_1 \cos \omega_1 t$ is the local oscillator signal in Figure 7. e_2 will be a symmetrical amplitude-modulated input signal

$$e_2 = E_2 (1 + k \cos \omega_m t) \omega_2 t$$

where $k = E_m / E_2$.

If the circuit of Figure 7 is to serve as a first detector in a superheterodyne receiver, that is, a frequency converter, the desirable output terms may be selected from Equation (8);

$$\frac{2E_2}{\pi 2}\{(F_2 - B_2)(C_2)\}\cos(\omega_1 - \omega_2)\,t.$$

Substituting $E_2(1 + k\cos\omega_m t)$ for E_2 since this is now the magnitude of the $\omega_2 t$ term, and the subscript n for the subscript 2,*

$$e_L = \frac{2E_2(1 + k\cos\omega_m t)}{2\pi}\{(F_n - B_n)C_n\}\cos(\omega_1 - \omega_2)\,t$$

$$= \frac{E_2}{\pi}\{(F_n - B_n)C_n\}\cos(\omega_1 - \omega_2)\,t$$

$$+ \frac{kE_2}{2\pi}\{(F_n - B_n)C_n\}\cos(\omega_1 - \omega_2 \pm \omega_m)\,t. \qquad (13)$$

It has been assumed that the load impedance of Figure 7 is a selective, though broadbanded, circuit whose input impedance is essentially constant and resistive for the difference frequency term $(\omega_1 - \omega_2)$ and its sidebands $(\omega_1 - \omega_2 \pm \omega_m)$. This implies that the time constant of the load circuit will be such that although it can follow variations of the $\omega_1 - \omega_2 \pm \omega_m$ envelope, it cannot follow variations of ω_1 or ω_2. If the modulation is less than 30 per cent, then all the assumptions made earlier remain valid.

The quantities F_n, B_n, and C_n become very important in receivers where wideband signals are to be received. If each of these quantities are not constant for the difference frequency and its sidebands, amplitude distortion of the modulating signal will be introduced. This means, of course, that in wideband receivers, such as television receivers, the source impedance of the frequency converter looking into the difference frequency load must be relatively flat over the frequency range from $\omega_1 - \omega_2 - \omega_{m\,\max}$ to $\omega_1 - \omega_2 + \omega_{m\,\max}$ where $\omega_{m\,\max}$ is the highest desirable modulating frequency.

In addition, if the relative phase shift between the sidebands and the difference frequency carrier $\omega_1 - \omega_2$ must be maintained linear, as is the case in color-television receivers, the phase characteristics of F_n, B_n, and C_n must be considered when the circuitry of the converter is being designed.

---

* Since more than one frequency is involved in this expression the subscript n is used to specify the exact frequency at which the quantities F and B are to be evaluated. In other words, n implies the evaluation of F and B at $\omega_1 - \omega_2$, $\omega_1 - \omega_2 + \omega_m$ and $\omega_1 - \omega_2 - \omega_m$ for all values of m.

Synchronous Detector

Let the local oscillator signal in Figure 7 be $e_1 = E_1 \cos \omega_1 t$ and let e_2 be the incoming double-sideband amplitude-modulated signal;

$$e_2 = E_2 (1 + k \cos \omega_m t) \cos \omega_1 t.$$

Note that the carrier frequencies of the incoming signal and local oscillator are equal. Substitution of the above value of e_2 in the last series of terms in Equation (8) gives

$$\frac{2}{\pi} (F_2 - B_2) C_2 E_2 (1 + k \cos \omega_m t) \cos \omega_1 t \left[\frac{\pi}{4} + \sum_{n=1}^{\infty} \frac{(-1)^{n+1}}{2n-1} \cos (2n-1) \omega_1 t \right] =$$

$$\frac{2}{\pi} (F_n - B_n) C_n E_2 \frac{\pi}{4} \cos \omega_1 t + \frac{2}{\pi} \left((F_n - B_n) C_n E_2 k \right) \left(\frac{1}{2} \cos \omega_m t + \frac{1}{4} \cos (2\omega_1 \pm \omega_m) t + \text{---} \right)$$

Assuming that R_L represents approximately the input impedance of a low-pass filter in the frequency range from 0 to $\omega_{m\,\max}$, the output voltage will be

$$e_L = \frac{E_1}{\pi} \{ (F_1 - B_1) C_1 \} + \frac{k E_2}{\pi} \left((F_n - B_n) C_n \right) \cos \omega_m t, \qquad (14)$$

where F_n, B_n, and C_n are evaluated at $\omega_1 + \omega_m$, the incoming sideband frequencies. Again, note that if these coefficients do not have a relatively constant impedance level between $\omega_1 - \omega_{m\,\max} \leq \omega_1 \leq \omega_1 + \omega_{m\,\max}$, amplitude distortion will exist in the output signal.

If the incoming modulated signal is a non-symmetrically modulated one, the same type of analysis can be used except that the phase considerations must be included. The analysis will show that the output voltage will be the same as in Equation (14) if the two carriers are synchronized in phase as well as in frequency.

Envelope Detection

In this case, remove the branch in Figure 7 containing e_2. Let $e_1 = E_1 (1 + k \cos \omega_m t) \cos \omega_1 t$ be the incoming amplitude-modulated

signal. Assuming, as before, a large carrier amplitude, and, in addition, limiting the modulation to less than approximately 20 to 25 per cent, we may determine the output voltage from Equation (7).

If R_L is a pure resistance,

$$e_L = B_1 C_1 E_1 \cos \omega_1 t + \frac{1}{2} B_n C_n E_n k \cos (\omega_1 + \omega_m) t + \frac{2}{\pi} (F_n - B_n) C_n E_1 (1 + k \cos \omega_m t) \left(\frac{\pi}{4} + \sum_{n=1}^{\infty} \frac{(-1)^{n+1}}{2n-1} \cos (2n-1) \omega_1 t \right) \tag{15}$$

$$e_L(t) = B_1 C_1 E_1 \cos \omega_1 t + \frac{1}{2} k B_n C_n E_1 \cos (\omega_1 \pm \omega_m) t + \frac{2}{\pi} (F_n - B_n) C_n \left\{ E_1 \frac{\pi}{4} \cos \omega_1 t + \frac{k\pi}{8} E_1 \cos (\omega_1 \pm \omega_m) t + \frac{E_1}{2} + \frac{E_1}{2} \cos 2\omega_1 t + \frac{k E_1}{2} \cos \omega_m t + \frac{k E_1}{4} \cos (2\omega_1 \pm \omega_m) t + \cdots \right\} . \tag{16}$$

If R_L represents approximately the input impedance of a low-pass filter over the frequency range $0 < \omega_m < \omega_{m\,\max}$, then $e_L(t)$ becomes

$$e_L = \frac{E_1}{\pi} (F_1 - B_1) C_1 + \frac{k E_1}{\pi} (F_n - B_n) C_n \cos \omega_m t. \tag{17}$$

A comparison of Equations (14) and (17) shows that for a given per cent of modulation, the envelope detector yields a modulating component identical to the modulating-component output of the synchronous detector.

Conclusion

In general, the technique of representing the action of the diode by a sampling function with an appropriate d-c average can be applied to circuits where one signal, by its amplitude, determines the operating characteristics of the diode, i.e., the front-to-back ratio of the diode. Although the analysis in this paper covered only those conditions where the diode conducted approximately 180 degrees, the same approach could be applied to diodes whose conduction angle is different from 180 degrees. This is accomplished simply by choosing the duty cycle of the sampling function to be proportional to the conduction angle. Thus, biased diodes can be handled with almost the same ease as unbiased ones.

RCA TECHNICAL PAPERS†

Fourth Quarter, 1959

Any request for copies of papers listed herein should be addressed to the publication to which credited.

"Atlantic Missile Range Cine Processing Laboratory," W. F. Bischof, *Jour. S.M.P.T.E.* (October) 1959

"Comments on 'Some Notes on Strip Transmission Line and Waveguide Multiplexers'," R. M. Kurzrok, *Trans. I.R.E. PGMTT* (October) (Correspondence) 1959

"Design Calculations for UHF Ferrite Circulators," H. Boyet, S. Weisbaum, and I. Gerst, *Trans. I.R.E. PGMTT* (October) (Correspondence) 1959

"Hall Effect in High Electric Fields," M. Glicksman and M. C. Steele, *Proc. I.R.E.* (October) (Letter to the Editor) 1959

"Theory and Application of a Minority Carrier Sweep-Out Effect," R. D. Larrabee, *Jour. Appl. Phys.* (October) 1959

"Thermoelectric Properties of Some Mixed Oxides," H. Lessoff, Y. Kersey, and R. A. Horne, *Jour. Chem. Phys.* (October) (Letter to the Editor) 1959

"Transistorized Preamplifier Design," H. J. Paz, *Electronic Industries* (October) 1959

"Two-Carrier Space-Charge-Limited Current in a Trap-Free Insulator," R. H. Parmenter and W. Ruppel, *Jour. Appl. Phys.* (October) 1959

"A Unified Analysis of Range Performance of CW, Pulse, and Pulse Doppler Radar," J. J. Bussgang, P. Nesbeda, and H. Safran, *Proc. I.R.E.* (October) 1959

"Why Man in Space?," G. R. Arthur, *Automatic Control* (October) .. 1959

"Switching Mechanism in Triglycine Sulfate and Other Ferroelectrics," E. Fatuzzo and W. J. Merz, *Phys. Rev.* (October 1) ... 1959

"Theoretical Model for Tetragonal-to-Cubic Phase Transformations in Transition Metal Spinels," P. J. Wojtowicz, *Phys. Rev.* (October 1) 1959

"Tube Parts Welded Semiautomatically," J. F. Stewart, *Electronics* (October 9) 1959

"High-Field Effect in Boron-Doped Silicon," R. D. Larrabee, *Phys. Rev.* (October 15) 1959

"New Parallel Photoelectromagnetic Effect," A. Amith, *Phys. Rev.* (October 15) 1959

"Considerations in Planning Sound Systems for Department Stores and Other Indoor Areas," A. K. Ward, *Wire and Radio Communications* (November) 1959

"The C-Stellarator, a New Research Tool for Hydrogen-Fusion Control Studies," L. B. Headrick, *Yale Scientific Magazine* (November) 1959

"Ferroelectric Behavior of Thiourea," G. J. Goldsmith and J. G. White, *Jour. Chem. Phys.* (November) 1959

"Infrared Studies of Birefringence in Silicon," S. R. Lederhandler, *Jour. Appl. Phys.* (November) 1959

"Jersey Engineers Steer Students Toward Science," R. E. Brown, *IRE Newsletter* (November) 1959

"Medical Electronics Center — Interdisciplinary Coordination," V. K. Zworykin, *Proc. I.R.E.* (November) 1959

"Scanning Microscopy in Medicine and Biology," L. E. Flory, *Proc. I.R.E.* (November) 1959
"7-Transistor Pocket Radio," H. Wittlinger, *Radio-Electronics* (November) 1959
"Temperature Dependence and Lifetime in Semiconductor Junctions," D. A. Jenny and J. J. Wysocki, *Jour. Appl. Phys.* (November) 1959
"Photoconductive and Photoelectromagnetic Lifetime Determination in Presence of Trapping. I. Small Signals," A. Amith, *Phys. Rev.* (November 15) 1959
"Finding Radio-Frequency Interference Levels," J. G. Arnold, *Electronics* (November 27) 1959
"The Achievement of Maximum Photoconductivity Performance in Cadmium Sulfide Crystals," R. H. Bube and L. A. Barton, *RCA Review* (December) 1959
"CdS Analog Diode and Triode," W. Ruppel and R. W. Smith, *RCA Review* (December) 1959
"Charts Ease Amplifier Calculations," R. A. Henderson, *Electronic Industries* (December) 1959
"Determining Screen Grid Dissipation in 'Ultra-Linear' Amplifiers," L. Kaplan, *Audio* (December) 1959
"Electroluminescence of Polycrystallites," S. Larach and R. W. Shrader, *RCA Review* (December) 1959
"Electronic Composites in Modern Television," R. C. Kennedy and F. J. Gaskins, *Jour. S.M.P.T.E.* (December) 1959
"Electronic Countermeasures — The Art of Jamming," D. J. Blattner. *Electronics World* (December) 1959
"Electronic Hardware," L. H. Henschel, *Electronic Industries* (December) 1959
"A Five-Transistor Automobile Receiver Employing Drift Transistors," R. A. Santilli and C. F. Wheatley, *Trans. I.R.E. PGBTR* (December) 1959
"How to Get Top Performance from the TVM-1A Microwave Equipment," *Broadcast News* (December) 1959
"Improvements in Detection, Gain Control, and Audio-Driver Circuits of Transistorized Broadcast-Band Receivers," D. Thorne and R. V. Fournier, *Trans. I.R.E. PGBTR* (December) 1959
"Infrared Photoconductive Detectors Using Impurity-Activated Germanium-Silicon Alloys," G. A. Morton, M. L. Schultz and W. E. Harty, *RCA Review* (December) 1959
"New 'B' Series Traveling Wave Antenna," M. S. Siukola, *Broadcast News* (December) 1959
"New Equipment for Measuring Envelope Delay," E. N. Luddy, *Broadcast News* (December) 1959
"New Special Effects System," R. P. Major, *Broadcast News* (December) 1959
"Optical Feedback Type Storage Light Intensifiers," H. O. Hook, *RCA Review* (December) 1959
"Properties of a Single-Element Light Amplifier Using Sintered Cadmium Selenide Photoconductive Material," F. H. Nicoll, *RCA Review* (December) 1959
"A Review of 'Electrofax' Behavior," J. A. Amick, *RCA Review* (December) 1959
"A Review of the IRE-PGEWS," T. T. Patterson, *Trans. I.R.E. PGEWS* (December) 1959
"Role of Space-Charge Currents in Light Amplifiers," A. Rose and R. H. Bube, *RCA Review* (December) 1959
"A Simplified Theory of Two-Carrier Space-Charge-Limited Current Flow in Solids," M. A. Lampert, *RCA Review* (December) .. 1959
"Sintered Cadmium Sulfide Photoconductive Cells," C. P. Hadley and E. Fischer, *RCA Review* (December) 1959
"Solid-State Image Intensifier Under Dynamic Operation," C. P. Hadley and R. W. Christensen, *RCA Review* (December) 1959

"Solid-State Optoelectronics," E. E. Loebner, *RCA Review* (December) 1959
"Thermoelectric Thermostat for X-Ray Diffraction," R. A. Horne, W. J. Croft, and L. B. Smith, *Rev. Sci. Instr.* (December) (Notes) 1959
"Turning Engineers Into Authors," W. A. Murphy, *Trans. I.R.E. PGEWS* (December) 1959
"A Volume-Charge Capacitor Model for 'Electrofax' Layers," J. A. Amick, *RCA Review* (December) 1959
"Wide-Band Facsimile Transmission Over a 900-Mile Path Utilizing Meteor Ionization," W. H. Bliss, R. J. Wagner, and G. S. Wickizer, *Trans. I.R.E. PGCS* (December) 1959
"How to Generate Accurate Sawtooth and Pulse Waves," C. A. Von Urff and R. W. Ahrons, *Electronics* (December 11) 1959
"High-Current Superconductivity," R. H. Parmenter, *Phys. Rev.* (December 15) 1959
"Resolution of the Ambiguity of Valence States in Spinels Containing Manganese and Iron," A. Miller, *Phys. Rev.* (December 15) 1959
"Accuracy of a Monopulse Radar," D. K. Barton, *Proc. I.R.E. 3rd National Conference on Military Electronics* 1959
"Television Broadcasting Antenna System Impedance Requirements," D. W. Peterson, *Proc. 13th Annual National Association of Broadcasters Engineering Conference* (March 15-18) 1959
"The Transistor — A New Friend for the Broadcaster," R. N. Hurst and J. W. Wentworth, *Proc. 13th Annual National Association of Broadcasters Engineering Conference* (March 15-18) 1959

Correction:

In the paper entitled "On the Nonlinear Behavior of Electron-Beam Devices," by F. Paschke, which appeared on pages 221-242 of the June 1957 issue, the third-order term of the velocity in Equation (19) (pp. 229-230) is incorrect. The correct value is

$$\frac{v_3}{v_{00}} = -\frac{1}{16}\left(\frac{\eta V_1}{v_{00}^2}\right)^3\left(\frac{\omega}{\omega_{p0}}\right)^2\left\{\sin(\omega t-\beta_e x)\left[\frac{\sin 3\beta_p x}{2}\left(1+9\left(\frac{\omega_{p0}}{\omega}\right)^2\right)\right.\right.$$

$$+\frac{\sin\beta_p x}{2}\left(1-3\left(\frac{\omega_{p0}}{\omega}\right)^2\right)-(1+\cos 2\beta_p x)\cdot 2\left(\frac{\omega_{p0}}{\omega}\right)^2\Bigg]$$

$$+\frac{\omega_{p0}}{\omega}\cos(\omega t-\beta_e x)\left[\sin 2\beta_p x+3\cos 3\beta_p x+5\cos\beta_p x\right]$$

$$+\sin 3(\omega t-\beta_e x)\left[-\frac{3}{2}\sin 3\beta_p x\left(1+\left(\frac{\omega_{p0}}{\omega}\right)^2\right)-\frac{1}{2}\sin\beta_p x\left(3-\left(\frac{\omega_{p0}}{\omega}\right)^2\right)\right.$$

$$\left.+(1+\cos 2\beta_p x)\cdot 2\left(\frac{\omega_{p0}}{\omega}\right)^2\right]-\frac{\omega_{p0}}{\omega}\cos 3(\omega t-\beta_e x)\left[3\cos 3\beta_p x\right.$$

$$\left.\left.+5\cos\beta_p x+3\sin 2\beta_p x\right]\right\}$$

The third-order terms in Equation (28) and the velocity pattern shown in Figure 2 should be changed accordingly. The error does not affect the discussion of the convection-current distribution.

HAROLD BORKAN received the B.S. degree in Electrical Engineering from Rutgers University in 1950. During 1945 and 1946 he served in the U. S. Navy. In June 1950 he joined the technical staff of RCA Laboratories at Princeton N. J. He did graduate work at Rutgers on a part-time basis, receiving the M.S. degree in Electrical Engineering in 1954. Since 1952 he has been in the Electronic Research Laboratory at Princeton and is engaged in research on television camera tubes and associated circuits. Mr. Borkan is a Senior Member of the Institute of Radio Engineers and a member of Eta Kappa Nu.

C. LOUIS CUCCIA received the B.S degree in Electrical Engineering in 1941 and M.S. degree in 1942, both from the University of Michigan. From 1941 to 1942, he was also employed as a research engineer for the Fisher Body Division of General Motors. He joined the technical staff of the RCA Laboratories in 1942 and worked on microwave-tube research and development until 1954. From 1954 to 1957, he was assigned to the color television activity of the laboratories specializing in evaluation of new ideas, patenting of new developments, and liaison between the various activities involved in color television receiver production. Early in 1957, he joined the Microwave Design Activity of the Electron Tube Division as Engineering Leader in charge of traveling-wave-tube and backward-wave oscillator design and development, and was responsible for the planning and development of RCA's new product line of periodically focused traveling-wave tubes. Since January 1959 he has been responsible for the product development of solid-state microwave amplifiers, and in the planning of new systems utilizing traveling-wave tubes.

E. DELLA TORRE received the B.E.E. degree from the Polytechnic Institute of Brooklyn in June, 1954 and the M.S. degree from Princeton University in 1956. He has since been at Rutgers, the State University, New Brunswick, New Jersey, where he is an instructor and an associate of the Microwave Electronics Laboratory. He has worked for Western Electric Company and Davies Laboratories, a division of Minneapolis Honeywell, during summers. The last two summers he has worked at RCA Laboratories in Princeton, New Jersey, where he was engaged in studying magnetic tapes. Mr. Della Torre is a member of Sigma Xi, and the Institute of Radio Engineers.

ALBERT FELLER received the BSEE and MSEE degree from the University of Pennsylvania. He is now working on his doctorate in electrical engineering. He came to RCA in 1951; from 1951 to 1956 he worked on VHF and UHF broadcast antennas. From 1956 to 1959, he participated in the development, for television broadcast transmitters, of special equipment such as color monitors, phase-correcting and frequency-control equipment, amplifiers, and multipliers. Since 1959, Mr. Feller has been working on development of electronic data processing equipment.

PETER FOLDES received the B.S. degree in electrical engineering from the Technical University of Budapest in Budapest in 1950. From 1950 to 1956 he was a research engineer at the Hungarian Telecommunication Research Institute and from 1953 to 1956, on a part-time basis, was also a lecturer on antennas at the Technical University of Budapest. In 1957 he joined RCA Victor Co., Ltd., Montreal, Canada. He has worked mostly in the field of antenna, propagation, and system engineering studies. Since 1958 he has been responsible for the theoretical aspects of the microwave subsystem in a wide-band microwave communication system. Mr. Foldes is a member of the American Institute of Electrical Engineers.

STEVEN G. KOMLOS received the B.S. degree in electronics engineering from the Technical University of Budapest in 1952. From 1952 to 1956 he worked as a lecturer at the Technical University of Budapest, and from 1954 to 1956 he was also consulting engineer for the Hungarian Television Co. In 1957, he joined RCA Victor Company, Ltd., Montreal, where he carried out development work in TV Broadcasting. At present, he is engaged in antenna development work.

ROBERT D. LARRABEE received the B.S. degree in electrical engineering and the M.S. degree in mathematics from Bucknell University in 1953. In 1955 he received the S.M. degree in science and in 1957 the Sc.D. degree in physics from the Massachusetts Institute of Technology. He joined the staff of RCA Laboratories in 1957 and has been engaged in the study of negative effective mass effects in semiconductors and in the measurement and utilization of plasma effects in semiconductors. He is a member of the Institute of Radio Engineers, Sigma Xi, Phi Mu Epsilon, Phi Eta Sigma, Pi Mu Epsilon, and Tau Beta Pi.

EDMUND A. LAPORT attended Northeastern University, Massachusetts University Extension, and McGill University. From 1924 to 1933 he was a radio transmitter engineer with Westinghouse Electric & Manufacturing Company at Springfield and Chicopee Falls, Mass. During 1933-34 he was associated with Paul F. Godley Company, Montclair, N.J. From 1934-36 he was a transmission engineer with Wired Radio, Inc., Ampere, N.J. From 1936 to 1938 he was in charge of high-power transmitter engineering for RCA Victor Division, Camden, N.J.; 1938-1944, Chief Engineer of RCA Victor Company, Limited, Montreal; 1944-1954, Chief Engineer of RCA International Division, New York City; from 1954 to date, Director of Communications Engineering for Radio Corporation of America, New York City, and, since March 1959, in Princeton, N.J. He is a Fellow of the Institute of Radio Engineers, and author of "Radio Antenna Engineering" (McGraw-Hill Book Co., 1952).

T. MURAKAMI received the B.S. degree in E.E. from Swarthmore College in 1944, and the M.S. degree from the Moore School of Electrical Engineering, University of Pennsylvania in 1947. From 1944 to 1946 he was an assistant and research associate in the Department of Electrical Engineering at Swarthmore College. Since 1946 he has been with the Advanced Development Section of the RCA Victor Television Division, Camden, N. J., working on radio frequency circuit development. Mr. Murakami is a Senior Member of the Institute of Radio Engineers and a member of Sigma Xi.

FRITZ PASCHKE received the degree of Diplom-Ingenieur in 1953 and the Dr. techn. sc. in 1955 from the Technical University Vienna. Between 1953 and 1955 he was a research assistant at the Institute of High-Frequency Techniques in Vienna. Since April 1956, Dr. Paschke has been a member of the technical staff at RCA Laboratories, Princeton, N. J.

A. C. VELDHUIS attended the Techniske Hooge School in Delft, Netherlands, for collegiate engineering studies. He passed his Propaedeutical examination (Mathematics) in 1938, his Candidate in Electrical Engineering examination in 1941, and his Engineer examination in 1941. During this period he also worked with Prof. Koomans on antenna design. After graduation he became a research engineer with Waldorp Instrumenten Fabriek in The Hague. During the War he had a command in the Dutch Underground forces. After liberation he was assigned to the Netherlands Purchasing Commission in New York City, on radio purchases. In 1946 he was honorably discharged from the army and then joined the Wind Turbine Company in West Chester, Pa., as chief engineer. He is also vice president of Wind Turbine Company of Canada, Limited. His work has been in the developments and design of antennas and transmission line systems of many kinds, including major high-frequency beam systems for Pakistan Broadcasting Service and the Royal Canadian Signal Corps. Mr. Veldhuis, who became a U.S.A. citizen in 1953, is a Senior Member of the Institute of Radio Engineers.